

2014

Lead sulfide colloidal quantum dots passivation and optoelectronic characterization for photovoltaic device application

Victor Malgras
University of Wollongong

UNIVERSITY OF WOLLONGONG

COPYRIGHT WARNING

You may print or download ONE copy of this document for the purpose of your own research or study. The University does not authorise you to copy, communicate or otherwise make available electronically to any other person any copyright material contained on this site. You are reminded of the following:

Copyright owners are entitled to take legal action against persons who infringe their copyright. A reproduction of material that is protected by copyright may be a copyright infringement. A court may impose penalties and award damages in relation to offences and infringements relating to copyright material. Higher penalties may apply, and higher damages may be awarded, for offences and infringements involving the conversion of material into digital or electronic form.

**LEAD SULFIDE COLLOIDAL QUANTUM DOTS
PASSIVATION AND OPTOELECTRONIC
CHARACTERIZATION FOR PHOTOVOLTAIC DEVICE
APPLICATION**

This thesis is submitted as part of the requirements for the award of the degree

DOCTOR OF PHILOSOPHY

From the

UNIVERSITY OF WOLLONGONG

By

VICTOR MALGRAS, M.Sc., B.Sc.

Institute for Superconducting and Electronic Materials

AIIM Facility, Innovation Campus

April, 2014

CERTIFICATION

I, Victor Malgras, declare that this thesis, submitted in partial fulfilment of the requirements for the award of Doctor of Philosophy, in the Institute for Superconducting & Electronic Materials, University of Wollongong, is wholly my own work unless otherwise referenced at any other academic institution.

Victor Malgras

April, 2014

ACKNOWLEDGEMENTS

I would like first to thank to Prof. S. X. Dou for accepting me in ISEM, University of Wollongong, as PhD candidate and for giving me a chance to work in such a good research environment.

It is my pleasure to express my sincere gratitude to my supervisors Dr. Jung Ho Kim for his trust, support and understanding, and Dr. Andrew Nattestad for introducing me to device engineering and providing guidance to address research through systematic approaches.

I am grateful to Dr. Attila J. Mozer, Dr. Tracey Clarke and Ms. Guanran Zhang for helping me performing the transient optoelectronic measurements and providing great advices regarding the data analysis, as well as Dr. Dongqi Shi for helping me in the operation of the X-ray photoelectron spectroscopy and Dr. David R.G. Mitchell for operating the atomic resolution TEM . I would also like to offer my gratitude to Dr. Tania Silver for helping me improve my English during the redaction of my thesis.

I would like to express my special thanks to my fiancée, Dr. Priyanka Jood, for her love and support, preventing me to fall in total dementia, and for waiting patiently the end of this degree for us to get married. I am also grateful to my friends from ISEM, Mr. Tomas Katkus, Mr. Igor Golovchansky, Dr. Ivan Seng, Mr, Xavier R. Ferreres and Mr. Rafael Santos for their valuable company throughout this PhD as well as to my dear friend Dr. Jean-Roch Nader.

I must convey my gratitude to the Australian Research Council (ARC) for the Discovery Project grant DP1096546 and the University of Wollongong for providing a University Postgraduate Award (UPA) and an International Postgraduate Tuition Award (IPTA).

I would also like to acknowledge Dr. Paul Wagner, Mr. Nicholas. Roach, Dr. Ivan Seng, Mr. Tomas Katkus, and Mr. Brendan Wright for their opinion relative to theoretical and experimental discussions, as well as Mr. Darren Attard, Mr. Mitchell Nancarrow and Dr. Patricia Hayes for training on microscopy and optical spectroscopy instruments.

I am grateful to my parents, Mr. Alain Malgras and Mrs. Marion Treger for their love and support throughout my whole life. Despite our divergent interests, they always were, and always will be role models to me, especially after seeing how fun their retirement looks.

Finally, thanks to the reader who can find valuable information in this work and use it for further research.

Table of Contents

CERTIFICATION.....	i
ACKNOWLEDGEMENTS.....	ii
LIST OF FIGURES.....	vii
LIST OF TABLES.....	xviii
LIST OF ABBREVIATIONS	xx
ABSTRACT.....	xxiv
CHAPTER 1 – INTRODUCTION	1
Reference.....	6
CHAPTER 2 – FUNDAMENTALS AND LITERATURE REVIEW.....	8
2.1 – Semiconductor physics	8
2.2 – Solar cells	14
2.2.1 – Solar spectrum and solar simulator	14
2.2.2 – <i>p-n</i> junction under illumination and the Shockley-Queisser limit	16
2.2.3 – Solar cells characteristics: ideal vs. real	19
2.3 - Quantum dots: properties and synthesis	22
2.3.1 – Confinement in quantum dots.....	22
2.3.2 – Tunable band gap.....	24
2.3.3 – Electron-hole pairs, excitons.....	26
2.3.4 – Relaxation dynamics, hot carriers, and multiple exciton generation	27
2.3.5 – Synthesis	30
2.4 – Quantum dots for photovoltaic application	33
2.4.1 – Typical device types and architectures	34
2.4.2 – The role of the ligands.....	38
2.4.3 – Transport in CQD Depleted Heterojunction Solar Cells	43
References	46
CHAPTER 3 – EXPERIMENTAL METHODOLOGY	58
3.1 – Introduction	58
3.2 – Material Characterization	58
3.2.1 – UV-Vis-NIR absorption spectroscopy	58
3.2.2 – Photoluminescence spectroscopy	60
3.2.3 – X-ray photoelectron spectroscopy (XPS).....	61
3.2.4 – Infrared (IR) spectroscopy.....	64

3.2.5 – Stylus profilometer.....	65
3.2.6 – Transmission electron microscopy (TEM).....	65
3.3 – Device characterization.....	66
3.3.1 – Solar simulator	66
3.3.2 – Current-voltage response under cold-white LED illumination	69
3.3.2 – Incident photon-to-charge carrier efficiency (IPCE)	70
3.3.3 – Charge extraction measurements.....	72
3.4 – Quantum dot synthesis.....	75
3.4.1 – Synthesis	75
3.4.2 – Washing.....	77
3.4.3 – Weighing and redispersing.....	77
3.5 – Device assembly.....	78
3.5.1 – FTO glass cutting and patterning	78
3.5.2 – Titanium dioxide dense layer deposition.....	80
3.5.3 – Individual device cutting	82
3.5.4 – Colloidal quantum dot layer deposition	83
3.5.5 – Contact evaporation.....	84
3.5.6 – Sealing	86
References	88
CHAPTER 4 – CHARACTERIZATION OF CARBOXYLIC LIGAND TREATMENT.....	89
4.1 – Introduction	89
4.2 – Experimental	90
4.3 – Results and discussion.....	92
4.3.1 – FTIR analysis	92
4.3.2 – XPS analysis	93
4.3.3 – Optical spectroscopy.....	107
4.4 – Conclusion	120
References	121
CHAPTER 5 – IMPACT OF SELECTIVE CONTACTS ON TRANSPORT AND STABILITY.....	126
5.1 – Introduction	126
5.2 – Experimental	126
5.3 – Results and discussion.....	128
5.3.1 – Steady state measurements	128
5.3.2 – Time-resolved optoelectronic measurements.....	138

5.4 – Conclusion	151
References	153
CHAPTER 6 – CONCLUSION AND FUTURE WORK	157
PUBLICATIONS DURING PHD.....	162
CONFERENCES ATTENDED DURING PHD	164

LIST OF FIGURES

Figure 1.1 – Efficiency timeline: NREL, the U.S. Department of Energy's primary national laboratory for renewable energy and energy efficiency R&D, documents efficiencies achieved by different developers worldwide (www.nrel.gov).	2
Figure 1.2 – Schematic representation of a multiple junction tandem solar cell (GaInP/GaAs/GaInAs), where each layer absorbs a specific portion of the solar spectrum.	4
Figure 2.1 – Band alignment during <i>p-n</i> junction formation. Before (a) and after (b) doping, and after contact (c).	9
Figure 2.2 –Representation of <i>p-n</i> junction transport mechanisms in the dark.	10
Figure 2.3 – Typical current density-voltage (<i>J – V</i>) profile of an ideal diode. ..	12
Figure 2.4 – Schematic diagram showing how the quasi-Fermi levels are split with the application of an external negative voltage.	14
Figure 2.5 – Geometric representations of the various solar spectrum standards AM 0, AM 1.0, AM1.5 and AM 2.0.	15
Figure 2.6 – Solar irradiance spectral distribution emphasizing the differences between AM 0 and AM 1.5. The factors responsible for specific wavelength range absorption are also indicated (en.wikipedia.org/wiki/Sunlight).	16
Figure 2.7 – AM 1.5 (blue) solar power and proportion which is actually absorbed by a standard crystalline silicon solar cell (purple). The orange dashed line represents the energy carried per photon at a specific wavelength.	17

Figure 2.8 – $J - V$ of a solar cell under illumination. The band bending and charge distribution are schematically illustrated for the short circuit (top inset) and open circuit (right inset) conditions.	19
Figure 2.9 – $J - V$ of a solar cell under illumination, emphasizing the main parameters.	20
Figure 2.10 – (a) Schematic representation of a box framed by infinite potential boundaries; (b) graphical representation of the authorized states (k_n, E_n) satisfying Equation 2.17; (c) schematic diagram showing how the band gap increases by decreasing the crystal size (Sigma-Aldrich.com).	23
Figure 2.11 – First excitonic energy dependence on the crystal diameter of the effective mass model (dotted curve), the hyperbolic model (dashed curve), and the 4-band model (solid curve). Symbols are experimental data from various publications (Kang <i>et al.</i> 1997).	25
Figure 2.12 – Schematic representation of heterojunctions of type I (a), II (b) and III (c).	26
Figure 2.13 – Schematic representation of excitonic levels located in the band gap.	27
Figure 2.14 – Fast relaxation in continuous energy levels (δE) and conservation of crystal momentum (Δk) in bulk semiconductors (a) versus MEG in nanocrystals (b) (Beard <i>et al.</i> 2012).	28
Figure 2.15 – Theoretical improvement of the Shockley-Queisser limit due to the MEG efficiency P (Beard <i>et al.</i> 2012).	29
Figure 2.16 – AFM images of InAs island growth for different In:As ratios (Benyoucef <i>et al.</i>).	30

Figure 2.17 – (a) Schematic of VLS mechanism. Low (b) and high (c) resolution TEM images of Si nanowires (by Ren <i>et al.</i>).	31
Figure 2.18 – Example of SILAR experimental setup to produce Hg²⁺ doped PbS QDs (by Lee <i>et al.</i> 2013).	31
Figure 2.19 – tri-n-octylphosphine oxide capped QD. (Jin <i>et al.</i> 2005).	32
Figure 2.20 – ZnCdSeS quantum dots with various sizes emitting at various wavelength (PlasmaChem).	33
Figure 2.21 – Hybrid Polymer/QDs solar cell (Emin <i>et al.</i> 2011).	34
Figure 2.22 – Quantum dot sensitized solar cell: architecture (a) and band structure (b) (Emin <i>et al.</i> 2011).	35
Figure 2.23 – Colloidal quantum dot Schottky junction solar cell: architecture (a) and band structure (b) (Emin <i>et al.</i> 2011).	36
Figure 2.24 – Quantum dot heterojunction solar cell: architecture (a) and band structure (b) (Emin <i>et al.</i> 2011).	37
Figure 2.25 – Schematic illustration showing various type of organic ligands with functional groups for biotechnology applications (Algar <i>et al.</i> 2010).	39
Figure 2.26 – Representation of steric spacing between CQDs when using (a) oleic acid or (b) 3-mercaptopropionic acid. Colour codes are as follow: oxygen: red, carbon: grey, hydrogen: white and sulfur: yellow.	40
Figure 2.27 – Scanning transmission electron microscope images CQDs after MPA (a) and EDT (b) ligand exchange (Jeong <i>et al.</i> 2012).	41
Figure 2.28 – S²⁻ inorganic capping by the Talapin group (Nag <i>et al.</i> 2011).	41
Figure 2.29 – Atomic-ligand passivation developed by (Tang <i>et al.</i> 2011).	42
Figure 2.30 – Atomic-chlorine passivation (Bae <i>et al.</i> 2012).	42

Figure 2.31 – SEM cross-section and band structure of a device with MoO_x selective contact (Gao <i>et al.</i> 2011).	44
Figure 2.32 – Push pump photocurrent method to probe trap states (Bakulin <i>et al.</i> 2013).	44
Figure 2.33 – Mid-gap band (MGB) participation in conduction (a) in the dark and (b) under illumination (Nagpal <i>et al.</i> 2011).	45
Figure 3.1 – Typical absorption spectroscopy set-up. The inset shows details of the geometry of the measurement.	59
Figure 3.2 – Representation of PL process with negligible (a) and significant (b) internal relaxation. E_G, E_{Abs}, E_{em}, and E_S are the band gap, the absorbed and emitted photon energy, and the Stoke shift, respectively.	60
Figure 3.3 – (a) Cryogenically cooled InGaAs-1700 detector from HORIBA Jobin Yvon and (b) its spectral response.	61
Figure 3.4 – Relation between the photon energy, the kinetic energy, the work function, and the binding energy for both sample and spectrometer in XPS measurement.	62
Figure 3.5 – Survey spectrum of a PbS CQD film. Inset shows a high resolution scan centered on the Pb 4f peaks.	63
Figure 3.6 – Stylus profiler sensor schematic.	65
Figure 3.7 – TEM imaging of PbS CQDs before (a) and after (b) exchanging oleic acid ligands for 3-mercaptopropionic acid. Images taken by Ziqi Sun (a and b) and David R.G. Michel (c).	66
Figure 3.8 – Photograph of the solar simulator set-up.	67

Figure 3.9 – Comparison between the real AM1.5 spectrum and the spectrum from the xenon lamp (with and without filter). The inset shows the AM1.5 filter transmission spectrum.	68
Figure 3.10 – IPCE for a typical PbS CQD solar cell (red) and dye-sensitized solar cell (blue). The AM1.5 spectral mismatch is represented by the dotted curve, and the purple rectangle frames the region of strong mismatch.	69
Figure 3.11 – (a) Home-made setup for cell characterization before sealing (in the glove box). (b) Comparison between the spectral irradiance of the LED and AM1.5.	69
Figure 3.12 – IPCE spectra of a typical device at slow (red) and faster (blue) scan rates. Data reported with permission of Guanran Zhang.	71
Figure 3.13 – In-house assembled IPCE setup.	71
Figure 3.14 – Illustrated procedure to measure time-resolved charge extraction at different switching times.	73
Figure 3.15 – Schematic representation of the photo-CELIV set-up.	74
Figure 3.16 – Oleic acid molecule (black: carbon, red: oxygen, white: hydrogen).	75
Figure 3.17 – Photograph of the flask before degassing (a,) before heating (b), and after heating (c).	76
Figure 3.18 – Bis(trimethylsilyl) sulphide molecule (yellow: sulphur, dark cyan: silicon, black: carbon, white: hydrogen).	76
Figure 3.19 – (a) Complete device and (b) scheme displaying the various layers.	78

Figure 3.20 – Schematic diagram showing the glass sheet substrate (a) before and (b) after the chemical etching process.	79
Figure 3.21 – Glass sheet arrangement for sonication.	80
Figure 3.22 –Schematic diagram showing the glass sheet substrate (a) before and (b) after the spray pyrolysis process.	81
Figure 3.23 – Profilometry data showing FTO and TiO₂ thickness.	82
Figure 3.24 – Schematic diagram of a substrate after cutting into individual pieces.	82
Figure 3.25 –Laurell Ws-400-6npp Lite spincoater.	83
Figure 3.26 – Schematc diagram showing individual substrate (a) before and (b) after PbS CQD spin-coating.	83
Figure 3.27 – Photograph showing (a) the thin brass evaporation mask, (b) the argon blanket set-up, and (c) the metal evaporator.	85
Figure 3.28 – Profilometry data showing MoO₃ film thickness for different evaporation thickness readings (on the quartz crystal balance).	85
Figure 3.29 – Pattern description showing individual substrate (a) before and (b) after contact evaporation. The drawing on the right gives a cross-sectional view of the device.	86
Figure 4.1 – Molecular structure of oleic acid, 3-mercaptopropionic acid, thioglycolic acid and thiolactic acid.	91
Figure 4.2 – IR spectra of the untreated sample (black) and the methanol (red), MPA (blue), TGA (magenta), and TLA (green) treated samples.	93
Figure 4.3 – XPS spectra centred on the C 1s peak for untreated (a), and methanol-only (b), MPA (c), TGA (d), and TLA (e) treated samples.	94

Figure 4.4 – XPS spectra centred on the O 1s peak for untreated (a), and methanol-only (b), MPA (c), TGA (d), and TLA (e) treated samples.	97
Figure 4.5 – XPS spectra centred on the Pb 4f peak for untreated (a), and methanol-only (b), MPA (c), TGA (d), and TLA (e) treated samples.	100
Figure 4.6 – XPS spectra centred on the S 2p peak for untreated (a), and methanol-only (b), MPA (c), TGA (d), and TLA (e) treated samples before ageing.	102
Figure 4.7 – XPS spectra centred on the S 2p peak for untreated (a), methanol-only (b), MPA (c), TGA (d) and TLA (e) treated samples after ageing.	104
Figure 4.8 – Bar graph showing the content variation after ageing process of component S_I, S_{II}, S_{III} and S_{IV} for each sample. Component S_{IV} in OA had a 200% increase; however the graph was cropped to facilitate the reading.	105
Figure 4.9 – Chemical structure of lead oleate.	105
Figure 4.10 – Esterification of carboxylic acid by methanol.	106
Figure 4.11 – Absorption spectra of suspended CQDs in toluene (dashed curve) and spin-coated films: untreated (black), methanol (red), MPA (blue), TGA (magenta) and TLA (green). The inset shows a higher resolution of the peaks maximum.	108
Figure 4.12 – Photoluminescence spectra for OA capped (black), methanol treated (red), MPA (blue), TGA (magenta) and TLA (green) capped samples.	111
Figure 4.13 – Combined absorption (red) and emission (blue) spectra for OA capped (a), methanol treated (b) and MPA capped (c) samples. Each curve is fitted with a simple or a double Gaussian. (black dot).	112

Figure 4.14 – Schematic representation of polydispersity on line broadening...	113
Figure 4.15 – Schematic representing three different passivation states. The Jablonsky diagrams describes of the passivation affect the electronic structure of the CQDs films.....	115
Figure 4.16 – Illustration of possible pathways for isolated CQDs (a) and for CQDs connected to TiO₂ (b). The thickness of the arrows is a qualitative indication of the proportion of electron involved in the pathway.	117
Figure 4.17 – Jablonski diagrams for each sample. The solid lines represent the <math>\langle 1S_h \rangle</math> and <math>\langle 1S_e \rangle</math> exciton energy levels, and the dashed lines represent the in-gap states. The energies displayed represent the shift with the OA sample energy levels (grey dashed line).....	119
Figure 5.1 – Profilometry of the PbS CQDs film on a typical device with 11 spin-coated layers.....	127
Figure 5.2 – (a) Partial IPCE spectrum (black solid curve) and complementary Gaussian fit (green solid curve) matching the first exciton peak from the absorption spectrum (dashed red curve). (b) Spectral current density (red solid curve) obtained from the convolution between the IPCE (black solid curve) and the lamp spectrum (purple dotted curve).....	128
Figure 5.3 – Current density-voltage ($J - V$) curves measured at different light intensities for devices with (a) 100 nm TiO₂ and (b) 135nm TiO₂ layer...	129
Figure 5.4 – Current-voltage curves measured at different light intensities for devices with (a) 100 nm TiO₂ and (b) 135nm TiO₂ layer.....	130
Figure 5.5 – (a) $J - V$ curves in forward (blue) and backward (red) bias voltage sweep for a device without MoO_x selective contact. Dotted lines	

correspond to a subsequent sweep. (b) log-log representation of the dark current.....	131
Figure 5.6 – Energy-band diagram showing a long (a) and short (b) channel and their impact on the potential barrier (S.M. Sze, 2006).	132
Figure 5.7 – Current-voltage curves measured with MoO_x (10 nm) selective contact. The dotted lines represent the scans in forward (blue) and backward (red) bias sweep and solid lines are the computed averages. Thinner lines are the immediate following scan.	134
Figure 5.8 – Energy band alignment between PbS CQDs and MoO_x.	135
Figure 5.9 – (a) Absorption spectroscopy of PbS CQDs films with (red) and without (blue) MoO_x layer. (b) and (c) Higher resolution spectra.	136
Figure 5.10 – Optical absorbance of the control PbS CQDs device. A red vertical line representing the laser pulse is also shown.	138
Figure 5.11 – (a) CELIV and photo-CELIV measurements for a standard device with 135 nm TiO₂ and 10 nm MoO_x. (b) Mobility dependence on the ramp rate.	139
Figure 5.12 – (a) Time-resolved charge extraction (TRCE) plot of 135 nm TiO₂/10 nm MoO_x device on a log-linear scale. (b) Half-life dependence on the light intensity.	141
Figure 5.13 – TRCE plot of 135 nm TiO₂/10 nm MoO_x device on a log-log scale.	142
Figure 5.14 – TRCE plot for devices without MoO_x (red), with 10 nm (green) and 20 nm (blue) MoO_x at 16 μJ/cm². The dashed lines are the fitted power law $n \propto t^{-\alpha}$ with their respective powers (α).	143

**Figure 5.15 – (a) OCVD for devices with 5 nm and 10 nm MoO_x at 160 μJ/cm².
(b) photovoltage dependence on the charge density from Figure 5.12. The dashed curves represent the exponential fit.144**

Figure 5.16 – Schematic describing the slow growth of V_{OC} after illumination with a laser pulse. t₀ describes the dark equilibrium before illumination. t₁ describes the system immediately after illumination. t₂ and t₃ describes the system with gradual charge diffusion. At t_{dr}, the maximum number of charges at the rear edge of the CQD film is reached. After t_{dr}, recombination becomes significant and EFP returns gradually to its initial position (at t₀).145

Figure 5.17 – Time-of-flight measurements. The inset shows the extracted charge (black) and half-life (red) dependence on the light intensity. The dashed lines indicate the limit after which the amount of extracted charges exceeds the capacitive charges stored at the contacts.146

Figure 5.18 – Transient photovoltage measurement under various V_{OC} conditions.148

Figure 5.19 – Transient photovoltage measurement (< 100 μs) for V_{OC}= 0.207 and 0.384 V.148

Figure 5.20 – (a) Dependence of stretched exponential power fitting parameter δ on V_{OC}. (b) Observed lifetime, τ_{obs}, dependence on the carrier density.150

Figure 6.1 – Illustration of three QDs differently passivated, the short and long molecules representing 3-mercaptopropionic acid and oleic acid,

respectively. The QD treated with methanol shows a significant proportion of ligands removed, as well as thin oxidized shell.....158

LIST OF TABLES

Table 3.1 – Specifications of the FTO glass from NSG.....	78
Table 3.2 – Sealing methods.....	87
Table 4.1 – List of C 1s components observed on CQD film with XPS and their assignment.....	96
Table 4.2 – List of O 1s components observed on CQD film with XPS and their assignment.....	98
Table 4.3 – List of Pb 4f components observed on CQD film with XPS and their assignment.....	101
Table 4.4 – Content of each S 2p component observed on CQD film with XPS before and after ageing process.....	103
Table 4.5 – List of S 2p components observed on CQD film from XPS and their assignement.....	107
Table 4.6 – Absorption peak position, shift from OA reference and FWHM.	109
Table 4.7 – Absorption and emission peak positions, FWHM and Stokes shifts for components (1) and (2) from the emission spectra for each sample	113
Table 4.8 – Ratio between the integral under the first component E_{Em1} and the area under the whole curve.....	116

Table 4.9 – Proportion of recaptured electrons over injected electrons into TiO₂.

.....118

Table 5.1 – Performances table for devices with different selective TiO₂ contact thickness......136

LIST OF ABBREVIATIONS

Abbreviation	Meaning
a	Separation between the grooves OR power law fitting parameter
A	Absorbance OR ramp rate
a_0	Bohr radius (0.529 Å)
a_{exc}	Exciton Bohr radius (nm)
AFM	Atomic Force Microscope
AM	Air-Mass index
BDT	1,3-Benzenedithiol
BE	Binding Energy
C	Capacitance
CELIV	Charge Extraction by Linearly Increasing Voltage
CIGS	Copper-Indium-Gallium-Selenide
CQD	Colloidal Quantum Dot
D	Diffusion coefficient
d	Thickness
DHJSC	Depleted Heterojunction Solar Cell
DOS	Density Of States
DSC	Dye-sensitized Solar Cell
E_{abs}	Absorption energy
E_{CB}	Conduction band edge energy level
EDT	1,2-Ethanedithiol
E_{em}	Emission energy
E_F	Fermi energy level
E_{FN}	Electrons quasi-Fermi level
E_{FP}	Holes quasi-Fermi level
E_G	Bang gap
E_{hv}	Photon energy
$E_{k,p}$	Energy calculated from the k·p Hamiltonian
$E_{ph,e}$	Phonon energy following electron relaxation
$E_{ph,h}$	Phonon energy following hole relaxation
E_S	Stokes shift
E_{Vac}	Vacuum energy level
E_{VB}	Valence band edge energy level
FTIR	Fourier Transform Infrared Spectroscopy
FTO	Fluorine doped Tin Oxide
FWHM	Full Width Half Maximum
G	Generation rate
GL	Gauss-Lorentz
h	Planck constant (6.62606957x10 ⁻³⁴ Js)

\hbar	Reduced Planck constant ($h/2\pi$)
I_0	Incident light intensity
IP	Ionisation potential
IPCE	Incident photon-to-charge carrier efficiency
IR	Infrared
I_T	Transmitted light intensity
ITO	Indium doped Tin Oxide
I_λ	Spectral current
J_0	Saturation current density
j_0	Differentiating RC-circuit current density step
J_{diff}	Diffusion current density
J_{drift}	Drift current density
J_{gen}	Generation current density
J_{mp}	Current density at the maximum power output
J_{ph}	Photogenerated current density
J_{rec}	Recombination current density
J_{sc}	Short-circuit current density
k	Wavenumber OR reaction rate
k_B	Boltzmann constant ($1.3806488 \times 10^{-23}$ J/K)
KE	Kinetic Energy
L	Length
LbL	Layer-by-Layer
L_{diff}	Diffusion length
L_{drift}	Drift length
L_N	Diffusion length of electrons
LO	Longitudinal Optical (related to phonon)
L_p	Diffusion length of holes
m^*	Electron-hole reduced mass
m_0	Free electron mass ($9.10938215 \times 10^{-31}$ kg)
m_e	Effective mass of electrons
MEG	Multiple Exciton Generation
MetOH	Methanol
m_h	Effective mass of holes
MPA	3-Mercaptopropionic Acid
n	Electron density OR Integer number
n_0	Density of electrons at equilibrium
N_A	Acceptor density
N_D	Donor Density
n_i	Intrinsic density
n_{id}	Ideality factor
NREL	National Renewable Energy Laboratory
NSG	Nippon Sheet Glass
OA	Oleic Acid

ODE	1-Octadecene
OFET	Optical Field-Effect Transistor
P	Power output
p_0	Density of holes at equilibrium
P_{in}	Power input from illumination
PL	Photoluminescence
P_{max}	Solar cell's maximum power output
PTFE	Polytetrafluoroethylene
q	Elementary charge ($1.60217657 \times 10^{-19}$ C)
QD	Quantum Dot
QDSC	Quantum Dot-sensitized Solar Cell
R	Resistance OR nanoparticle size
R_s	Series resistance
R_{sh}	Shunt resistance
S	Area
SCLC	Space Charge Limited Current
SILAR	Successive Ionic Layer Adsorption and Reaction
SJSC	Schottky Junction Solar Cell
T	Temperature
$t_{1/2}$	Half-life
TA	Transient absorption
TAA	Titanium diisopropoxide bis(acetylacetonate)
TCO	Transparent Conductive Oxide
TEM	Transmission Electron Microscope
TGA	Thioglycolic Acid
TLA	Thiolactic Acid
t_{max}	Extraction time
TMS	Bis(trimethylsilyl)sulfide
TOF	Time-Of-Flight
TPV	Transient Photovoltage
TRCE	Time-Resolved Charge Extraction
TRPL	Time-Resolved Photoluminescence
U_0	Differentiating RC-circuit voltage step
UV	Ultraviolet
V_{bi}	Built-in voltage
VLS	Vapour-Liquid-Solid
V_{mp}	Voltage at the maximum power output
V_{neg}	Negative applied voltage
V_{OC}	Open-circuit voltage
V_{pos}	Positive applied voltage
W	Depleted region length
XPS	X-ray Photoelectron Spectroscopy
Z	Atomic number
α	Absorption coefficient OR power law fitting parameter

γ	Exponential fitting parameter
Δj	Conductivity current density
Δn	Excess electrons
Δp	Excess holes
ϵ	Dielectric constant (permittivity)
ϵ_0	Vacuum dielectric constant (8.854 187 817x10 ⁻¹² F/m)
ϵ_r	Relative dielectric constant
ϑ	Angle OR fraction of free versus trapped carriers
λ	Wavelength
μ	Mobility
ω	Wave frequency (photons)
ρ_c	Density of states at the conduction band edge
ρ_v	Density of states at the valence band edge
τ	Lifetime
Φ	Work function
φ	Photon flux
χ	Electron affinity
ω	Wave frequency (phonons)

ABSTRACT

Photovoltaic energy conversion is one of the best alternatives to fossil fuel consumption. Petroleum resources are now close from depletion and their combustion is known to be responsible for releasing a considerable amount of greenhouse gas and carcinogenic airborne particles. Novel third-generation solar cells include a vast range of device architectures and materials aiming to overcome the factors limiting the current technologies. Among them, quantum dot based devices showed promising potential both as sensitizers and as colloidal nanoparticle film. *p*-doped PbS colloidal quantum dot (CQD) forming a heterojunction with a *n*-doped wide-band-gap semiconductor such as TiO₂ or ZnO. Ultimately, this technology would lead to the assembly of a tandem-type cell with CQD films absorbing in different region of the solar. The confinement in these nanostructures is also expected to result in marginal mechanisms such as hot carrier collection and multiple exciton generation which would increase the theoretical conversion efficiency limit.

In this work, certain mechanisms linked with CQD film passivation are addressed using various measurement methods. X-ray photoelectron spectroscopy is investigated in depth in order to pinpoint species specific to the role of methanol during the ligand exchange and notable differences are observed in the surface states of films treated with 3-mercaptopropionic acid, thioglycolic acid and thiolactic acid. The removal of the initial oleic acid ligand following methanol rinsing clearly leaves the CQD unprotected against adventitious oxidation altering a single atomic monolayer of the nanoparticles, as confirmed by a broadening and blue shift of the first exciton energy observed on UV-Vis absorption spectroscopy. Through fluorescence spectroscopy, two in-gap states are identified in each sample and the non-

uniform quenching after ligand exchange suggests that 1% of the charges injected in TiO₂ are recapture by the deeper trap state. Thiolactic ligand treatment shows a notable enhanced protection against surface contamination and displayed negligible electronic configuration change compared to the untreated sample while providing similar quenching properties. It can be related to the fact that this molecule is more bulky due to its -CH₃ group and undergoes more steric interactions with neighbouring ligands.

A whole assembly procedure is optimized, from the PbS CQDs synthesis to characterization of selective contacts based devices. Current-voltage analysis in dark conditions indicates that transport in such device appears to be strongly affected by space-charge limiting effects due to in-gap trap states distribution. The impact of TiO₂ and MoO_x selective contacts is also addressed. MoO_x not only improves performance due to electron screening barrier, it also enhances stability significantly. No sign of free extracted charge is observed, indicating that the doping in the CQD film is negligible. Through time resolved charge extraction measurements, one can observe that recombination appears to be first dominated by relatively slow mechanisms and undergoes a fast acceleration. The time at which this acceleration occurs looks to be partly related to the MoO_x thickness, suggesting that recombination with the external circuit might play a dominant role. Recombination regimes are addressed and appears to involve multiple mechanisms which cannot be simply fit with common first or second order reaction rates.

CHAPTER 1 – INTRODUCTION

A.E. Becquerel might have observed the photovoltaic effect for the first time in 1839¹ by detecting small currents when silver chloride was illuminated, but it was only when C. Fritts deposited selenium on a thin layer of gold in 1883 that the junction solar cell was first produced, albeit with an efficiency below 1%. The early 20th century is marked by significant progress in crystallography (P. Curie), solid state physics (J.J. Thomson, P. Drude, P. Debye, F. Bloch) and statistical physics (A. Einstein, M. Planck, L. Boltzmann), which unlocked many doors towards the understanding of semiconductor-junction-based photovoltaic devices. Various combinations were attempted before D. Chapin developed a doped (diffused) silicon *p-n* junction based solar cell in Bell Laboratories in 1954 following R. Ohl's patent. The device, with an efficiency of around 6%, gave birth to the first generation of commercially relevant solar cells.

Most solar panels used nowadays are still built on this crystalline silicon *p-n* junction technology and reach a commercially available efficiency of 22%.² Combined with the discovery of the transistor in 1947 (J. Bardeen, W. Shockley, and W. Brattain), which replaced “vacuum tube technology” by a scalable “electronics”, the demand for manufactured semiconductors increased significantly.

The price of silicon based solar cells fell from AU\$ 82.89/watt in 1977 to AU\$ 0.80/watt in 2013 (converted from USD)³ making the sun a competitive energy source substituting for coal or other fossil fuels (AU\$ 116.00/MWh from a new baseload gas power station).⁴ Researchers are still targeting improvements, however, regarding

stability (life span, heat/moisture resistance), recyclability and especially efficiency and production costs.

For various reasons, researchers had to look in another direction, as this technology started to reveal certain limitations. W. Shockley and H. Queisser calculated in 1961 that there was a theoretical limit specific to this type of single junction in “bulk” semiconductor solar cells restricting the efficiency to never more than 33.7%.⁵ The mechanisms involved in power losses will be developed in the following chapter. Moreover, a typical silicon purification line requires 650°C baking processes⁶ and is responsible for most of the energy cost of production.

The National Renewable Energy Laboratory (NREL) keeps a detailed track of the various photovoltaic technologies which appeared since 1975 (Figure 1.1).

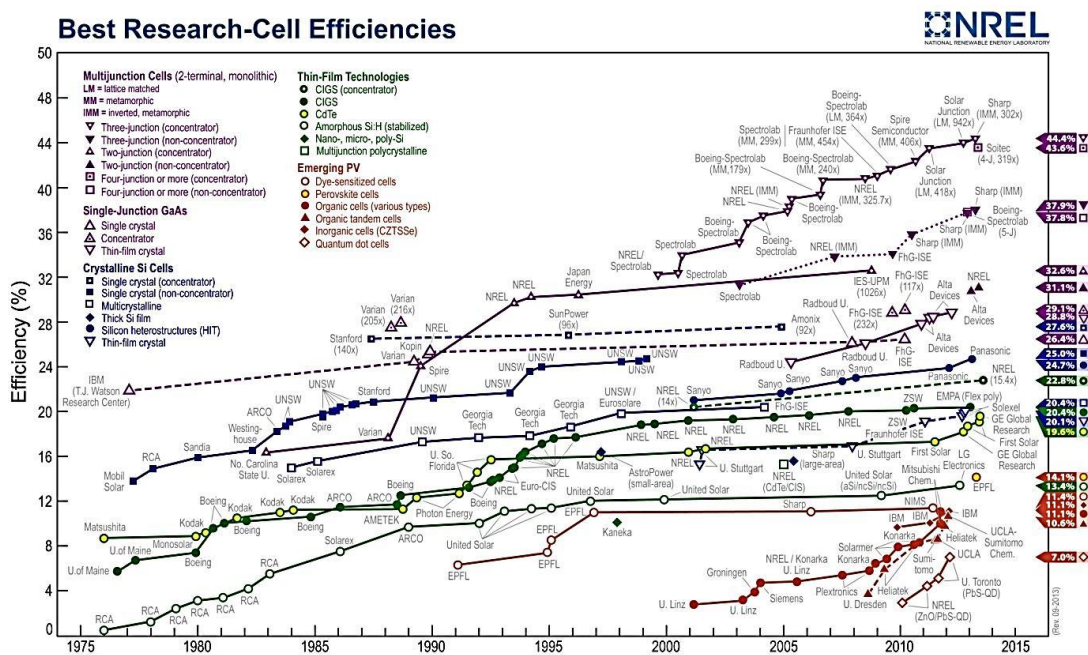


Figure 1.1 – Efficiency timeline: NREL, the U.S. Department of Energy's primary national laboratory for renewable energy and energy efficiency R&D, documents efficiencies achieved by different developers worldwide (www.nrel.gov).

The second generation of solar cells was aimed towards “greener” solutions and tried to decrease the amount of matter involved in the cell’s architecture by using a strongly light absorbing material such as copper-indium-gallium-selenide (CIGS) 2-4 μm thin films collecting more of the light over the 400-800 nm range.⁷ This technology can now achieve 19.6% conversion efficiency.⁸ The 2nd generation also includes organic and dye-sensitized solar cells which are assembled through relatively simple and low-cost processes and able to reach efficiencies above 13%.⁹ The latter attracted considerable attention because of their “do it yourself” potential (simple technological manufacturing and low material purity requirements). These devices suffer from relatively shorter life-span stability, however, due to the use of liquid electrolytes, which make the devices hard to encapsulate. More recent research tends to address this drawback by using solid-state hole transporting materials,¹⁰ ionic liquids,¹¹ or photonic crystal.¹²

The third generation solar cells mostly target various ways to overcome the Shockley-Queisser limit. The unbeaten record comes from tandem cells with 36.9% efficiency, resulting from the stacking of several *p-n* junctions made from elements optimized to absorb specific regions of the solar spectrum. Nevertheless, such technology requires metalorganic vapour phase deposition techniques, which increase the cost of production by several orders of magnitude and still limit its use to aerospace applications.

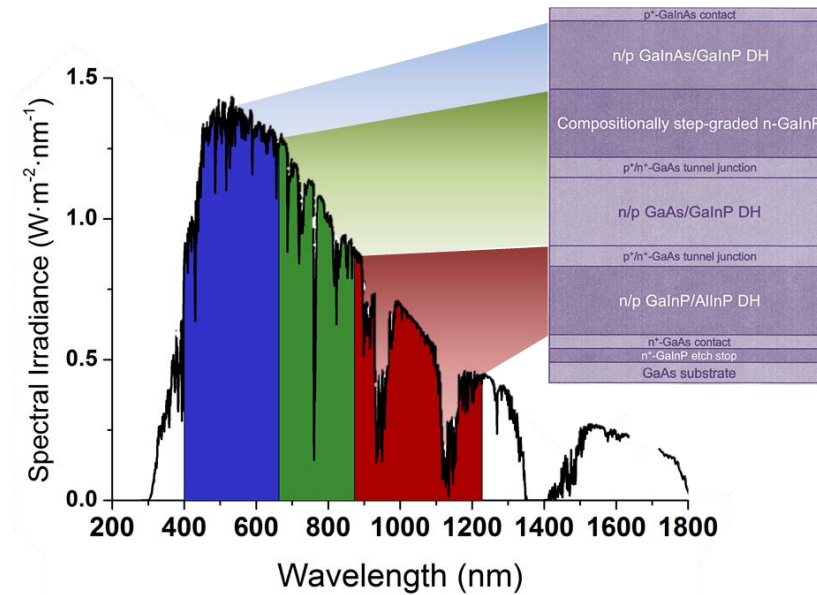


Figure 1.2 – Schematic representation of a multiple junction tandem solar cell (GaInP/GaAs/GaInAs), where each layer absorbs a specific portion of the solar spectrum.

Another strategy consists of using quantum dots (crystals on the nanometer scale) as light absorbers. Under a specific size, certain binary crystals show significant changes in their optical and electronic behaviour, making them an attractive option for light harvesting technology. The enthusiasm for quantum dot based solar cell started when A. J. Nozik^{13, 14} assumed in 2001 that phenomena such as hot carrier collection and multiple exciton generation could significantly increase solar cell performances and thus, overcome the Shockley-Queisser limit. Different methods exist to produce these nanocrystals such as vapour-liquid-solid, molecular beam epitaxy, electron beam lithography, successive ionic layer adsorption and reaction, and the synthesis of colloidal quantum dots (CQDs) through a nucleation process. The former three are “physical syntheses” and require highly controlled atmosphere, high voltage, and/or high vacuum, which are obstructing their application.

The latter methods, known as “chemical syntheses” are relatively cheap to set up but require significant optimization in order to achieve controlled size and size distribution. Moreover, one has to replace the long organic ligand originating from the

synthesis process and cap the colloidal QDs to prevent agglomeration by a smaller agent. There is a great deal of research that is currently aiming to improve this “ligand exchange” method and thus improve device performances and stability.

There are three architectures that have been investigated to achieve proper photovoltaic devices: the Schottky junction, the quantum dot sensitizer and the depleted heterojunction. The latter recently achieved 7.4% efficiency through the use of hybrid passivation methods.¹⁵ However, the performance of these devices is still limited due to a poor understanding of how the QDs passivation and other structural features influence the transport mechanisms.

This study aims to investigate in details the impact of typical organic treatment on the surface passivation of the nanoparticles and to ascertain what the major transport limitations are. Chapter 2 combines fundamental explanations on the mechanisms at the origin photovoltaic performances and a review on the properties and applications of quantum dots as well as the state-of-the-art in PbS colloidal quantum dots base solar cells. Chapter 3 describes the techniques used in this work to characterize material and devices, as well as the home-built set-up developed in order to synthesize the PbS nanoparticles and to assemble the solar cells. Chapter 4 gives detailed X-ray photoelectron spectroscopy and steady-state optical spectroscopy analyses of the passivation treatment using various organic ligands. Chapter 5 describes the steady-state and transient optoelectronic measurements leading to a better understanding of charge transport and recombination in such devices. Finally, Chapter 6 summarizes the major findings made during this research, providing further recommendation for future work.

Reference

1. Becquerel, A.E., *Mémoire sur les effets électrique produits sous l'influence des rayons solaires*. Comptes rendus hebdomadaires des séances de l'Académie des sciences, 1839. **9**: p. 561.
2. Parida, B., S. Iniyar, and R. Goic, *A review of solar photovoltaic technologies*. Renewable and Sustainable Energy Reviews, 2011. **15**(3): p. 1625.
3. Carr, G., *Sunny uplands: Alternative energy will no longer be alternative*, in *The Economist*. 2012.
4. Hannam, P., *Rising risk prices out new coal-fired plants: report*, in *The Sydney Morning Herald*. 2013: Sydney.
5. Shockley, W. and H.J. Queisser, *Detailed Balance Limit of Efficiency of p-n Junction Solar Cells*. Journal of Applied Physics, 1961. **32**(3): p. 510.
6. Becker, C., et al., *Microstructure and photovoltaic performance of polycrystalline silicon thin films on temperature-stable ZnO:Al layers*. Journal of Applied Physics, 2009. **106**(8): p. 084506.
7. Chu, V.B., et al., *Fabrication of solution processed 3D nanostructured CuInGaS₂ thin film solar cells*. Nanotechnology, 2014. **25**(12): p. 125401.
8. Green, M.A., et al., *Solar cell efficiency tables (version 39)*. Progress in photovoltaics: research and applications, 2012. **20**(1): p. 12.
9. Yella, A., et al., *Porphyryin-sensitized solar cells with cobalt (II/III)-based redox electrolyte exceed 12 percent efficiency*. Science, 2011. **334**(6056): p. 629.
10. Bach, U., et al., *Solid-state dye-sensitized mesoporous TiO₂ solar cells with high photon-to-electron conversion efficiencies*. Nature, 1998. **395**(6702): p. 583.
11. Kuang, D., et al., *Stable dye-sensitized solar cells based on organic chromophores and ionic liquid electrolyte*. Solar energy, 2011. **85**(6): p. 1189.

12. Chung, I., et al., *All-solid-state dye-sensitized solar cells with high efficiency*. Nature, 2012. **485**(7399): p. 486.
13. Nozik, A.J., *Spectroscopy and hot electron relaxation dynamics in semiconductor quantum wells and quantum dots*. Annual Review of Physical Chemistry, 2001. **52**: p. 193.
14. Nozik, A.J., *Quantum dot solar cells*. Physica E-Low-Dimensional Systems & Nanostructures, 2002. **14**(1-2): p. 115.
15. Ip, A.H., et al., *Hybrid passivated colloidal quantum dot solids*. Nature Nanotechnology, 2012. **7**(9): p. 577.

CHAPTER 2 – FUNDAMENTALS AND LITERATURE REVIEW

In order to introduce the notions behind energy conversion and charge extraction in colloidal quantum dot (CQD) solar cells, this Chapter will develop general concepts regarding semiconductor physics¹, electronic transport in typical *p-n* junctions in the dark and with photogenerated carriers, and basic performances measurements of non-ideal photovoltaic devices, before developing the typical properties of quantum dots materials. Following this theoretical background, the state of the art in CQD solar cells technology will be discussed, including architecture, treatments, and passivation techniques.

2.1 – Semiconductor physics

By definition, an intrinsic semiconductor's Fermi level is located in the middle of the bandgap so $E_F = \frac{E_{CB} + E_{VB}}{2}$, in between the valence band (E_{VB}) and conduction band (E_{CB}). This means that the charges in the material are balanced (positive vs. negative). Phosphorus has one more valence electron in its highest orbital than silicon. Typically, doping P atoms into Si through the diffusion process tends to increase the available electrons for further charge transport. When a semiconductor is doped with *donor* impurities, it is called an *n*-type semiconductor and has negative charges as *majority carriers*. At high doping concentrations, electrons start to occupy states which are closer to the conduction band, which results in a shift of the Fermi level

towards higher energies. Boron has one less valence electron than silicon. Typically, doping B atoms into Si tends to increase the available holes. Analogously, *p*-type semiconductors are doped with *acceptor* impurities and have holes as majority carriers, while the Fermi level is shifted towards lower energies.

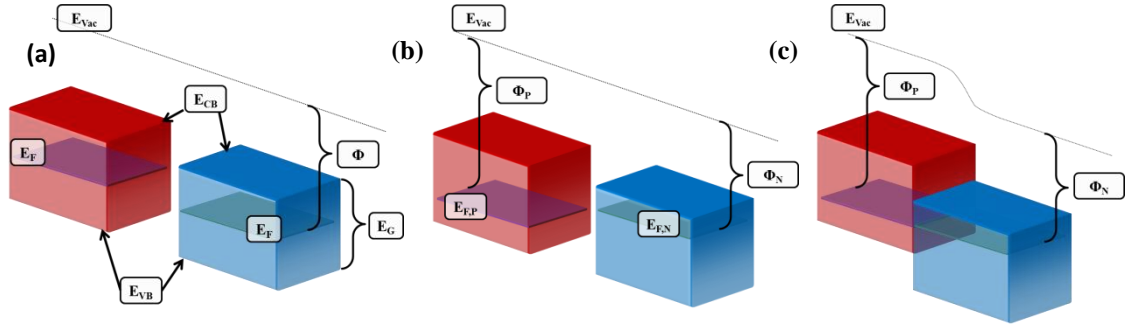


Figure 2.1 – Band alignment during *p-n* junction formation. Before (a) and after (b) doping, and after contact (c).

The position of the Fermi level is dictated by the available electrons and “states” in the system. We refer to the *density of states* (DOS) to determine how electrons are distributed in the energy continuum (for bulk materials). The DOS in E_{CB} and E_{VB} can be seen as the number of states in ΔE (centred on E) per unit of volume and can be determined by:

$$\rho_C = \frac{8\pi m_e \sqrt{2m_e(E - E_{CB})}}{h^3} \quad (2.1)$$

$$\rho_V = \frac{8\pi m_h \sqrt{2m_h(E_{VB} - E)}}{h^3} \quad (2.2)$$

where E , h , m_e , and m_h are the energy, the Planck constant, and effective mass of the electrons and holes, respectively. The effective masses are the masses that the electrons and holes “seem” to have when they move in a crystal lattice. It is a way to take into account the periodic potential which is unique to each material.

In the case where no carriers are optically generated (in the dark) and no external bias is applied, if both types are compatible (negligible lattice mismatch) and form a junction, an electrostatic equilibrium takes place, where electrons diffuse along a concentration gradient from n - to p - in order to uniformly occupy the available space. The remaining static charges tend to repel mobile charges in the junction's neighbourhood forming a "depleted region", and thus leaving locally a positive polarity on the n -side and a negative polarity on the p -side (see Figure 2.2). The resulting internal electric field allows the few minority carriers to drift through the junction, while statistically, some majority carriers have enough energy to cross the electric field backward. The system is at equilibrium when the net-current flow is nil and the vacuum level has shifted so that the Fermi level can be uniform throughout the material while keeping the respective work functions unchanged.

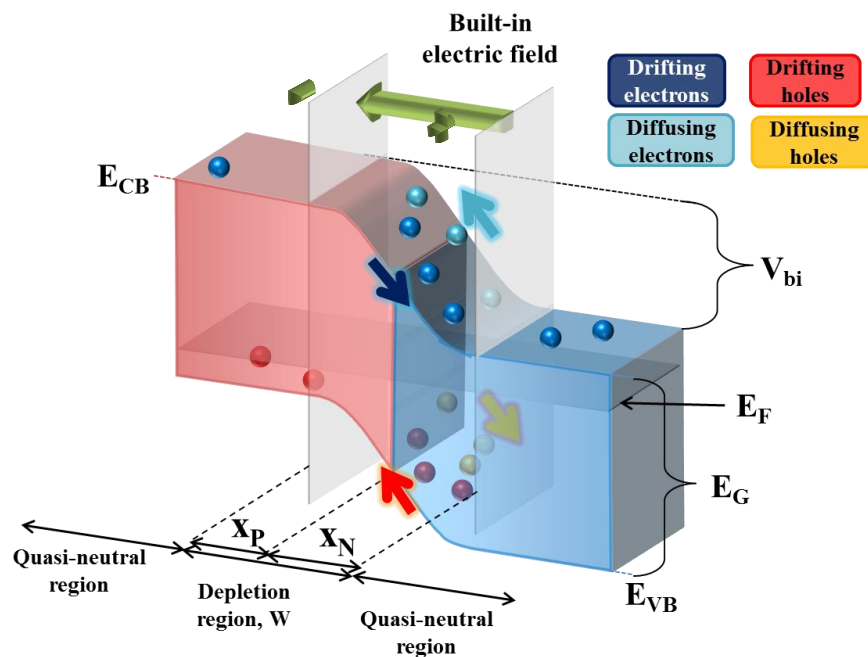


Figure 2.2 – Representation of p - n junction transport mechanisms in the dark.

The spatial distribution of the depleted region depends in the doping level in each side of the junction:

$$W = \sqrt{\frac{X_P}{\frac{2\varepsilon V_0}{q} \frac{N_A}{N_D(N_A+N_D)}}} + \sqrt{\frac{X_N}{\frac{2\varepsilon V_0}{q} \frac{N_D}{N_A(N_A+N_D)}}} = \sqrt{\frac{2\varepsilon V_0}{q} \left(\frac{1}{N_A} + \frac{1}{N_D} \right)} \quad (2.3)$$

with the built-in potential $V_{bi} = \frac{k_B T}{q} \ln \left(\frac{N_A N_D}{n_i^2} \right)$, where ε , q , k , T , N_A , N_D , and n_i are the permittivity, elementary charge, Boltzmann constant, temperature, and acceptor, donor and intrinsic densities, respectively. X_P and X_N represent the depleted region's proportions on the p -side and n -side, respectively. Thermally generated charges reaching the depletion region are quickly swept along by the electric field and participate in the drift current ($J_{gen} = J_{drift}$). Outside this region, the electric field is negligible, and charge transport is dominated by diffusion mechanisms.

The ‘‘charge lifetime’’ τ corresponds to the average time these minority carrier charges can move about before recombining with the majority carriers ($J_{rec} = J_{diff}$). During that time, carriers can travel a drift length, L_{drift} , if they are in the depletion region and a diffusion length, L_{diff} , if they are in the quasi-neutral region:

$$L_{drift} = \frac{2\mu V_{bi} \tau}{W} \quad (2.4)$$

$$L_{diff} = \sqrt{D\tau}, \text{ with } D = \frac{\mu k_B T}{q} \quad (2.5)$$

where D and μ are the diffusion coefficient and the charge mobility, respectively.

In the context of solar cells, device engineering should ensure high values for these lengths in order to collect as many carriers as possible before they recombine. This can be achieved more easily in a bulk junction where materials can be processed to minimize the defects, impurities, and lattice mismatch causing transport hindrance. Indeed, certain defects cause the disruption in the lattice which commonly leads to the formation of electronic states lying in the band gap. The resulting potential wells tend

to capture charges, hindering the overall transport process. The energy difference between these states and the band corresponding band edge (E_{CB} for electrons and E_{VB} for holes) will determine if the traps are deep or shallow. Charges have a higher probability to hop out of a shallow trap (thermal/optical activation) than from deep traps. The latter will tend to hold the captured charge long enough to make it recombine (recombination centre). Good diffusion still represents a significant trade-off for emerging photovoltaic technologies, however. On the other hand, shallow traps arising, for example, from surface reconstruction in TiO_2 mesoporous layers are not as detrimental. Indeed, if the mobility decreases, the lifetime increases, keeping the product $\mu\tau$ relatively unchanged.

If the system is negatively biased through an external source ($-V_{neg}$), the potential barrier at the interface will simply increase to $V_{bi} + V_{neg}$, inducing a drop in J_{diff} , while keeping the thermally generated drift current J_{drift} relatively unchanged, as the available minority carriers are not altered by the height of the potential drop. Under forward bias ($+V_{pos}$), the potential drops to $V_{bi} - V_{pos}$, and more charges diffuse through the depletion region to become minority carriers.

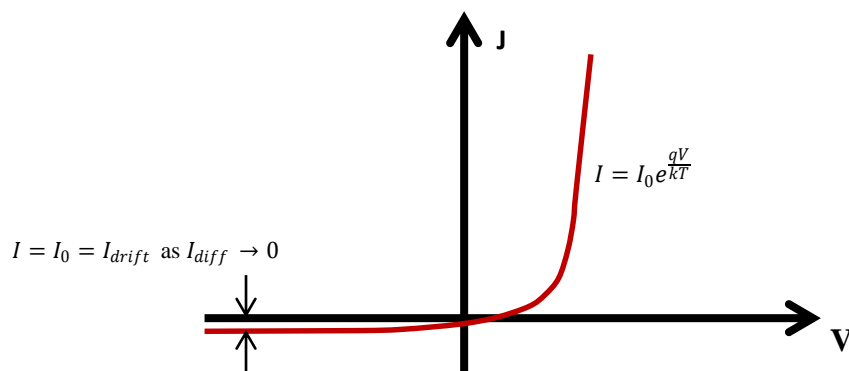


Figure 2.3 – Typical current density-voltage ($J - V$) profile of an ideal diode

If the potential barrier disappears (i.e. $V_{pos} > V_{bi}$), J_{diff} increases exponentially following the Shockley ideal diode approximation (see current density-voltage plot in Figure 2.3):

$$J = J_0 \left(e^{\frac{qV}{k_B T}} - 1 \right) = J_{diff} - J_{drift} \quad (2.6)$$

where J_0 is the reverse saturation current (thermally generated minority carriers) and V is the applied voltage. Note that $J_0 \approx J_{drift}(V)$ and $J_0 e^{\frac{qV}{k_B T}} \approx J_{diff}(V)$. At this point, it is important to introduce the concept of *quasi-Fermi levels* (also known as *chemical potentials*), which represent the Fermi level seen by electrons, E_{FN} , and by holes, E_{FP} , when the system is displaced from equilibrium. When excess charges are generated (through bias or illumination), the quasi-Fermi levels are displaced to satisfy the new energy distribution.

$$E_{FN} = E_{CB} + k_B T \ln \left(\frac{n_0 + \Delta n}{\rho_c} \right) = E_F + k_B T \ln \left(\frac{\Delta n}{\rho_c} \right) \quad (2.7)$$

$$E_{FP} = E_{VB} - k_B T \ln \left(\frac{p_0 + \Delta p}{\rho_v} \right) = E_F - k_B T \ln \left(\frac{\Delta p}{\rho_v} \right) \quad (2.8)$$

with n_0 , p_0 , Δn , Δp , ρ_v , and ρ_c the density of electrons and holes at equilibrium, the concentration of excess electrons and holes, and the effective density of state in the valence band and in the conduction band, respectively.

The quasi-Fermi levels of majority carriers are not significantly affected, as their density is already high and relatively unchanged, but minority carriers' quasi-Fermi levels will undergo a significant shift. For example, if there is a forward bias, V_{pos} , the Fermi level will split in order to be closer to each respective band edge (Figure 2.4), with the energy difference $E_{FN} - E_{FP} = qV_{pos}$.

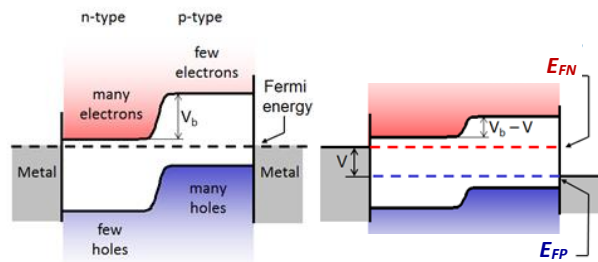


Figure 2.4 – Schematic diagram showing how the quasi-Fermi levels are split with the application of an external negative voltage

2.2 – Solar cells

Solar cells are nothing more than diodes in which the generation current can be greatly increased due to the ability of the material to absorb photons, exciting electrons, which will add to the thermally generated current. The following sections extend the aforementioned concepts to the applications in photovoltaic devices.

2.2.1 – Solar spectrum and solar simulator

The sun's irradiance and the shape of its spectral distribution vary with the latitude, time of the year, and time of the day, as well as with the weather conditions, (clouds, humidity, wind, etc.). In order to define a standard sun to compare photovoltaic devices' efficiency, one can refer to the air-mass (AM) index that relates to different applications. AM 0 represents the solar spectrum above the edge of the atmosphere.

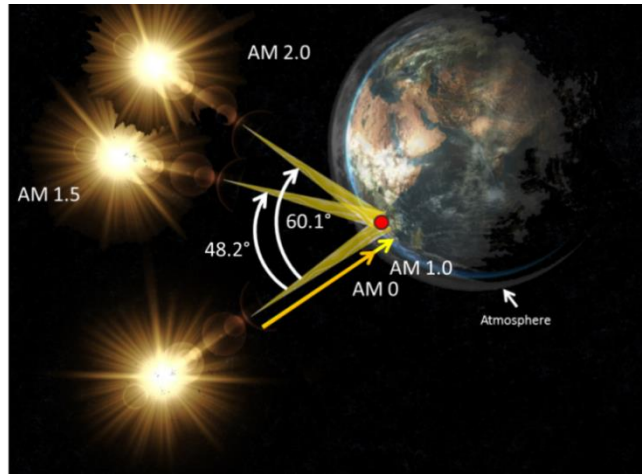


Figure 2.5 – Geometric representations of the various solar spectrum standards AM 0, AM 1.0, AM1.5 and AM 2.0.

AM 1.0, 1.5, and 2.0 express the solar intensity from the sun after passing through the atmosphere at different angles (see Figure 2.5). This gaseous layer is composed of various compounds which absorb a significant proportion (up to 23%) of the light intensity (see Figure 2.6). AM 0 will then only be relevant for extraterrestrial applications (e.g. satellites) while the others give insight on the input power a solar cell receives in a day. AM 1.0 is exact only if the device is tested to be installed in equatorial or tropical regions at the zenith. Most of the Earth's population, however, lie further from the equator in temperate zones, where the zenith makes an angle of 48.2° , increasing the light path across the atmosphere (AM 1.5). Some other refinements include the *albedo* of the surroundings (diffuse reflectivity of a surface). Most solar simulators use a xenon arc lamp with filters mimicking the AM 1.5 spectrum.²

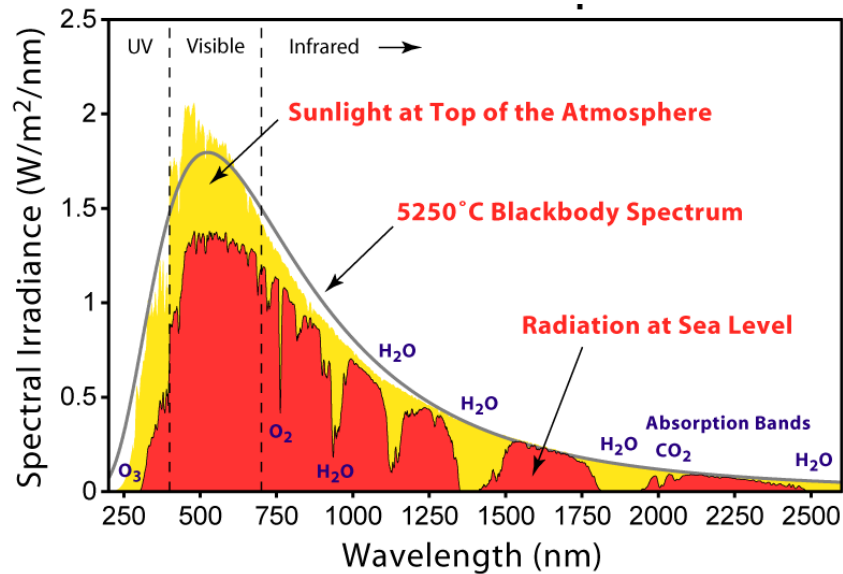


Figure 2.6 – Solar irradiance spectral distribution emphasizing the differences between AM 0 and AM 1.5. The factors responsible for specific wavelength range absorption are also indicated. (en.wikipedia.org/wiki/Sunlight)

2.2.2 – *p-n* junction under illumination and the Shockley-Queisser limit

In dark conditions, generated current is induced by thermally activated charge carriers. Photons convey more energy than phonons (< 100 meV), and thus their contribution to the generation current can be more significant if the band gap for materials with suitable band gap. The solar spectrum is mostly spread between 250 nm (4.96 eV) and 4000 nm (0.31 eV), split up between ultraviolet (UV), visible, and infrared (IR) light.

As described by Shockley and Queisser in 1961,³ conversion and extraction mechanisms limit the standard solar cell to 33.7% efficiency. First, photons with a lower energy than E_G will simply be transmitted through the junction, diffracted, or reflected. This phenomenon is responsible for the loss of 19% of the available solar energy for a typical standard crystalline silicon solar cell with $E_G \approx 1.1$ eV (see Figure

2.7). Secondly, if a photon transfers an energy E_{hv} higher than E_G to an electron, the latter will be promoted to a charge carrier state in a higher energy level and will thermalize to the bottom of E_{CB} by releasing a phonon (lattice vibration) with an energy $E_{ph,e}$ (analogously $E_{ph,h}$ for holes) with $E_{ph,e} + E_{ph,h} = E_{hv} - E_G$. This other mechanism accounts for the 33% solar power loss.

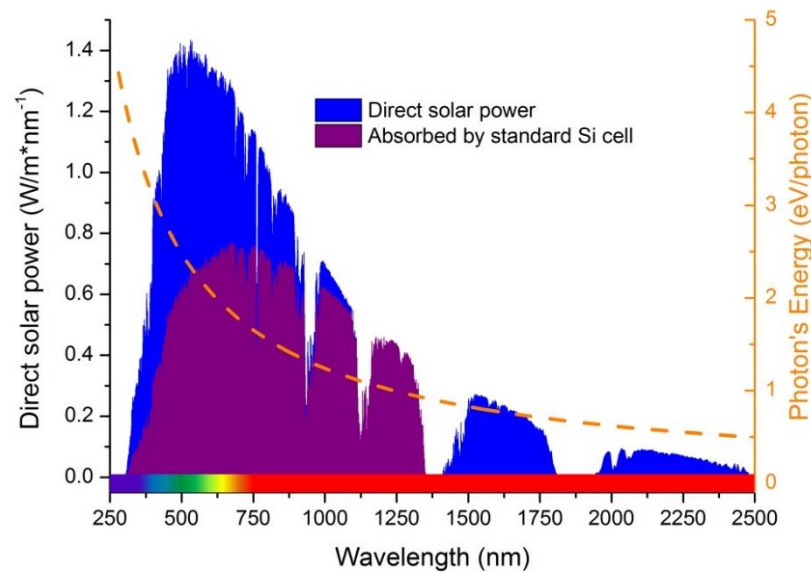


Figure 2.7 – AM 1.5 (blue) solar power and proportion which is actually absorbed by a standard crystalline silicon solar cell (purple). The orange dashed line represents the energy carried per photon at a specific wavelength.

Finally, phenomena such as the radiation of the photovoltaic device (black body radiation > 300 K) and radiative recombination (detailed balance principle) monopolize another $\sim 15\%$ of the incoming solar energy.

Figure 2.8 depicts a typical current density – voltage ($J - V$) curve of a solar cell in the dark (dotted line) and under illumination (solid line). Note that it is the same plot as the one from Figure 2.4, but it is conventionally transposed from the 4th quadrant to the first quadrant. The current measured is then (for an ideal cell):

$$J = J_{ph} - J_0 \left(e^{\frac{qV}{kT}} - 1 \right) \quad (2.9)$$

where J_{ph} is the photogenerated current.

Under *short circuit conditions* (left inset in Figure 2.8), most of the photogenerated charges drift along the electric field, while the diffusion flow stays unchanged. The short-circuit current density, J_{sc} , is at a maximum and corresponds to the photogenerated charges diffusing towards the depletion region to be swept along by the junction polarity. Its main limitation is the diffusion length and the minority carriers' lifetime, which can cause them to recombine before reaching the electric field. If a load is added to the circuit, however, charge extraction is hindered. Once the collection rate decreases to below the photogeneration rate, excess minority carriers accumulate on each side of the depletion region, gradually splitting the quasi-Fermi levels and building up a polarity opposed to the applied potential drop. Charges diffuse more and more through the potential barrier, causing J_{diff} to increase and thus the total current to decrease. The recombination probability (or recombination rate) is strongly dependent on the amount of excess carriers, until equilibrium is reached to satisfy:

$$J_{ph} - J_{rec} - J = 0 \quad (2.10)$$

with J_{rec} being the overall recombination current and J the current leaving the cell. This dictates that photogenerated charges, which are not extracted, will necessarily recombine. Under *open circuit conditions* (infinite load), excess charges are confined in the device, and equilibrium is reached when the generation and recombination rates match each other. Under these conditions, the maximum carrier density is reached on each side of the depletion region, and the quasi-Fermi levels are separated by an energy qV_{oc} , where V_{oc} represents the device's maximum achievable electrical potential.

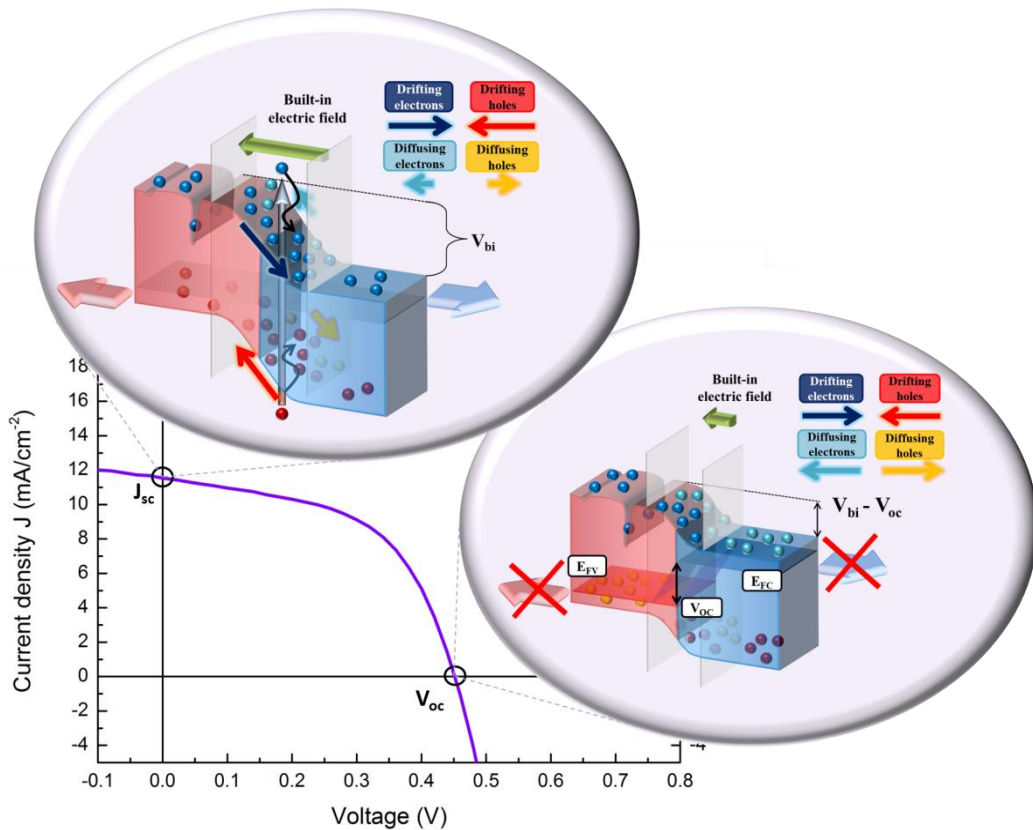


Figure 2.8 – $J - V$ of a solar cell under illumination. The band bending and charge distribution are schematically illustrated for the short circuit (top inset) and open circuit (right inset) conditions.

2.2.3 – Solar cells characteristics: ideal vs. real

The current density – voltage ($J - V$) characteristic of a solar cell gives the principal information regarding its performance. The short-circuit current density (J_{sc}) represent the maximum current that can be collected through the device and reflects the output of a bundle of properties such as photo-absorption, injection/diffusion, junction engineering, and defect/impurity levels. J_{sc} will depend on:

- how strongly does the active material absorbs light;
- the competition between the injection from the absorbing material to the transport material (can be the same) and the back recombination process;

- the potential distribution through the cell, so charge transport is not hindered by potential barriers/wells due to work function mismatch;
- the probability that charges will encounter a recombination centre (defect/impurity/surface state) before extraction.

For optimally engineered solar cells, the short-circuit current density can be approximated as:

$$J_{sc} = qG(L_N + W + L_P) \quad (2.11)$$

where G, W, L_N and L_P are the charge generation rate (includes absorption spectrum and injection rate), the depletion region's width, and the diffusion lengths of minority carriers (electrons and holes), respectively.

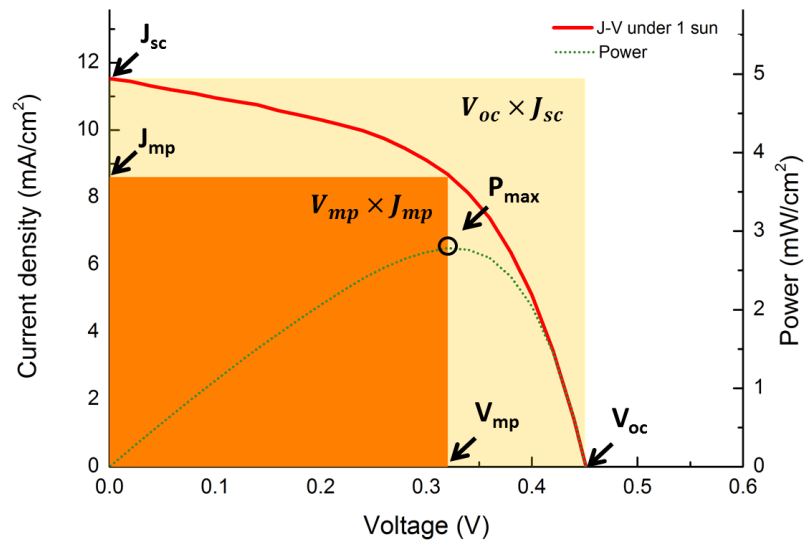


Figure 2.9 – $J - V$ of a solar cell under illumination, emphasizing the main parameters.

Figure 2.9 shows a typical $J - V$ curve emphasizing the most relevant data. One determines the maximum power, P_{max} , coordinates (V_{mp}, J_{mp}) by plotting the power curve $P = V \times J$. This will indicate under which regime the solar cell should operate in order to optimize its output. From this value can be obtained the *fill factor* (FF):

$$FF = \frac{V_{mp} \times J_{mp}}{V_{oc} \times J_{sc}} = \frac{P_{max}}{V_{oc} \times J_{sc}} \quad (2.12)$$

which indicates how “square” the solar cell response is. Higher fill factors relate to more ideal devices and result in higher output for similar (V_{oc}, J_{sc}) .

The device efficiency is the ratio between the maximum power output and the power input (from the solar spectrum):

$$\eta(\%) = 100 \times \frac{P_{max}}{P_{in}} \quad (2.13)$$

with $P_{in} = 100mW/cm^2$ for the 1.5 AM standard.

Most solar cells are less “ideal” than the ones described by Equation 2.9. In order to account for the multiple power losses, the equation can be re-written as:

$$J = J_{ph} - J_0 \left(e^{\frac{q(V+R_s J)}{n_{id} k T}} - 1 \right) - \frac{(V+R_s J)}{R_{sh}} \quad (2.14)$$

With n_{id} , R_s and R_{sh} being the ideality factor, and the series and the shunt resistance, respectively.

Ideality factors can give some steady-state information on the overall performance dependence on various recombination mechanisms. It can be approximated from a series of V_{oc} measurements at different light intensities L . Assuming a linear dependence between L and J_{ph} , and a relatively high shunt resistance, one can obtain:

$$n_{id} \approx \frac{q}{k_B T} \frac{dV_{oc}}{d \ln(L)} \quad (2.15)$$

2.3 - Quantum dots: properties and synthesis

Quantum dots (QDs) are small crystals (or nanocrystals) with electronic properties differing from those of their bulk counterpart due to their small size. This section summarizes their properties of interest in the context of solar cells, their synthesis, and their role in different photovoltaic device architectures.

2.3.1 – Confinement in quantum dots

The most basic example to introduce confinement in quantum mechanics is the particle in a box. Solving the Schrödinger equation for the single dimension case with infinite potential boundaries reveals that the available energy levels in the box⁴ are limited to:

$$E_n(k_n) = \frac{\hbar^2 k_n^2}{2m} = \frac{n^2 \hbar^2 \pi^2}{2mL^2} \quad (2.16)$$

where \hbar , m , and L are the reduced Planck constant, the particle mass, and the size of the box, respectively. k_n is the wavenumber, and n is an integer justifying mathematically the terms “discrete” energy levels. The energy between E_n and E_{n+1} will increase as the size of the box L decreases.

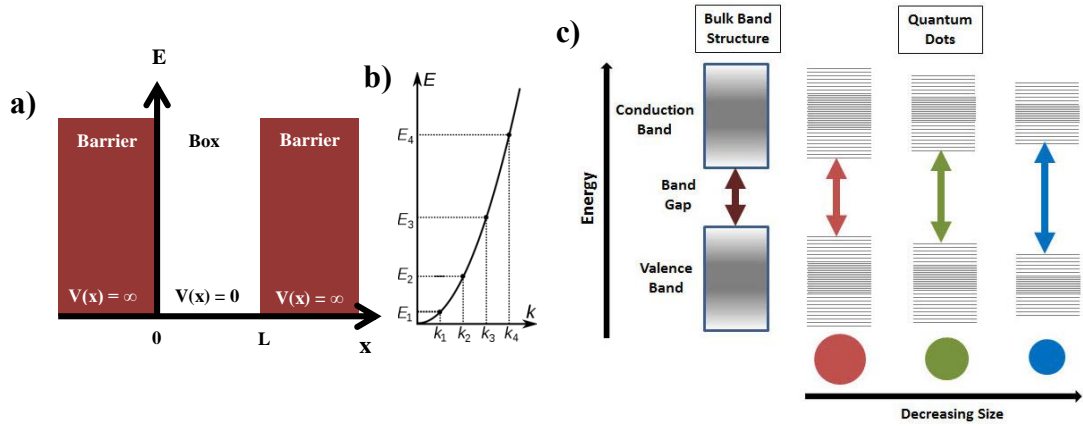


Figure 2.10 – (a) Schematic representation of a box framed by infinite potential boundaries; (b) graphical representation of the authorized states (k_n, E_n) satisfying Equation 2.17; (c) schematic diagram showing how the band gap increases by decreasing the crystal size (Sigma-Aldrich.com).

QDs are semiconducting nanocrystals that are small enough to restrict their electrons to a confinement regime. Conventionally, the size of this three-dimensional box needs to be equal to or less than to the “exciton Bohr radius” a_{exc} in order for its electrons to be subject to the “strong confinement regime”:

$$a_{exc} = \frac{a_0 \epsilon_r}{m^*/m_0} \quad (2.17)$$

With $a_0 = 0.529 \text{ \AA}$, ϵ_r , $m^* = \left(\frac{1}{m_e} + \frac{1}{m_h}\right)^{-1}$, and m_0 being the hydrogen atom’s Bohr radius, the relative permittivity constant of the material, the electron-hole reduced mass, and the free electron mass, respectively. In the case of lead sulfide quantum dots with $m_e = m_h = 0.08m_0$ and $\epsilon_r = 17.2$, we obtain $a_{exc} = 21.4 \text{ nm}$. This value remains a first approximation, as it does not take into consideration the confinement due to the dielectric properties of the crystal. Various factors, however, will be responsible for modifying the boundary potential seen by the confined charge in a nanocrystal and thus, affecting the energy states distribution, such as:

- **Shape symmetries** (or asymmetries) which are not perfectly square or spherical;

- **Reconstruction**, making the surface different from the bulk lattice and smoothening the potential edges;
- **Affinity with the external environment**, allowing electronic orbitals to overlap and confined charge to be delocalized outside of the crystal;

2.3.2 – Tunable band gap

Below the quantum confinement limit, variations in energy level position will become significant. Louis Brus⁵ determined the effective mass model:

$$E_{G,QD} = E_{G,Bulk} + \frac{\hbar^2 \pi^2}{2m^* R^2} - \frac{1.8q^2}{\epsilon_{QD} R} + \text{polarization terms} \quad (2.18)$$

where R and ϵ_{QD} are the radius of the particle and the dielectric constant of the QD, respectively. Lead chalcogenides quantum dots, however, have relatively high dielectric constant and small band gaps. The common approximations to solve the Schrödinger equation don't hold anymore, and the model deviates from real experimental data for crystal sizes under 10 nm (see Figure 2.11). Wang et al. developed a hyperbolic model⁶ overcoming this divergence and rewrote the equation as:

$$E_{G,QD} = \sqrt{E_{G,Bulk}^2 + \frac{2\hbar^2 E_{G,Bulk}}{m^* R^2}} \quad (2.19)$$

Another method was later proposed by Kang *et al.* using a complex 4-band model^{7, 8} using the k·p Hamiltonian:

$$E_{Vac,QD} = E_{k\cdot p} + \left(1 - \frac{1}{\epsilon_{QD}}\right) \frac{q^2}{2R} + \chi_{bulk} \quad (2.20)$$

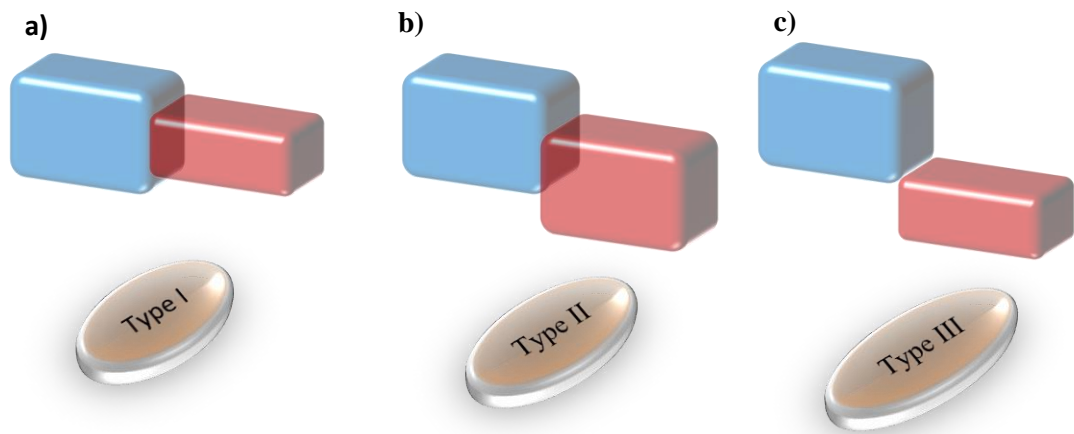


Figure 2.12 – Schematic representation of heterojunctions of type I (a), II (b) and III (c)

2.3.3 – Electron-hole pairs, excitons

In Section 2.1.2, it was taken for granted that the final state of an excited electron was “in” the conduction band, leaving a hole behind in the valence band. This “electron-hole pair” state governs electronic transport in most of the bulk semiconductor devices where both charges are swept away from each other by the electric field in the depleted region. In reality, however, the band gap is relevant for macroscopic materials where the long range periodicity indicates that the electronic properties remain locally the same, wherever the charges are. In nanostructured devices, many new factors must be taken into account: crystal boundaries, the shape effect, matrices of two or more components, and interface tunnelling or confinement. The defects introduce perturbations which result in potential wells, potential barriers and mid-gap states.

For example, in certain crystals with high dielectric constants, the Coulomb interaction between electrons and holes is screened. Thus, the two charges become weakly bonded and form a quasi-particle called an “exciton”. Its energy state can be

calculated by using the Schrödinger equation for the hydrogen atom, and by simply replacing the masses of the proton and the electron by the effective masses of the hole and the electron from the material considered, respectively. In bulk materials, the excitonic levels are located just below the conduction band (see Figure 2.13), reflecting the Coulomb interaction. Excitons have no charge, but can move in a medium until they receive enough energy to split (even $\Delta E \approx k_B T$ at room temperature for bulk

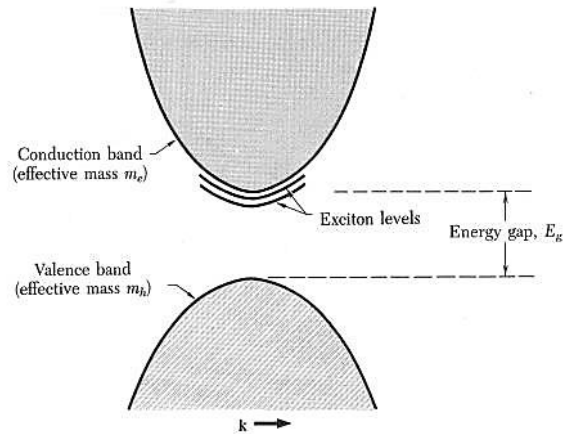


Figure 2.13 – Schematic representation of excitonic levels located in the band gap.

materials). In isolated quantum dots (such as PbS quantum dots), it is well established that since the excited electrons and holes are spatially confined, there is no “free charge” state, and the whole transitional spectrum is entirely dictated by excitonic levels.⁹⁻¹³

2.3.4 – Relaxation dynamics, hot carriers, and multiple exciton generation

If an electron absorbs a photon with an energy above the energy of the lowest exciton energy (generally referred as $1S_h-1S_e$), various pathways can be followed:

- 1) the electron can relax to its lowest state by dissipating energy as heat through electron-phonon interaction or the Auger process;

- 2) the excess energy can be transferred to excite one or more electrons through the reverse Auger process, leading to multiple exciton generation (MEG);
- 3) the electron-hole quasi-particle can split, leaving a highly energetic charge (hot carrier) that must be extracted before recombining.

The first pathway results in an obvious energy loss (Shockley-Queisser limit) and is still the dominant fate of excited charges because of its extremely fast occurrence in bulk semiconductors (\sim several ps). Theoretical models have shown that these processes can be slowed down by increasing the photogenerated carrier density up to $\sim 10^{18} \text{ cm}^{-3}$ to induce a “hot phonon bottleneck” due the non-equilibrium distribution of longitudinal optical (LO) phonons.^{14, 15} Later on, Arthur J. Nozik emphasized the potential of this effect if applied in optoelectronic devices.¹⁶⁻¹⁸ This process is still limited by crystal momentum which must be conserved during the transitions. The result is that no MEG is observed before $h\nu > 4E_G$. Further experiments, however, were carried out on QDs at light intensities similar to the solar irradiation on earth demonstrated that certain confined structures were showing similar behaviour at much lower photogenerated charge density.¹⁹⁻²¹

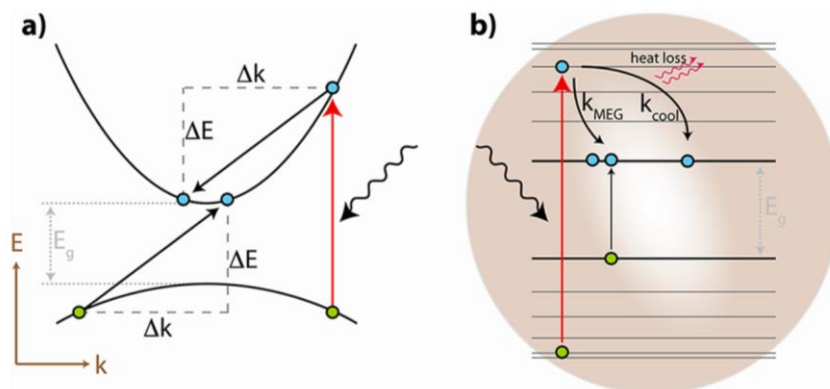


Figure 2.14 – Fast relaxation in continuous energy levels (δE) and conservation of crystal momentum (Δk) in bulk semiconductors (a) versus MEG in nanocrystals (b) (Beard *et al.* 2012).

Because of their small size, nanocrystals do not suffer from the problem of conservation of momentum which is inherent to the long range periodicity (Figure 2.14). These assumptions are based on the idea that if the energy separation between two discrete exciton levels is higher than the fundamental phonon energy, than a multiple-phonon process would be required in order for the charge to relax to the lowest level. These mechanisms are significantly slower than single phonon interactions, and their relaxation time could be estimated from:

$$\tau_c \approx \omega^{-1} \exp(\Delta E/k_B T) \quad (2.21)$$

where τ_c is the hot carrier cooling time, ω is the phonon frequency and ΔE is the energy separating the two discrete energy levels. According to Equation (2.21), strongly quantized levels (> 0.2 eV) would stretch the relaxation time to ~ 100 ps. Using ultra-fast transient absorption (TA) spectroscopy or time-resolved photoluminescence decay (TRPL)²²⁻²⁴, Schaller *et al.* observed different decaying components, which they associated with single- and multiple-excitons.

These phenomena, when applied at full potential in solar cells technology,^{25, 26} are expected to improve the Shockley-Queisser limit (Figure 2.15) from 33.7% to 45% (for MEG)²⁷ and to 67% (for hot carriers)²⁸. These measurements were performed on individual nanocrystals under controlled conditions, however. The challenge of incorporating QDs into a photovoltaic device while

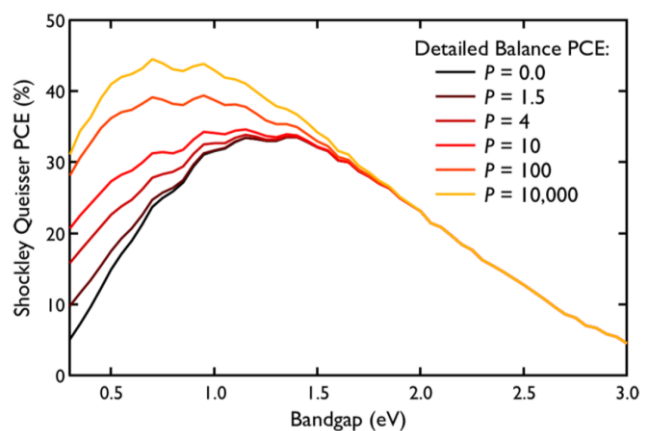


Figure 2.15 – Theoretical improvement of the Shockley-Queisser limit due to the MEG efficiency P (Beard *et al.* 2012).

benefiting from their MEG²⁹⁻³² or hot carrier³³ mechanisms are still attracting a lot of attention.

2.3.5 – Synthesis

Different methods have been developed to produce QDs from different materials, with different shapes, sizes and size distributions for various applications. Physico-chemical vapour deposition techniques involve the formation of the materials directly on the substrate, giving an improved control of the size and spatial distribution. They are especially appropriate in the development of superlattices which amplify quantum electronic confinement properties.³⁴⁻³⁷ On the other hand, wet chemical techniques provide good alternative routes to producing QDs in a colloidal suspension with a proper 3-dimensional confinement characteristic. These methods typically use standard glassware with temperatures limited to 300°C, leading to significantly lower production costs.

2.3.5.1 – Physical vapour deposition

A typical method to grow a 3-D structure through vapour phase deposition is Stranski-Krastinov growth.³⁸⁻⁴⁰ By depositing several monolayers of one semiconductor upon another which has a strong lattice mismatch with the former,

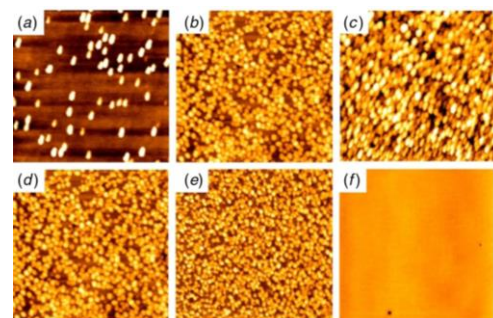


Figure 2.16 – AFM images of InAs island growth for different In:As ratios (by Benyoucef *et al.*).

epitaxial growth is initiated in a layer-by-layer fashion and forms 3D islands.⁴¹ These structures can then grow coherently (see the atomic force microscope (AFM) images in Figure 2.16).

Another method is vapour-liquid-solid (VLS) deposition.⁴²⁻⁴⁵ Initially, a thin film of gold (1-10nm) is deposited onto a silicon wafer (100) and then heated above the Au/Si eutectic point to form droplets of Au-Si alloy on the surface of the substrate. The sample is then brought into a vacuum chamber with a flow of reactive gas mixture (typically SiCl₄:H₂) at 800°C. The droplets, acting as a catalyst to lower the activation

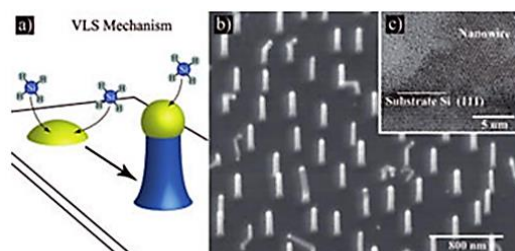


Figure 2.17 – (a) Schematic of VLS mechanism. Low (b) and high (c) resolution TEM images of Si nanowires (by Ren *et al.*).

energy of normal vapour solid growth, absorb the gas until the supersaturated state is reached, after which, excess Si atoms are automatically driven down to the substrate, leading to anisotropic growth (see Figure 2.17).

2.3.5.2 – Successive Ionic Layer Adsorption and Reaction (SILAR)

Vogel *et al.* was the first to use develop the sensitization of wide-band-gap semiconductors with different binary sulfides semiconductor nanoparticles through chemical bath deposition.⁴⁶ The method was rebaptised later on as SILAR in

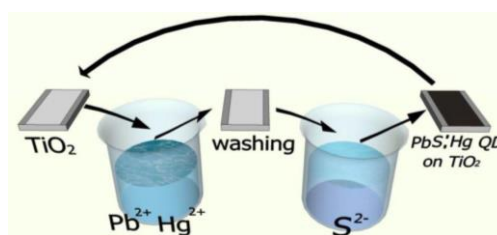


Figure 2.18 – Example of SILAR experimental setup to produce Hg²⁺ doped PbS QDs (by Lee *et al.* 2013).

order prevent confusion with other types of chemical bath deposition techniques. The technique consists of immersing the substrate in a saturated aqueous solution of nitrate

salt (in this case lead nitrate), rinsing, immersing in an aqueous solution of sodium sulfide (Na_2S), and rinsing again (see example in Figure 2.18). The deposition can be optimized by varying the immersion time, the number of repetitions, and the type of salts or their concentration. The number of “seeds” deposited during the first cycle is the limiting factor, however, because any subsequent steps will only involve growing the crystallites without adding new ones. Direct growth on the substrate (as in Section 2.3.5.1) has the advantages of increasing the cohesion of the sensitizer and improving electron injection at the same time. This method, which is exclusively used for quantum dot sensitized solar cells, suffers still from certain drawbacks which will be discussed in Section 2.4.1.1.⁴⁷

2.3.5.3 – Colloidal growth synthesis

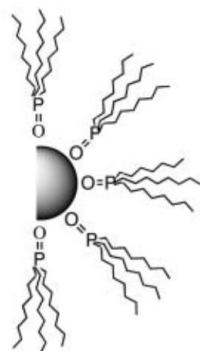


Figure 2.19 – tri-n-octylphosphine oxide capped QD. (Jin *et al.* 2005).

Since Faraday synthesized gold colloidal nanoparticles in 1857,⁴⁸ many chemical routes were developed in order to obtain such nanostructures in a wide range of binary materials. A typical method involves the encounter of two (or more) precursors, generally from groups II/VI or IV/VI, in a hot solvent containing coordinating molecules under vigorous stirring. A considerable number of nucleation centres are formed initiating growth of the particles through Ostwald ripening. The role of the coordinating ligands is to set a critical crystal size, after which, growth is hindered.⁴⁹⁻⁵¹ This leads to a narrowed size distribution, where the mean size can be empirically controlled through parameters such as the precursor ratio, ligand concentration, temperature and reaction time.

Murray *et al.* developed and modernized this technique in IBM's laboratory, leading to the standard recipes to synthesize cadmium chalcogenides⁵²⁻⁵⁴ and lead chalcogenides.⁵⁵ These methods used tri-n-octylphosphine (TOP) to dissolve the chalcogen (S, Se, Te) precursor and tri-n-octylphosphine oxide (TOPO) as the coordinating ligand (Figure 2.19). They also introduced the lead oleate-bis(trimethylsilyl)sulfide precursor combination to produce PbS quantum dots in hot diphenyl ether (boiling point ~260°C). Nowadays, researchers have adopted the Hines and Scholes method,⁵⁶ in which the toxic diphenyl ether is replaced by 1-octadecene (boiling point 315°C). Further washing process are required to extract the quantum dots from the reaction solution. The final product is still capped with oleate (or TOPO) molecules making it stable in non-polar solvents, hence the name colloidal quantum dots (CQDs). Parameters such as injection temperature and reaction time can easily lead to a wide range of nanoparticle sizes, and thus a wide range of band gaps with different emission wavelengths (Figure 2.20).



Figure 2.20 – ZnCdSeS quantum dots with various sizes emitting at various wavelength (PlasmaChem).

2.4 – Quantum dots for photovoltaic application

QDs show unique optoelectronic properties due to their extreme confinement, including a high extinction coefficient allowing thin layers to absorb a considerable of photons.⁵⁷ There has been considerable research with the aim of designing devices for the purpose of optimizing photoabsorption and charge transport/collection while

maintaining a high voltage output. Various architectures are used as scaffolds for the researchers to observe the effects of new materials and new treatments, and to analyse the fundamentals of electronic transport in such devices.

2.4.1 – Typical device types and architectures

In this section, three types of architectures are reviewed: the quantum dot sensitized solar cell, the colloidal quantum dot schottky junction solar cell and the colloidal quantum dot heterojunction solar cell.⁵⁸ Other strategies have more recently been investigated, however, such as hybrid cells (see Figure 2.21) blending colloidal quantum

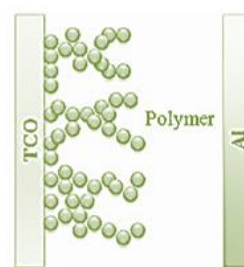


Figure 2.21 – Hybrid Polymer/QDs solar cell (Emin *et al.* 2011).

dots with polymers,⁵⁹⁻⁶² fullerenes,^{63, 64} graphene,^{65, 66} or carbon nanotubes.⁶⁷

2.4.1.1 – Quantum Dot Sensitized Solar Cells (QDSCs)

Inspired by their organic analogue (dye sensitized solar cells, DSCs), the sensitizers from QDSCs (Figure 2.22(a)) are generally grown through SILAR deposition (see Section 2.3.5.2) and are selected for their high extinction coefficient. The operation mechanism can be observed from the band diagram in Figure 2.22(b). Briefly, a photon is absorbed in one QD, generating an exciton. The electron and hole dissociate at the interface with a TiO₂ particle. The electron is injected into the TiO₂, resulting in the oxidation of the QDs, and transported to the working electrode, generally made of a transparent conductive oxide (TCO). The hole recombines with

an electron from the redox medium and regenerates the ground state. The system is at equilibrium once the oxidized electrolyte diffuses to the counter electrode where it will be reduced.

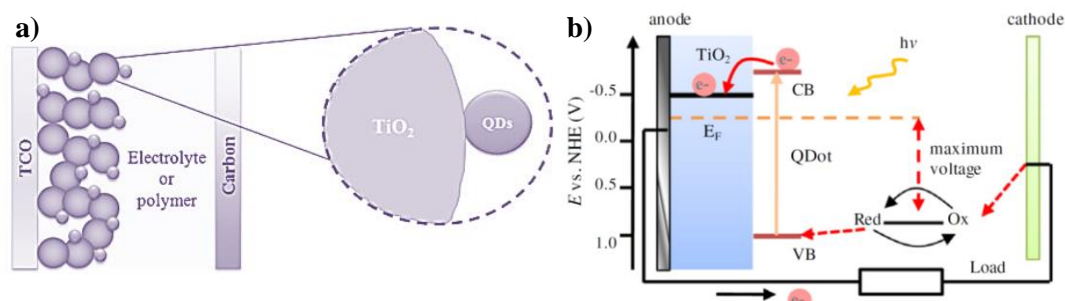


Figure 2.22 – Quantum dot sensitized solar cell: architecture (a) and band structure (b) (Emin *et al.* 2011).

Typical electrolytes in DSCs use the iodide/triiodide redox couple, appears to be a reactive source of corrosion for sensitized QDs. Other compositions, including polysulfides dissolved in methanol,⁶⁸ cobalt complexes⁶⁹ or solid state hole conductors such as (2,2,(7,7-(tetrakis-(N,N-di-pmethoxyphenylamine) 9,9-(spirobifluorene) (spiro-OMeTAD)).⁷⁰ As in DSCs, the main pathway for photogenerated carriers to recombine in QDSCs is from the TiO₂ particles to the redox couple from the electrolyte.^{71, 72} This comes from the low coverage efficiency during the SILAR deposition. A ZnS coating efficiently screens this back-recombination mechanism, but it introduces new monoenergetic surface states affecting the fill factor.⁷³ Various other strategies are still being investigated.⁷⁴⁻⁷⁸ The latest devices sensitized with PbS quantum dots showed a significantly high short-circuit current (38 mA/cm²), leading to an overall efficiency of 5.6%.⁷⁹

2.4.1.2 – CQD Schottky Junction Solar Cell (SJSC)

The CQD Schottky junction solar cell was the first to achieve efficiencies above 1% from CQDs.^{67,68} The architecture (see Figure 2.23) is based on stacking a large work function TCO (such as indium-doped tin oxide) with a film of *p*-type CQDs to form an Ohmic contact. This is followed by evaporating a shallow work function metal (aluminium, magnesium) to create the appropriate band-bending to extract electron while repelling holes.

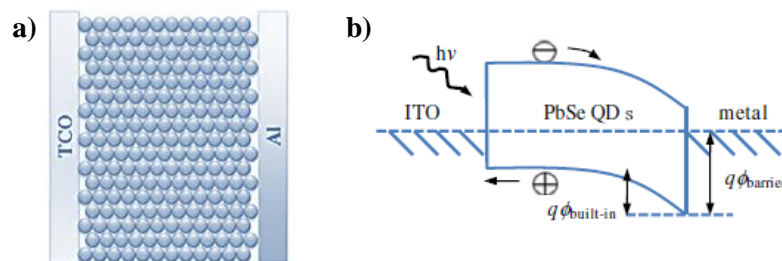


Figure 2.23 – Colloidal quantum dot Schottky junction solar cell: architecture (a) and band structure (b) (Emin *et al.* 2011).

This attractive strategy had, however, a few drawbacks. The short diffusion length in these films limits their thickness to 200 nm, which is too thin to absorb more of the entire available radiation. Increasing the thickness of the device above this critical limit causes the charges to recombine before reaching the electrodes. Also, defect states at the metal/semiconductor interface tend to pin the Fermi level affecting the overall open-circuit voltage. Nevertheless, the optimization of the material synthesis, the post-treatments, and the assembly,⁸⁰ along with the use of hole-selective contacts, led Piliago *et al.* to produce devices with an efficiency of 5.2%.⁸¹

2.4.1.3 – CQD Depleted Heterojunction Solar Cell (DHJSC)

This architecture has similar features to the CQD SJSC (Figure 2.24(a)). It has an additional *n*-doped layer of wide-band-gap semiconductor particles (TiO₂, ZnO) between the TCO electrode and the CQD layer to ensure electron transport (Figure 2.24(b)), while the back contact is made of a metal with a large work function (such as Au or Pt).

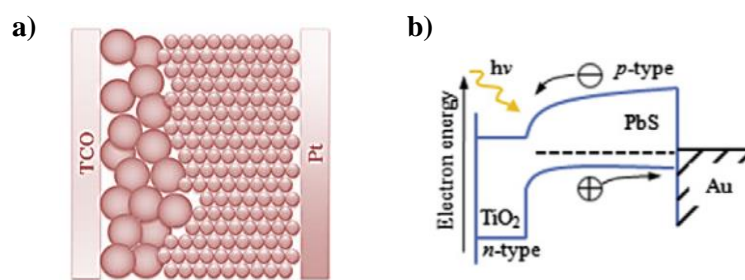


Figure 2.24 – Quantum dot heterojunction solar cell : architecture (a) and band structure (b) (Emin *et al.* 2011).

As compared to the Schottky junction, the heterojunction provides more efficient electron-hole dissociation. Back electron transfers from the oxide to the CQD layer being suppressed by the built-in field. High open-circuit voltage can be achieved because of the large difference between the Fermi level position in TiO₂ and the work function of the counter electrode. Finally, because the dissociative junction is on the illuminated side, carrier separation happens faster. The first DHJSC⁸² was reported in 2010 with an efficiency of 5.1%, far above the records achieved by other architectures at the time. These high performances were partly due to optimized parameters such as: CQD synthesis, size selection, ligand exchange and film thickness (both for TiO₂ and PbS CQDs). Further improvement, including controlled oxide doping^{83, 84} and inorganic passivation, stretched the performance of these devices up to 7.4%.^{85, 86} Ultimately, replacing the wide-band-gap oxide by *n*-doped CQD film and stacking

films with different QD size would lead a tandem structure for this sort of device⁸⁷⁻⁹⁰ to increase the absorption range.

2.4.2 – The role of the ligands

Ligands are ions or molecules⁹¹ coordinating with a metal atom. In the context of nanoparticle chemistry, the ligand forms a bond with a surface atom where the volume periodicity is broken and fulfils three main roles: passivation, functionalization, and steric spacing.

The term “passivation” literally means to make a material less reactive to its environment. The surfaces of nanoparticles can be very unstable due to strains, uncontrolled reconstruction, or unbalanced charge. These unstable sites are ready to bond with anything so as to relax to a lower surface energy state. The most common contaminants are the native oxides formed from oxygen and moisture in air. These species can have significantly detrimental influence on the particle properties by adding new surface states (generally mid-gap states) to the overall crystal energy structure. These levels can pin the Fermi level down (and be responsible for lowering the open-circuit voltage) or even act as deep traps and recombination centres. Passivating the surface involves introducing ligand molecules to coordinate with the unstable sites by inducing minimum change in the energy state distribution, while preventing other adventitious contaminants from being adsorbed.

Functionalization is a broad term, as it includes any modification in the physical or chemical reactivity of the material. In the context of biotechnology (see

Figure 2.25), QDs can be functionalized to improve their biocompatibility⁹² or can act as a chromophore functional groups to make certain cells or proteins fluorescent.⁹³

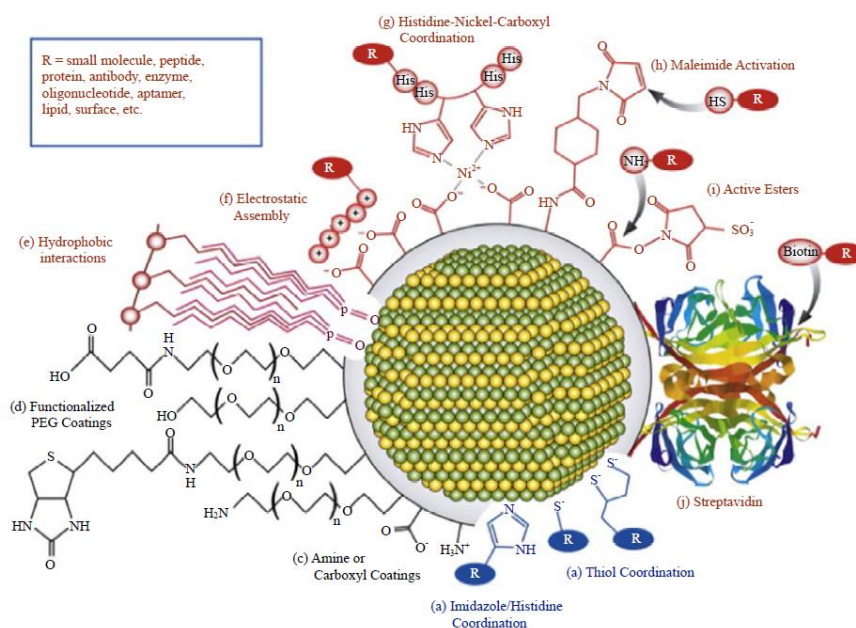


Figure 2.25 – Schematic illustration showing various type of organic ligands with functional groups for biotechnology applications (Algar *et al.* 2010).

For PbS CQD based solar cells, the nanoparticles are coated with oleate ligands having long non-polar hydrocarbon chains, giving the material the ability to be suspended in non-polar solvents (alkanes, toluene, and chloroform). This property makes CQDs easier to deposit on substrates through spin-coating, dip-coating or even potential screen- and inkjet-printing techniques.⁹⁴

In order for QDs to retain their confined optoelectronic properties, they must maintain a certain degree of isolation in order to prevent the electron wave function from delocalising in neighbouring nanocrystals. The loss of confinement leads to uncontrolled and non-uniform energy level reconfiguration, where the first exciton transition is reduced and the energy levels regain their continuous character (from the bulk). Electrons from completely remote nanoparticles, however, have a very low

hopping probability and thus suffer from low conductivity. After being cast on a solid surface, ligands of various lengths provide various steric spacing between the QDs and a balance must be found between confinement and conductivity. For this reason, CQD films are generally made through a layer-by-layer process, where in each cycle, long chain ligands are exchanged for shorter ones (see Figure 2.26).

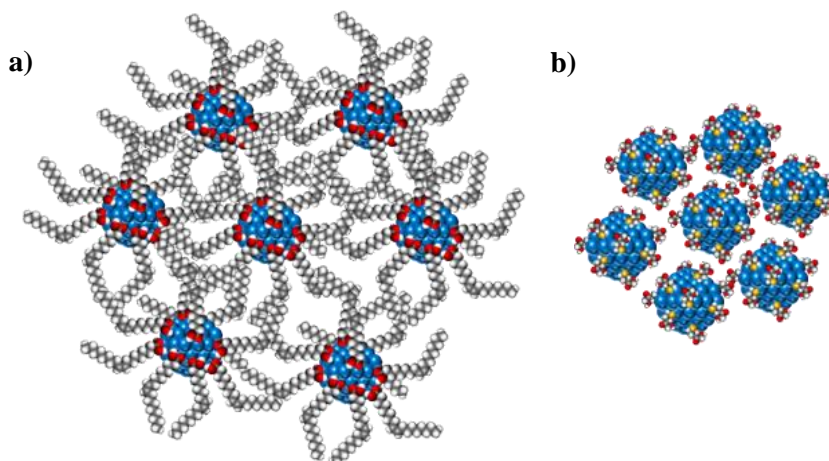


Figure 2.26 – Representation of steric spacing between CQDs when using (a) oleic acid or (b) 3-mercaptopropionic acid. Colour codes are as follow: oxygen: red, carbon: grey, hydrogen: white and sulfur: yellow.

Ligand exchange could be categorized in two groups: organic and inorganic ligand exchange.

2.4.2.1 – Organic ligand exchange

Replacing oleate molecules with short ionic dithiol ligands such as 1,2-ethanedithiol (EDT) and 1,3-benzenedithiol (BDT) showed promising results for PbS CQD films.⁹⁵⁻¹⁰⁰ Certain groups have reported poor resistance to ambient atmospheric conditions,^{101, 102} however, while 3-mercaptopropionic acid (MPA) seems to result in better stability, improved mobility, and is less influenced by possible trap states for similar interparticle spacing (Figure 2.27).^{103, 104} Jeong *et al.* suggested that the greater

chemical diversity of MPA (thiol + carboxylic groups) in comparison to EDT could passivate a broader distribution of surface states.

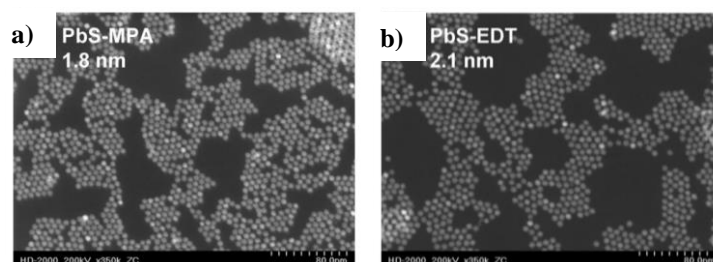


Figure 2.27 – Scanning transmission electron microscope images CQDs after MPA (a) and EDT (b) ligand exchange (Jeong *et al.* 2012).

It was also suggested that substituting the oleate group for oleylamine¹⁰⁵ or octylamine¹⁰⁶ through a 3-day solution-phase ligand exchange prior to the MPA or EDT solid phase exchange made it possible to achieve a more effective replacement and improved passivation.

2.4.2.2 – Inorganic ligand exchange

Because of the bulkiness of the organic ligand exchange as well as their vulnerability to thermal degradation and oxidation, other researchers have aimed to develop inorganic ligand strategies. Talapin's group started by using $\text{Sn}_2\text{S}_6^{4-}$ ions to cap various types of quantum dots (CdSe, CdTe, CdS, Bi_2S_3 , Au, Pd)^{107, 108} and extended this work further with a wider range of inorganic ligands (Figure 2.28).¹⁰⁹ This successful method looks promising and has already shown good electronic properties for device applications. Only photoconductivity

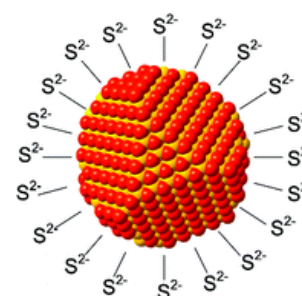


Figure 2.28 – S^{2-} inorganic capping by the Talapin group (Nag *et al.* 2011).

experiments were performed on CdSe passivated QD films, however, no real photovoltaic device has been reported to date.

Tang *et al.* successfully developed an inorganic halide ligand passivation method (Figure 2.29).⁸⁵ A first step consisted of improving passivation due to surface sulfur dangling bonds by treating the quantum dots in a mixture of

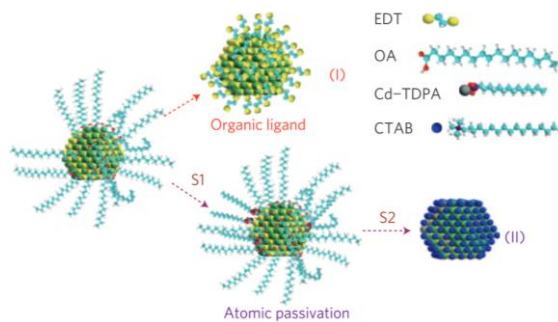


Figure 2.29 – Atomic-ligand passivation developed by (Tang *et al.* 2011).

tetradecylphosphonic acid, CdCl₂, and oleylamine (60 °C, 5 min). This improved stability and the size distribution removes certain surface defects. The spin-coating layer deposition took place in a glove box where each layer was then post-treated

with solutions of cetyltrimethylammonium bromide (Br⁻), hexadecyltrimethylammonium chloride (Cl⁻), or tetrabutylammonium iodide (I⁻). These treatments led to significant improvement of device performances.^{110, 111} Thon *et al.* also performed *ab initio* calculations to calculate the evolution of mid-gap trap-states after such a passivation strategy.¹¹² Further optimisation by Ip *et al.* led to the best performing device to date with an efficiency of 7.4 %.⁸⁶

Other promising methods include atomic chlorine ligand passivation (Figure 2.30), leading to relatively good electronic transport.^{113, 114} Zhang *et al.* completely removed the oleate ligand using ammonium sulfide.¹¹⁵ They report that the remaining

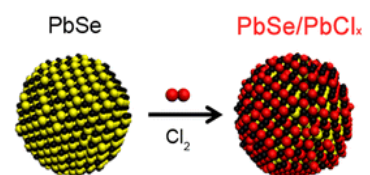


Figure 2.30 – Atomic-chlorine passivation (Bae *et al.* 2012).

QDs were self-passivated and interconnected through metal-sulfide bonding. Using microwave conductivity transients, Cate *et al.* observed the activation of carrier

multiplication after infilling PbSe films with Al₂O₃ or Al₂O₃/ZnO by atomic layer deposition. None of these methods have as yet been implemented in photovoltaic devices, however. Kinder *et al.* produced a matrix of PbS QDs encapsulated in a CdS matrix, creating a quasi-superlattice. They assembled various solar cells that could reach an efficiency of 2.4%.

2.4.3 – Transport in CQD Depleted Heterojunction Solar Cells

Many publications now give notions of “selective contacts” instead of heterojunctions. Mora-Sero *et al.* observed clearly how the choice of material can literally filter charges (fluorine doped tin oxide FTO, Au and poly(3,4-ethylenedioxythiophene) (PEDOT) for holes; TiO₂ and ZnO for electrons).¹¹⁶ Engineering the interface between PbS CQDs and the electron selective contact by various choices of materials and doping techniques has attracted considerable attention.¹¹⁷⁻¹²¹ Improving the hole collection was achieved using LiF in Schottky devices,¹²²⁻¹²⁵ while DHJSC shows better results using MoO_x (see Figure 2.31).^{126, 127} The reasons for this enhancement are still discussed, as very deep-lying energy levels and exceptionally large work function¹²⁸ seem to only be a part of the explanation. Gao *et al.* also observed that hole injection could be controlled through Schottky barrier engineering.¹²⁹ This could be achieved by matching the work function of the metal and the energy bands of PbS CQDs with specific sizes.

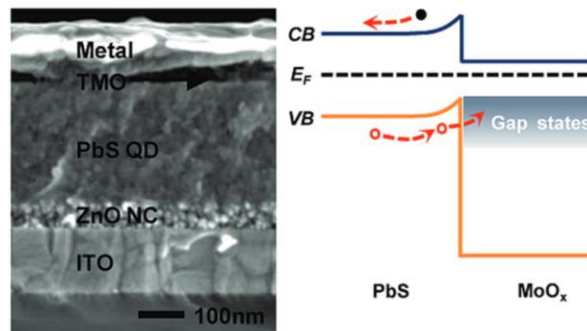


Figure 2.31 – SEM cross-section and band structure of a device with MoO_x selective contact (Gao *et al.* 2011).

Bakulin *et al.* observed the presence of trap states with various depths (0.3-0.5 eV) below the conduction band that were responsible for charge immobilization and poor charge separation (see Figure 2.32).¹³⁰ Using 1D- and 3D- models, Zhitomirsky determined the lifetime, trap density, mobility, and diffusion coefficient by simply taking into consideration the geometry of the device and its photoluminescence response.¹³¹ He found that state-of-the-art devices have a diffusion length of 80 nm.

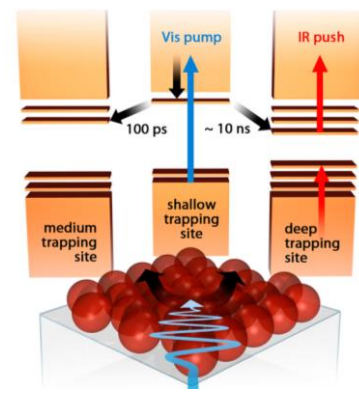


Figure 2.32 – Push pump photocurrent method to probe trap states (Bakulin *et al.* 2013).

Transport in CQD films has been known to be substantially mediated by intraband (in-gap) states which are dependent on the surface passivation.¹³² Using an optical field-effect transistor (OFET) configuration, P. Nagpal and V.I. Klimov described the existence of a “mid-gap band” with different levels of participation, depending on whether the device is in the dark or under illumination (Figure 2.33(a)-(b)). With similar methods, Stadler *et al.* employed sub-threshold analysis to probe the trap distribution and map the density of state distribution in a CQD film.

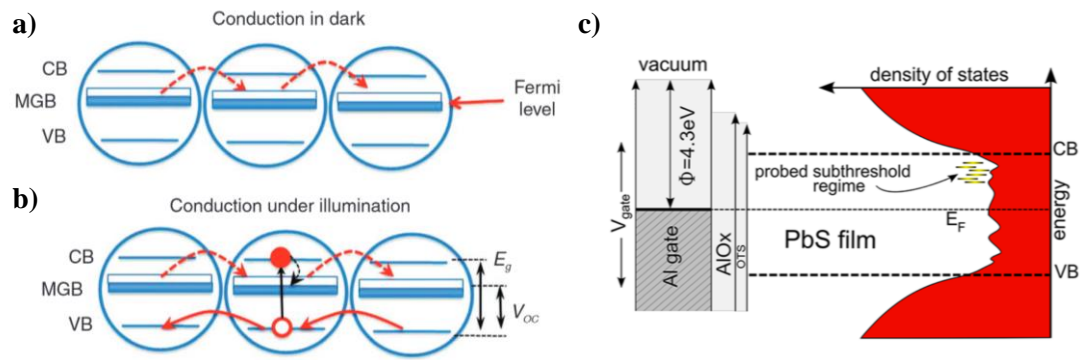


Figure 2.33 – Mid-gap band (MGB) participation in conduction (a) in the dark and (b) under illumination (Nagpal *et al.* 2011).

References

1. Kittel, C., *Introduction to Solid State Physics*, 7th ed. 2007: Wiley India Pvt. Limited.
2. G173, A.S. *Standard Tables for Reference Solar Spectral Irradiances: Direct Normal and Hemispherical on 37° Tilted Surface*. 2012 [cited 2014; Available from: www.astm.org].
3. Shockley, W. and H.J. Queisser, *Detailed Balance Limit of Efficiency of p-n Junction Solar Cells*. *Journal of Applied Physics*, 1961. **32**(3): p. 510.
4. Griffiths, D.J., *Introduction to Quantum Mechanics*. 2005, Upper Saddle River, NJ: Pearson Education.
5. Chestnoy, N., et al., *Luminescence and photophysics of cadmium sulfide semiconductor clusters: the nature of the emitting electronic state*. *The Journal of Physical Chemistry*, 1986. **90**(15): p. 3393.
6. Wang, Y., et al., *PbS in Polymers - From Molecules to Bulk Solids*. *Journal of Chemical Physics*, 1987. **87**(12): p. 7315.
7. Kang, I. and F.W. Wise, *Electronic structure and optical properties of PbS and PbSe quantum dots*. *Journal of the Optical Society of America B-Optical Physics*, 1997. **14**(7): p. 1632.
8. Hyun, B.R., et al., *Electron Injection from Colloidal PbS Quantum Dots into Titanium Dioxide Nanoparticles*. *ACS Nano*, 2008. **2**(11): p. 2206.
9. Yang, Y., et al., *Strong Electronic Coupling and Ultrafast Electron Transfer between PbS Quantum Dots and TiO₂ Nanocrystalline Films*. *Nano Letters*, 2012. **12**(1): p. 303.
10. Gao, J. and J.C. Johnson, *Charge Trapping in Bright and Dark States of Coupled PbS Quantum Dot Films*. *ACS Nano*, 2012. **6**(4): p. 3292.
11. Fernée, M.J., et al., *Highly efficient luminescence from a hybrid state found in strongly quantum confined PbS nanocrystals*. *Nanotechnology*, 2006. **17**(4): p. 956.

12. Lewis, J., S. Wu, and X. Jiang, *Unconventional gap state of trapped exciton in lead sulfide quantum dots*. *Nanotechnology*, 2010. **21**(45): p. 455402.
13. Wanger, D.D., et al., *The Dominant Role of Exciton Quenching in PbS Quantum-Dot-Based Photovoltaic Devices*. *Nano Letters*, 2013. **13**(12): p. 5907.
14. Bockelmann, U. and G. Bastard, *Phonon scattering and energy relaxation in two-, one-, and zero-dimensional electron gases*. *Physical Review B*, 1990. **42**(14): p. 8947.
15. Benisty, H., C. Sotomayor-Torres, and C. Weisbuch, *Intrinsic mechanism for the poor luminescence properties of quantum-box systems*. *Physical Review B*, 1991. **44**(19): p. 10945.
16. Pelouch, W.S., et al., *Investigation of Hot-Carrier Relaxation in Quantum-Well and Bulk GaAs at High Carrier Densities*. *Semiconductor Science and Technology*, 1992. **7**(3B): p. B337.
17. Rosenwaks, Y., et al., *Hot-Carrier Cooling in GaAs Quantum-Wells vs Bulk*. *Physical Review B*, 1993. **48**(19): p. 14675.
18. Pelouch, W.S., et al., *Comparison of Hot-Carrier Relaxation in Quantum-Wells and Bulk GaAs at High Carrier Densities*. *Physical Review B*, 1992. **45**(3): p. 1450.
19. Williams, F. and A.J. Nozik, *Solid-State Perspectives of the Photoelectrochemistry of Semiconductor Electrolyte Junctions*. *Nature*, 1984. **312**(5989): p. 21.
20. Williams, V.S., et al., *Optical Nonlinearities and Ultrafast Carrier Dynamics in Semiconductor Doped Glasses*. *Journal of Modern Optics*, 1988. **35**(12): p. 1979.
21. Boudreaux, D.S., F. Williams, and A.J. Nozik, *Hot Carrier Injection at Semiconductor-Electrolyte Junctions*. *Journal of Applied Physics*, 1980. **51**(4): p. 2158.
22. Ellingson, R.J., et al., *Highly efficient multiple exciton generation in colloidal PbSe and PbS quantum dots*. *Nano Letters*, 2005. **5**(5): p. 865.

23. Schaller, R.D., et al., *High-efficiency carrier multiplication and ultrafast charge separation in semiconductor nanocrystals studied via time-resolved photoluminescence*. The Journal of Physical Chemistry B, 2006. **110**(50): p. 25332.
24. Schaller, R.D. and V.I. Klimov, *High efficiency carrier multiplication in PbSe nanocrystals: implications for solar energy conversion*. Physical Review Letters, 2004. **92**(18): p. 186601.
25. Nozik, A.J., *Quantum dot solar cells*. Physica E-Low-Dimensional Systems & Nanostructures, 2002. **14**(1-2): p. 115.
26. Beard, M.C., et al., *Third generation photovoltaics based on multiple exciton generation in quantum confined semiconductors*. Accounts of Chemical Research, 2012. **46**(6): p. 1252.
27. Hanna, M. and A. Nozik, *Solar conversion efficiency of photovoltaic and photoelectrolysis cells with carrier multiplication absorbers*. Journal of Applied Physics, 2006. **100**(7): p. 074510.
28. König, D., et al., *Hot carrier solar cells: Principles, materials and design*. Physica E: Low-dimensional Systems and Nanostructures, 2010. **42**(10): p. 2862.
29. Semonin, O.E., et al., *Peak external photocurrent quantum efficiency exceeding 100% via MEG in a quantum dot solar cell*. Science, 2011. **334**(6062): p. 1530.
30. Beard, M.C., et al., *Variations in the quantum efficiency of multiple exciton generation for a series of chemically treated PbSe nanocrystal films*. Nano Letters, 2009. **9**(2): p. 836.
31. Luther, J.M., et al., *Multiple exciton generation in films of electronically coupled PbSe quantum dots*. Nano Letters, 2007. **7**(6): p. 1779.
32. Lee, J.-S., et al., *Band-like transport, high electron mobility and high photoconductivity in all-inorganic nanocrystal arrays*. Nature Nanotechnology, 2011. **6**(6): p. 348.
33. Takeda, Y., et al., *Practical factors lowering conversion efficiency of hot carrier solar cells*. Applied Physics Express, 2010. **3**(10): p. 104301.

34. Nozik, A.J., et al., *Semiconductor quantum dots and quantum dot arrays and applications of multiple exciton generation to third-generation photovoltaic solar cells*. Chemical Reviews, 2010. **110**(11): p. 6873.
35. Okada, Y., et al., *Increase in photocurrent by optical transitions via intermediate quantum states in direct-doped InAs/GaNAs strain-compensated quantum dot solar cell*. Journal of Applied Physics, 2011. **109**(2): p. 024301.
36. Robinson, R.D., et al., *Spontaneous superlattice formation in nanorods through partial cation exchange*. Science, 2007. **317**(5836): p. 355.
37. Yu, P. and M. Cardona, *Fundamentals of Semiconductors: Physics and Materials Properties*. 2010: Springer.
38. Matthews, D., et al., *Experimental investigation of the effect of wetting-layer states on the gain-current characteristic of quantum-dot lasers*. Applied Physics Letters, 2002. **81**(26): p. 4904.
39. Bailey, C.G., et al., *Open-circuit voltage improvement of InAs/GaAs quantum-dot solar cells using reduced InAs coverage*. IEEE Journal of Photovoltaics, 2012. **2**(3): p. 269.
40. Raviswaran, A., et al., *Evolution of coherent islands during strained-layer Volmer-Weber growth of Si on Ge (111)*. Physical Review B, 2001. **63**(12): p. 125314.
41. Benyoucef, M. and J. Reithmaier, *Direct growth of III-V quantum dots on silicon substrates: structural and optical properties*. Semiconductor Science and Technology, 2013. **28**(9): p. 094004.
42. Ren, L., H. Li, and L. Ma, *The Selective Growth of Silicon Nanowires and Their Optical Activation*. 2011.
43. Trentler, T.J., et al., *Solution-Liquid-Solid Growth of Crystalline III-V Semiconductors: An Analogy to Vapor-Liquid-Solid Growth*. Science, 1995. **270**(5243): p. 1791.
44. Westwater, J., et al., *Growth of silicon nanowires via gold/silane vapor-liquid-solid reaction*. Journal of Vacuum Science & Technology B, 1997. **15**(3): p. 554.

45. Wu, Y. and P. Yang, *Direct observation of vapor-liquid-solid nanowire growth*. Journal of the American Chemical Society, 2001. **123**(13): p. 3165.
46. Vogel, R., P. Hoyer, and H. Weller, *Quantum-Sized PbS, CdS, Ag₂S, Sb₂S₃ and Bi₂S₃ Particles as Sensitizers for Various Nanoporous Wide-Bandgap Semiconductors*. Journal of Physical Chemistry, 1994. **98**(12): p. 3183.
47. Kamat, P.V., *Quantum dot solar cells. Semiconductor nanocrystals as light harvesters*. The Journal of Physical Chemistry C, 2008. **112**(48): p. 18737.
48. Faraday, M., *The Bakerian lecture: experimental relations of gold (and other metals) to light*. Philosophical Transactions of the Royal Society of London, 1857: p. 145.
49. Peng, X.G., J. Wickham, and A.P. Alivisatos, *Kinetics of II-VI and III-V colloidal semiconductor nanocrystal growth: "Focusing" of size distributions*. Journal of the American Chemical Society, 1998. **120**(21): p. 5343.
50. Qu, L.H., W.W. Yu, and X.P. Peng, *In situ observation of the nucleation and growth of CdSe nanocrystals*. Nano Letters, 2004. **4**(3): p. 465.
51. Xie, R., Z. Li, and X. Peng, *Nucleation Kinetics vs Chemical Kinetics in the Initial Formation of Semiconductor Nanocrystals*. Journal of the American Chemical Society, 2009. **131**(42): p. 15457.
52. Murray, C.B., D.J. Norris, and M.G. Bawendi, *Synthesis and Characterization of Nearly Monodisperse CdE (E = S, Se, Te) Semiconductor Nanocrystallites*. Journal of the American Chemical Society, 1993. **115**(19): p. 8706.
53. Murray, C.B., C. Kagan, and M. Bawendi, *Synthesis and characterization of monodisperse nanocrystals and close-packed nanocrystal assemblies*. Annual Review of Materials Science, 2000. **30**(1): p. 545.
54. Jin, T., et al., *Amphiphilic p-sulfonatocalix[4]arene-coated CdSe/ZnS quantum dots for the optical detection of the neurotransmitter acetylcholine*. Chemical Communications, 2005(34): p. 4300.
55. Murray, C.B., et al., *Colloidal synthesis of nanocrystals and nanocrystal superlattices*. IBM Journal of Research and Development, 2001. **45**(1): p. 47.

56. Hines, M.A. and G.D. Scholes, *Colloidal PbS nanocrystals with size-tunable near-infrared emission: Observation of post-synthesis self-narrowing of the particle size distribution*. *Advanced Materials*, 2003. **15**(21): p. 1844.
57. Medintz, I.L., et al., *Quantum dot bioconjugates for imaging, labelling and sensing*. *Nature Materials*, 2005. **4**(6): p. 435.
58. Emin, S., et al., *Colloidal quantum dot solar cells*. *Solar Energy*, 2011. **85**(6): p. 1264.
59. Huynh, W.U., J.J. Dittmer, and A.P. Alivisatos, *Hybrid nanorod-polymer solar cells*. *Science*, 2002. **295**(5564): p. 2425.
60. Ren, S., et al., *Inorganic-organic hybrid solar cell: bridging quantum dots to conjugated polymer nanowires*. *Nano Letters*, 2011. **11**(9): p. 3998.
61. Liu, J., et al., *Employing end-functional polythiophene to control the morphology of nanocrystal-polymer composites in hybrid solar cells*. *Journal of the American Chemical Society*, 2004. **126**(21): p. 6550.
62. McDonald, S.A., et al., *Solution-processed PbS quantum dot infrared photodetectors and photovoltaics*. *Nature Materials*, 2005. **4**(2): p. 138.
63. Ryan, J.W., et al., *Nongeminate Recombination Dynamics-Device Voltage Relationship in Hybrid PbS Quantum Dot/C60 Solar Cells*. *The Journal of Physical Chemistry C*, 2013. **117**(34): p. 17470.
64. Zhou, Y., et al., *Efficiency enhancement for bulk-heterojunction hybrid solar cells based on acid treated CdSe quantum dots and low bandgap polymer PCPDTBT*. *Solar Energy Materials and Solar Cells*, 2011. **95**(4): p. 1232.
65. Li, Y., et al., *An Electrochemical Avenue to Green- Luminescent Graphene Quantum Dots as Potential Electron- Acceptors for Photovoltaics*. *Advanced Materials*, 2011. **23**(6): p. 776.
66. Guo, C.X., et al., *Layered graphene/quantum dots for photovoltaic devices*. *Angewandte Chemie, International Edition*, 2010. **49**(17): p. 3014.
67. Landi, B., et al., *CdSe quantum dot-single wall carbon nanotube complexes for polymeric solar cells*. *Solar Energy Materials and Solar Cells*, 2005. **87**(1): p. 733.

68. Lee, Y.-L. and C.-H. Chang, *Efficient polysulfide electrolyte for CdS quantum dot-sensitized solar cells*. Journal of Power Sources, 2008. **185**(1): p. 584.
69. Lee, H.J., et al., *Regenerative PbS and CdS quantum dot sensitized solar cells with a cobalt complex as hole mediator*. Langmuir, 2009. **25**(13): p. 7602.
70. Lee, H., et al., *PbS and CdS Quantum Dot- Sensitized Solid- State Solar Cells: "Old Concepts, New Results"*. Advanced Functional Materials, 2009. **19**(17): p. 2735.
71. Mora-Seró, I., et al., *Recombination in quantum dot sensitized solar cells*. Accounts of Chemical Research, 2009. **42**(11): p. 1848.
72. Tenne, R. and G. Hodes, *Improved efficiency of CdSe photoanodes by photoelectrochemical etching*. Applied Physics Letters, 2008. **37**(4): p. 428.
73. Shen, Q., et al., *Effect of ZnS coating on the photovoltaic properties of CdSe quantum dot-sensitized solar cells*. Journal of Applied Physics, 2008. **103**(8): p. 084304.
74. Radich, J.G., R. Dwyer, and P.V. Kamat, *Cu₂S Reduced Graphene Oxide Composite for High-Efficiency Quantum Dot Solar Cells. Overcoming the Redox Limitations of S²⁻/Sn²⁻ at the Counter Electrode*. The Journal of Physical Chemistry Letters, 2011. **2**(19): p. 2453.
75. Lee, Y.-L., B.-M. Huang, and H.-T. Chien, *Highly efficient CdSe-sensitized TiO₂ photoelectrode for quantum-dot-sensitized solar cell applications*. Chemistry of Materials, 2008. **20**(22): p. 6903.
76. González-Pedro, V., et al., *Modeling high-efficiency quantum dot sensitized solar cells*. ACS Nano, 2010. **4**(10): p. 5783.
77. Diguna, L.J., et al., *High efficiency of CdSe quantum-dot-sensitized TiO₂ inverse opal solar cells*. Applied Physics Letters, 2007. **91**(2): p. 023116.
78. Rühle, S., M. Shalom, and A. Zaban, *Quantum- Dot- Sensitized Solar Cells*. ChemPhysChem, 2010. **11**(11): p. 2290.
79. Lee, J.-W., et al., *Quantum-dot-sensitized solar cell with unprecedentedly high photocurrent*. Scientific Reports, 2013. **3**.

80. Strasfeld, D.B., et al., *Imaging Schottky barriers and ohmic contacts in PbS quantum dot devices*. Nano Letters, 2012. **12**(2): p. 569.
81. Piliago, C., et al., *5.2% efficient PbS nanocrystal Schottky solar cells*. Energy & Environmental Science, 2013. **6**(10): p. 3054.
82. Pattantyus-Abraham, A.G., et al., *Depleted-heterojunction colloidal quantum dot solar cells*. ACS Nano, 2010. **4**(6): p. 3374.
83. Liu, H., et al., *Systematic optimization of quantum junction colloidal quantum dot solar cells*. Applied Physics Letters, 2012. **101**(15): p. 151112.
84. Liu, H., et al., *Electron acceptor materials engineering in colloidal quantum dot solar cells*. Advanced Materials, 2011. **23**(33): p. 3832.
85. Tang, J., et al., *Colloidal-quantum-dot photovoltaics using atomic-ligand passivation*. Nature Materials, 2011. **10**(10): p. 765.
86. Ip, A.H., et al., *Hybrid passivated colloidal quantum dot solids*. Nature Nanotechnology, 2012. **7**(9): p. 577.
87. Ning, Z., et al., *Graded doping for enhanced colloidal quantum dot photovoltaics*. Advanced Materials, 2013. **25**(12): p. 1719.
88. Tang, J., et al., *Quantum junction solar cells*. Nano Letters, 2012. **12**(9): p. 4889.
89. Kramer, I.J., et al., *Solar cells using quantum funnels*. Nano Letters, 2011. **11**(9): p. 3701.
90. Wang, X., et al., *Tandem colloidal quantum dot solar cells employing a graded recombination layer*. Nature Photonics, 2011. **5**(8): p. 480.
91. *Advanced Inorganic Chemistry, 6th ed.* 2007: Wiley India Pvt. Limited.
92. Mazumder, S., et al., *Review: biofunctionalized quantum dots in biology and medicine*. Journal of Nanomaterials, 2009. **2009**: p. 38.
93. Algar, W.R., A.J. Tavares, and U.J. Krull, *Beyond labels: A review of the application of quantum dots as integrated components of assays, bioprobes,*

and biosensors utilizing optical transduction. Analytica Chimica Acta, 2010. **673**(1): p. 1.

94. Konstantatos, G. and E.H. Sargent, *Colloidal Quantum Dot Optoelectronics and Photovoltaics*. 2013: Cambridge University Press.
95. Moody, I.S., A.R. Stonas, and M.C. Lonergan, *PbS nanocrystals functionalized with a short-chain, ionic, dithiol ligand*. *The Journal of Physical Chemistry C*, 2008. **112**(49): p. 19383.
96. Luther, J.M., et al., *Structural, optical and electrical properties of self-assembled films of PbSe nanocrystals treated with 1,2-ethanedithiol*. *ACS Nano*, 2008. **2**(2): p. 271.
97. Barkhouse, D.A.R., et al., *Thiols passivate recombination centers in colloidal quantum dots leading to enhanced photovoltaic device efficiency*. *ACS Nano*, 2008. **2**(11): p. 2356.
98. Szendrei, K., et al., *PbS nanocrystal solar cells with high efficiency and fill factor*. *Applied Physics Letters*, 2010. **97**(20): p. 203501.
99. Xu, F., et al., *Interconnected TiO₂ Nanowire Networks for PbS Quantum Dot Solar Cell Applications*. *Journal of Nanotechnology*, 2012. **2012**.709031
100. Padilla, D., et al., *Thermal Properties of TiO₂/PbS Nanoparticle Solar Cells*. *Nanomaterials & Nanotechnology*, 2012. **2**(2).18
101. Klem, E.J., et al., *Impact of dithiol treatment and air annealing on the conductivity, mobility, and hole density in PbS colloidal quantum dot solids*. *Applied Physics Letters*, 2008. **92**(21): p. 212105.
102. Inerbaev, T.M., et al., *Quantum chemistry of quantum dots: Effects of ligands and oxidation*. *Journal of Chemical Physics*, 2009. **131**(4).
103. Voznyy, O., et al., *A charge-orbital balance picture of doping in colloidal quantum dot solids*. *ACS Nano*, 2012. **6**(9): p. 8448.
104. Jeong, K.S., et al., *Enhanced Mobility-Lifetime Products in PbS Colloidal Quantum Dot Photovoltaics*. *ACS Nano*, 2012. **6**(1): p. 89.

105. Tang, J., et al., *Quantum Dot Photovoltaics in the Extreme Quantum Confinement Regime: The Surface-Chemical Origins of Exceptional Air- and Light-Stability*. ACS Nano, 2010. **4**(2): p. 869.
106. Koleilat, G.I., et al., *Efficient, stable infrared photovoltaics based on solution-cast colloidal quantum dots*. ACS Nano, 2008. **2**(5): p. 833.
107. Kovalenko, M.V., et al., *Expanding the chemical versatility of colloidal nanocrystals capped with molecular metal chalcogenide ligands*. Journal of the American Chemical Society, 2010. **132**(29): p. 10085.
108. Kovalenko, M.V., M. Scheele, and D.V. Talapin, *Colloidal nanocrystals with molecular metal chalcogenide surface ligands*. Science, 2009. **324**(5933): p. 1417.
109. Nag, A., et al., *Metal-free Inorganic Ligands for Colloidal Nanocrystals: S^{2-} , HS^- , Se^{2-} , HSe^- , Te^{2-} , HTe^- , TeS_3^{2-} , OH^- , and NH_2^- as Surface Ligands*. Journal of the American Chemical Society, 2011. **133**(27): p. 10612.
110. Ning, Z., et al., *All- Inorganic Colloidal Quantum Dot Photovoltaics Employing Solution- Phase Halide Passivation*. Advanced Materials, 2012. **24**(47): p. 6295.
111. Zhitomirsky, D., et al., *N- Type Colloidal- Quantum-Dot Solids for Photovoltaics*. Advanced Materials, 2012. **24**(46): p. 6181.
112. Thon, S.M., et al., *Role of Bond Adaptability in the Passivation of Colloidal Quantum Dot Solids*. ACS Nano, 2013. **7**(9): p. 7680.
113. Bae, W.K., et al., *Highly effective surface passivation of PbSe quantum dots through reaction with molecular chlorine*. Journal of the American Chemical Society, 2012. **134**(49): p. 20160.
114. Zanella, M., et al., *Atomic Ligand Passivation of Colloidal Nanocrystal Films via their Reaction with Propyltrichlorosilane*. Chemistry of Materials, 2013. **25**(8): p. 1423.
115. Zhang, H., et al., *Surfactant ligand removal and rational fabrication of inorganically connected quantum dots*. Nano Letters, 2011. **11**(12): p. 5356.

116. Mora-Sero, I., et al., *Selective contacts drive charge extraction in quantum dot solids via asymmetry in carrier transfer kinetics*. Nature Communications, 2013. **4**.
117. Maraghechi, P., et al., *The donor–supply electrode enhances performance in colloidal quantum dot solar cells*. ACS Nano, 2013. **7**(7): p. 6111.
118. Ehrler, B., et al., *Preventing interfacial recombination in colloidal quantum dot solar cells by doping the metal oxide*. ACS Nano, 2013. **7**(5): p. 4210.
119. Willis, S.M., et al., *The transitional heterojunction behavior of PbS/ZnO colloidal quantum dot solar cells*. Nano Letters, 2012. **12**(3): p. 1522.
120. Wang, X., et al., *Enhanced Open-Circuit Voltage in Visible Quantum Dot Photovoltaics by Engineering of Carrier-Collecting Electrodes*. ACS Applied Materials & Interfaces, 2011. **3**(10): p. 3792.
121. Jean, J., et al., *ZnO nanowire arrays for enhanced photocurrent in PbS quantum dot solar cells*. Advanced Materials, 2013. **25**(20): p. 2790.
122. Debnath, R., et al., *Ambient-Processed Colloidal Quantum Dot Solar Cells via Individual Pre-Encapsulation of Nanoparticles*. Journal of the American Chemical Society, 2010. **132**(17): p. 5952.
123. Tang, J., et al., *Schottky quantum dot solar cells stable in air under solar illumination*. Advanced Materials, 2010. **22**(12): p. 1398.
124. Johnston, K.W., et al., *Schottky-quantum dot photovoltaics for efficient infrared power conversion*. Applied Physics Letters, 2008. **92**(15): p. 151115.
125. Etgar, L., et al., *Light energy conversion by mesoscopic PbS quantum dots/TiO₂ heterojunction solar cells*. ACS Nano, 2012. **6**(4): p. 3092.
126. Brown, P.R., et al., *Improved current extraction from ZnO/PbS quantum dot heterojunction photovoltaics using a MoO₃ interfacial layer*. Nano Letters, 2011. **11**(7): p. 2955.
127. Gao, J., et al., *n-type transition metal oxide as a hole extraction layer in PbS quantum dot solar cells*. Nano Letters, 2011. **11**(8): p. 3263.

128. Meyer, J. and A. Kahn, *Electronic structure of molybdenum-oxide films and associated charge injection mechanisms in organic devices*. Journal of Photonics for Energy, 2011. **1**.011109
129. Gao, J.B., et al., *Quantum Dot Size Dependent J-V Characteristics in Heterojunction ZnO/PbS Quantum Dot Solar Cells*. Nano Letters, 2011. **11**(3): p. 1002.
130. Bakulin, A.A., et al., *Charge Trapping Dynamics in PbS Colloidal Quantum Dot Photovoltaic Devices*. ACS Nano, 2013. **7**(10): p. 8771.
131. Zhitomirsky, D., et al., *Measuring charge carrier diffusion in coupled colloidal quantum dot solids*. ACS Nano, 2013. **7**(6): p. 5282.
132. Guyot-Sionnest, P., B. Wehrenberg, and D. Yu, *Intraband relaxation in CdSe nanocrystals and the strong influence of the surface ligands*. The Journal of Chemical Physics, 2005. **123**(7): p. 074709.

CHAPTER 3 – EXPERIMENTAL METHODOLOGY

3.1 – Introduction

This chapter describes the steps leading to the production of a heterojunction PbS colloidal quantum dot (CQD) photovoltaic device, including the measurement techniques used to characterize the synthesized materials (ultraviolet-visible-near-infrared (UV-Vis-NIR) photospectroscopy, fluorescence spectroscopy, X-ray photoelectron spectroscopy, X-ray diffraction, infrared spectroscopy, energy dispersive X-ray spectroscopy, transmission electron microscopy) and the device performance (current-voltage response under solar simulator, incident photon-to-charge carrier efficiency, transient charge extraction techniques). In addition, details on quantum dot preparation and device assembly are provided.

3.2 – Material Characterization

3.2.1 – UV-Vis-NIR absorption spectroscopy

A SHIMADZU UV-1800 with a 0.5 nm sampling interval was used in order to measure the proportion of light absorbed by a sample at a specific wavelength. A tungsten (W) filament coupled with a deuterium lamp generate a white light with a wide spectrum, which will pass through a diffraction grating monochromator (see Figure 3.1). The grating is a reflective substrate with densely packed parallel grooves (1200-1400 grooves/mm). By assuming that the surface has a sawtooth pattern (top

inset in Figure 3.1), the grating equation can be derived. The optical aperture is set at a fixed diffracted angle (D) and will only accept the wavelengths (λ) which interfere constructively after diffraction, as dictated by the grating equation:

$$a(\sin(I) + \sin(D)) = n\lambda \quad \text{Equation 3.1}$$

where a is the separation distance between the grooves ($\sim 0.8 \mu\text{m}$), I is the incidence angle, and n is an integer stating the diffraction order. To prevent photons with a wavelength $n\lambda$ from also being included, a band-pass filter normally precedes the monochromator to narrow the spectrum in advance.

The beam is then split in two between the sample and a reference before reaching a photodiode (see Figure 3.1). First, there is a baseline measurement of the absorption of any obstacle in the light beam path that would add to the sample's absorption. In the case of PbS CQDs dispersed in toluene, a cuvette filled with toluene only will be run as the baseline. If the material is cast onto a substrate, this substrate alone needs to be measured as the baseline.

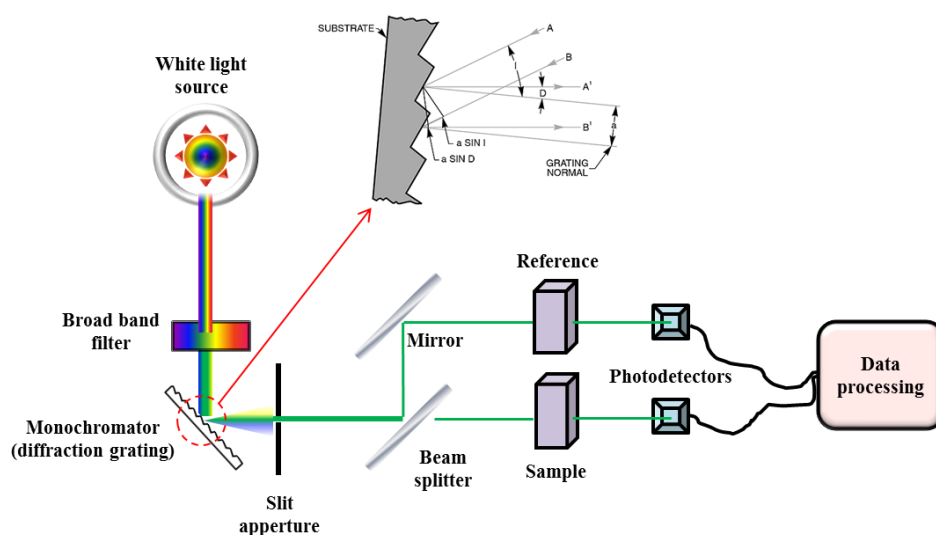


Figure 3.1 – Typical absorption spectroscopy set-up. The inset shows details of the geometry of the measurement.

Following the Beer-Lambert law, the transmitted light intensity I_T :

$$I_T = I_0 e^{-A} = I_0 e^{-\alpha d} \quad (3.2)$$

where I_0 , A , α , and d are the incident light intensity, the absorbance, the absorption coefficient, and the thickness of the sample. Absorption spectroscopy is especially appropriate for characterizing photoactive materials. For PbS CQDs, it is a way to determine the optical band gap (or first exciton energy) and calculate the size distribution of the sample (Equation 2.21).

In this work, UV-Vis-NIR spectra were acquired with a SHIMADZU UV-1800 with a 0.5 nm sampling interval.

3.2.2 – Photoluminescence spectroscopy

Photoluminescence (PL) is the emission of a photon through radiative relaxation of an electron which was excited to some upper energy level (e.g. after absorbing a higher energy photon). When the emitted radiation originates from recombination from a singlet state (typically ~ns scale), it is called fluorescence.

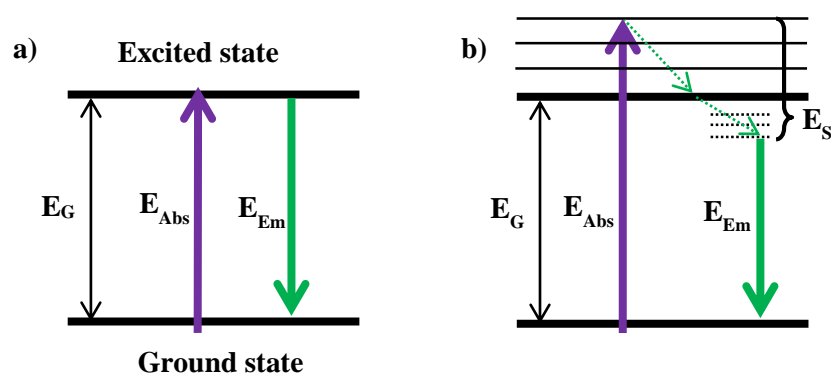


Figure 3.2 – Representation of PL process with negligible (a) and significant (b) internal relaxation. E_G , E_{Abs} , E_{em} , and E_S are the band gap, the absorbed and emitted photon energy, and the Stoke shift, respectively.

If the excited electron undergoes internal relaxation to a triplet state, however, the transitions to the ground state are “forbidden” (as dictated by quantum mechanics), and the relaxation can stretch to longer time scales.

In order for the detector to only receive fluorescence emission (diffusive), care must be taken to keep it away from the transmitted and reflected beam path. As both the source and the detector have their own monochromators, one can choose to keep one steady while scanning the other. The relation between the absorption and emission energies can give fundamental information related to the interactions of states in materials and molecules. For example, the Stokes shift is the difference between the absorption and emission peaks and reflects the losses due to non-radiative state transitions (Figure 3.2).

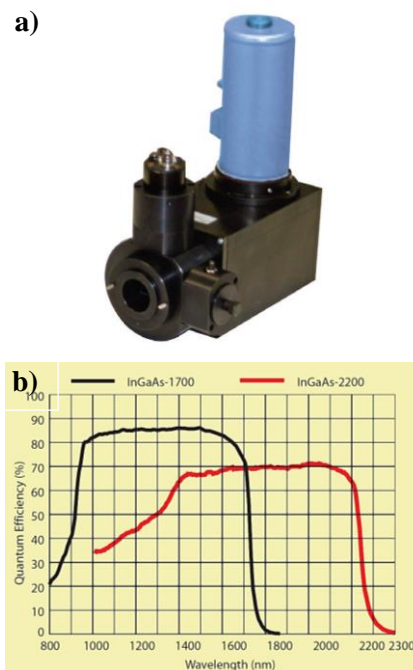


Figure 3.3 – (a) Cryogenically cooled InGaAs-1700 detector from HORIBA Jobin Yvon and (b) its spectral response.

In this project, PL spectroscopy is carried out through a custom-built system from Horiba - Jobin Yvon using an InGaAs single channel detector (Figure 3.3) which offers improved sensitivity and detection range once cryogenically cooled with liquid nitrogen. The excitation wavelength is parked at 550 nm, and the entrance and exit slits were both set at a 2 nm band pass.

3.2.3 – X-ray photoelectron spectroscopy (XPS)

This technique probes the energy levels of valence electrons at the surface of a sample. A non-monochromatic X-ray beam is produced by bombarding an aluminium anode with high energy electrons. The photons are then focused on a quartz crystal which will re-emit monochromatic X-rays by fluorescence ($h\nu \approx 1486.7$ eV), narrowing both the spectral and the spatial distribution. The photons excite electrons in valence core levels so they can exit the material surface with excess energy (see Figure 3.4). As this kinetic energy is measured by the spectrometer's detector, one can calculate the binding energy according to:

$$BE = h\nu - (KE + \Phi) = h\nu - (KE' + \Phi') \quad \text{Equation 3.4}$$

where $h\nu$, BE , KE , KE' , Φ , and Φ' are the photon energy, the binding energy, the kinetic energy seen from the sample and from the spectrometer, and the sample's and the spectrometer's work function, respectively.

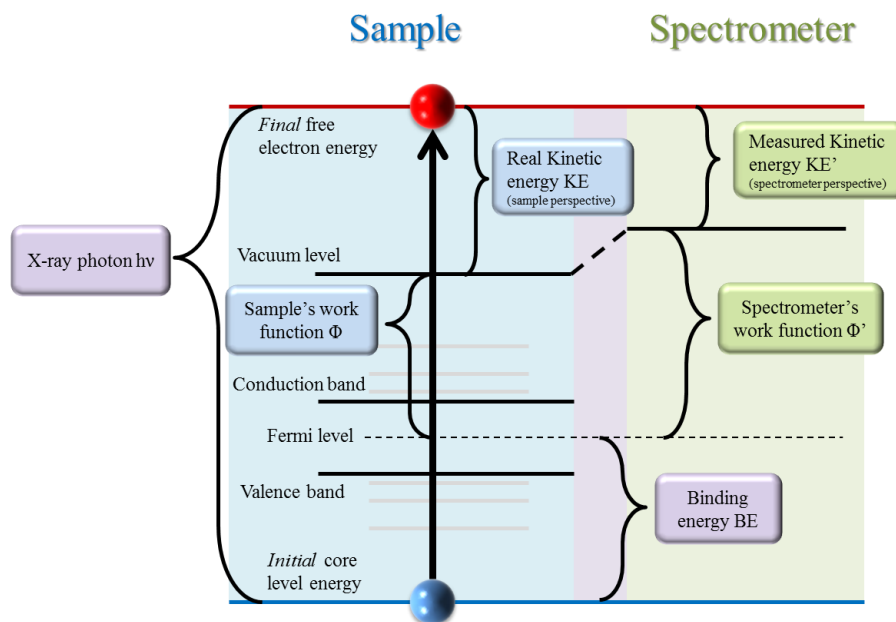


Figure 3.4 – Relation between the photon energy, the kinetic energy, the work function, and the binding energy for both sample and spectrometer in XPS measurement.

Electrostatic/magnetic lenses collect electrons with specific kinetic energy by setting the appropriate voltage, and a combination of apertures and slits reduces the noise and the bandwidth of the signal. The resolving power of the analyser ($E/\delta E$) determines how the sensitivity and resolution can be set with minimum conflict. The *pass energy* corresponds to the deceleration imposed on the incoming electrons. The XPS instrument used in this project is equipped with a hemispherical energy analyser to improve resolution. The whole set-up requires high to ultra-high vacuum levels ($\sim 10^{-9}$ mbar):

- to desorb water contamination from the surface of the sample;
- to prevent electrons from colliding with any obstacle on their way to the counting detector, positioned approximately a meter away from the target.

A survey scan gives an overview of the energy peaks present on the spectrum and leads to more accurate mapping of the surface composition (Figure 3.5).

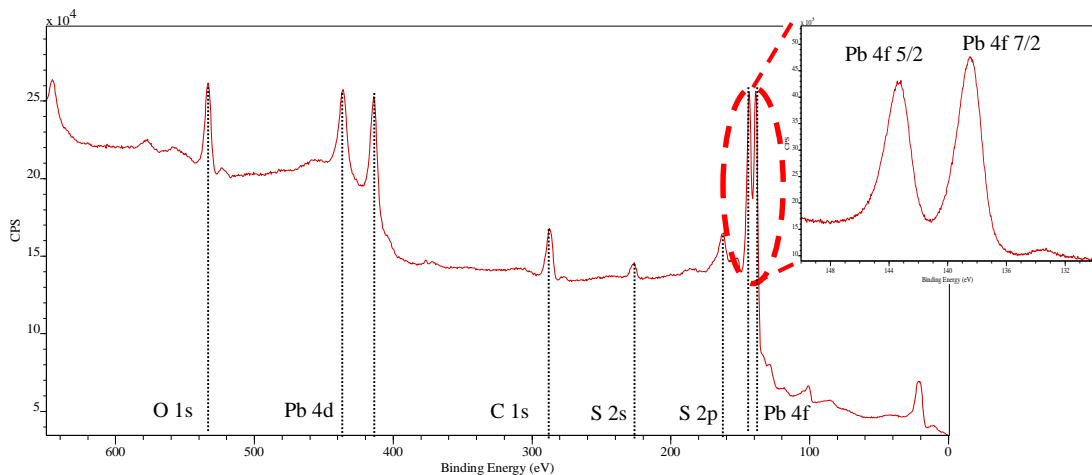


Figure 3.5 – Survey spectrum of a PbS CQD film. Inset shows a high resolution scan centered on the Pb 4f peaks.

High resolution scans (e.g. Figure 3.5 inset) provide detailed information on how atoms are bound together by measuring energy shifts and bandwidth alterations. By

deconvoluting peaks, one can identify the proportions of different species of the same atom (e.g., oxidation states, covalencies with other atoms).

In this thesis study, XPS was conducted using a SPECS PHOIBOS 100 Analyser installed in a high-vacuum chamber with base pressure below 10^{-8} mbar. X-ray excitation through Al K α radiation ($h\nu = 1486.61$ eV) was operated at 12 kV (120 W). The XPS binding energy high resolution spectra were recorded with a 20 eV pass energy in the fixed analyser transmission mode. The calibration was performed by fitting the C 1s and Cu 2p peaks from a pure copper sample. Analysis of the XPS data was carried out using the commercial CasaXPS2.3.15 software package. The signal was fitted using a Voigt Gauss-Lorentz (GL) line shape, GL(30), and the background type was set to “Shirley”. For multicomponent fittings, the full-width half-maximum (FWHM) of each component was set to be equal to each other, to reflect that captured electrons were affected by the same phonon interactions and rearrangement environment. A general survey scan was always performed in order to confirm that no silicon peak appears, ensuring that the emitted photoelectrons are only coming from the CQD film.

3.2.4 – Infrared (IR) spectroscopy

This technique provides a signature for specific types of bonds that absorb IR photons and dissipate the energy through vibrations which characterize the molecular structure. Organic compounds (containing C, O, H, N) tend to have numerous sharp peak signatures specific to their molecular configuration (e.g. aromatic ring vs. hydrocarbon chain), making them the ideal target for this kind of measurement. In this work, IR spectra were acquired with a SHIMADZU Prestige-21.

3.2.5 – Stylus profilometer

A Veeco profilometer (Dektak 150) was used to determine film thicknesses. In this system, a stylus is used to detect the topography at the surface. It is connected through a pivot to a

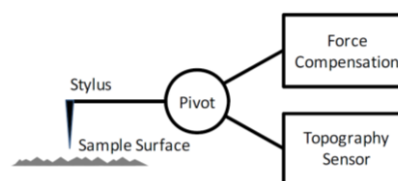


Figure 3.6 – Stylus profiler sensor schematic.

topography sensor which will track the signal and a force compensation mechanism which applies a constant force at the surface (see Figure 3.6).

3.2.6 – Transmission electron microscopy (TEM)

To observe the impact of ligand exchange on interparticle spacing, TEM imaging was performed using a JML-2011F from JEOL Ltd (Figure 3.7(a)). The samples were prepared by dipping TEM grids in a 0.5 mg/ml PbS CQDs solution in n-octane. To exchange the ligand, the grid was then dipped in a 5% v/v 3-mercaptopropionic acid in methanol and then rinsed with methanol and n-octane (Figure 3.7(b)).

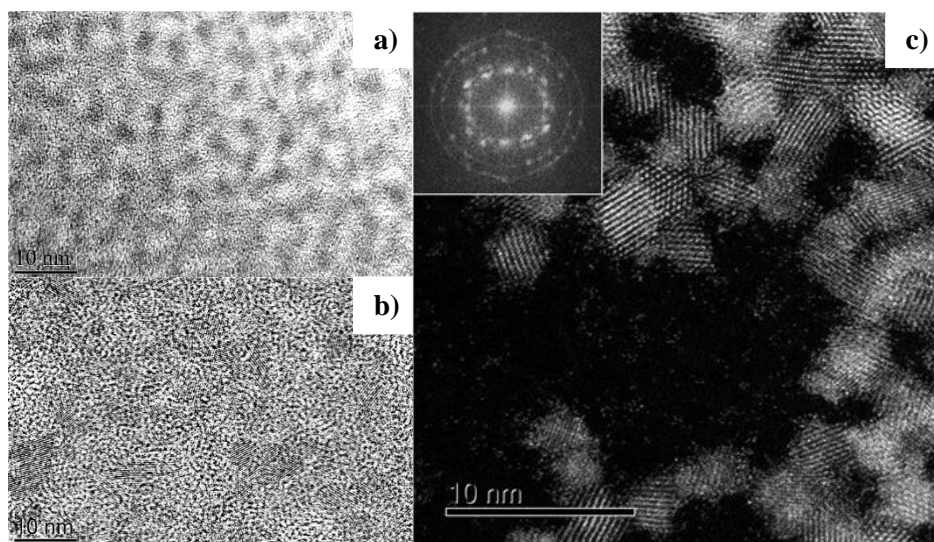


Figure 3.7 – TEM imaging of PbS CQDs before (a) and after (b) exchanging oleic acid ligands for 3-mercaptopropionic acid. Images taken by Ziqi Sun.

The sample were imaged again using a JEOL-ARM-200F (Figure 3.7(c)). Four planes could be identified with d-spacing of 3.47 Å, 2.93 Å, 2.12 Å and 1.84 Å corresponding to the 111, 002, 220 and 311 planes, respectively.¹

3.3 – Device characterization

3.3.1 – Solar simulator

The standard equipment used in this work was a certified class AAA (spectral-temporal-spatial) solar simulator and was purchased from Peccell Technologies Inc. (see Figure 3.8). The power supply (white dashed line) contains a switching regulator to keep current fluctuation below 4%. The sample stage PEC-T10 (blue dashed line) allows keeps the device temperature constant throughout the measurement.

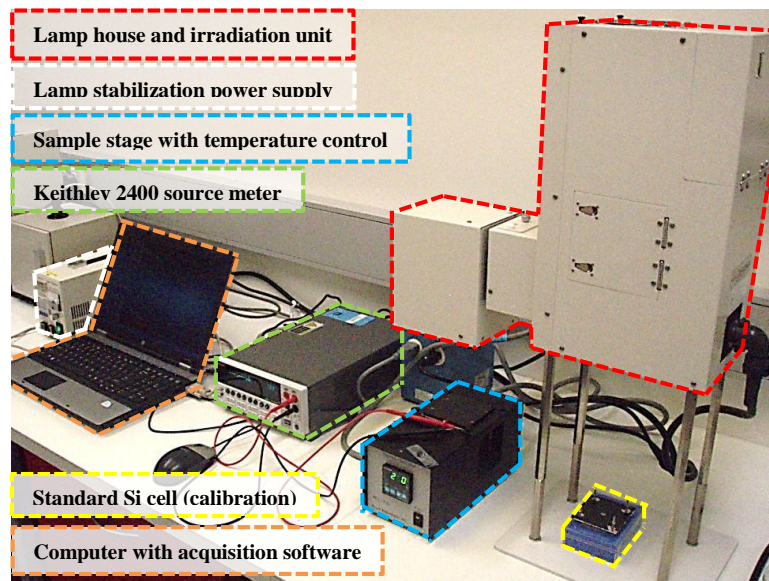


Figure 3.8 – Photograph of the solar simulator set-up.

The Keithley 2400 sourcemeter (green dashed line) is controlled by a Pecell I-V curve analyser Ver. 2.1 software on the computer (orange dashed line) and measures the current response under an applied bias. The silicon standard cell (yellow dashed line) is a stable device which provides a reference to calibrate the simulator. The main lamp unit, a PEC-L12 (red dashed line), contains:

- a xenon arc bulb generating a white light spectrum;
- the optics (collimator lens, integrator lens, and mirrors) responsible for delivering a spatially uniform output (less than 2% variation inside a 50 mm x 50 mm area);
- the air mass filter (AM1.5G) responsible for reducing strong peaks from the xenon arc lamp spectrum in order to give a closer replica of the solar spectrum (see Figure 3.9).

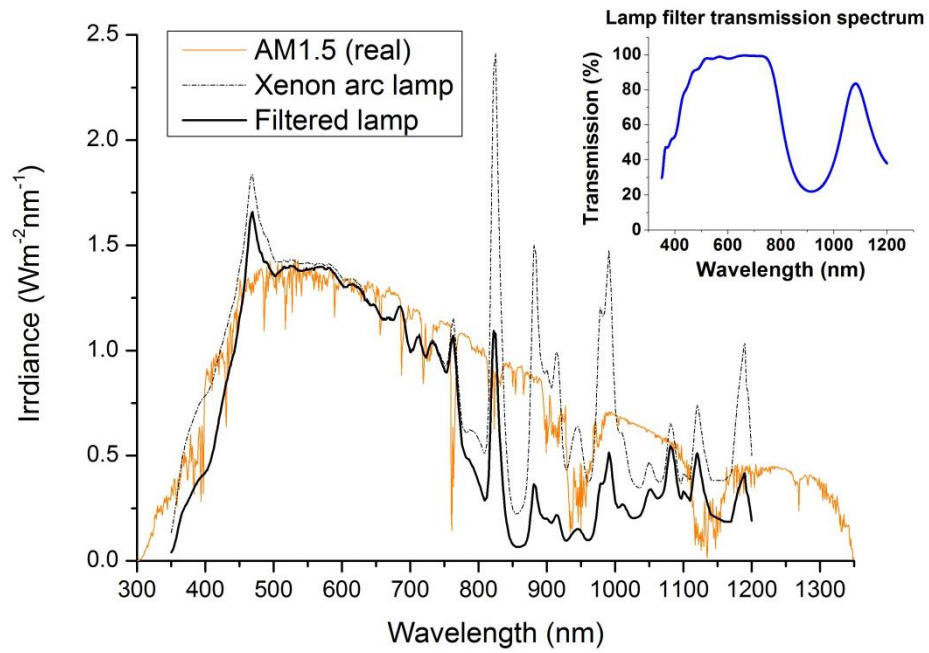


Figure 3.9 – Comparison between the real AM1.5 spectrum and the spectrum from the xenon lamp (with and without filter). The inset shows the AM1.5 filter transmission spectrum.

We can observe significant mismatches, however, between 750 and 1050 nm. The apparatus was acquired for dye-sensitized solar cells (DSCs) performance measurement purposes. For such devices, this mismatch typically will not significantly affect the measurement, as most dyes don't absorb above 750 nm. 3-4 nm PbS quantum dots, on the other hand, absorb strongly in the 900-1050 nm region, and devices using CQDs show appreciable external quantum efficiencies out to 1200 nm (Figure 3.10). It was calculated that this mismatch accounts for $\sim 7\%$ ($\pm 1.2\%$) overestimate of the input power, P_{in} .

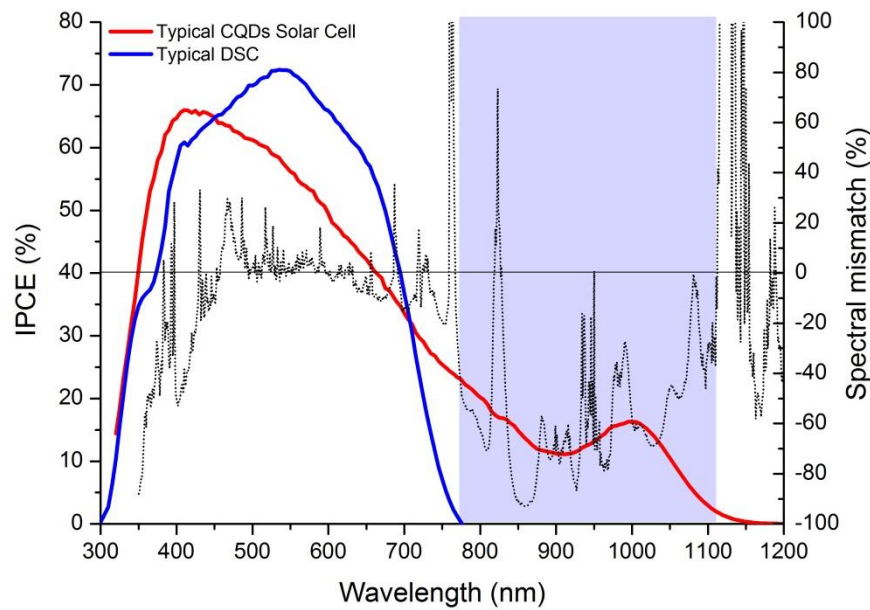


Figure 3.10 – IPCE for a typical PbS CQD solar cell (red) and dye-sensitized solar cell (blue, data reported with permission of Jianjian Lin). The AM1.5 spectral mismatch is represented by the dotted curve, and the purple rectangle frames the region of strong mismatch.

3.3.2 – Current-voltage response under cold-white LED illumination

After assembly, the devices are brought in an argon filled glovebox. Before being sealed, the devices are tested qualitatively using a home-made sample holder mounted with a cold-white LED (see Figure 3.11).

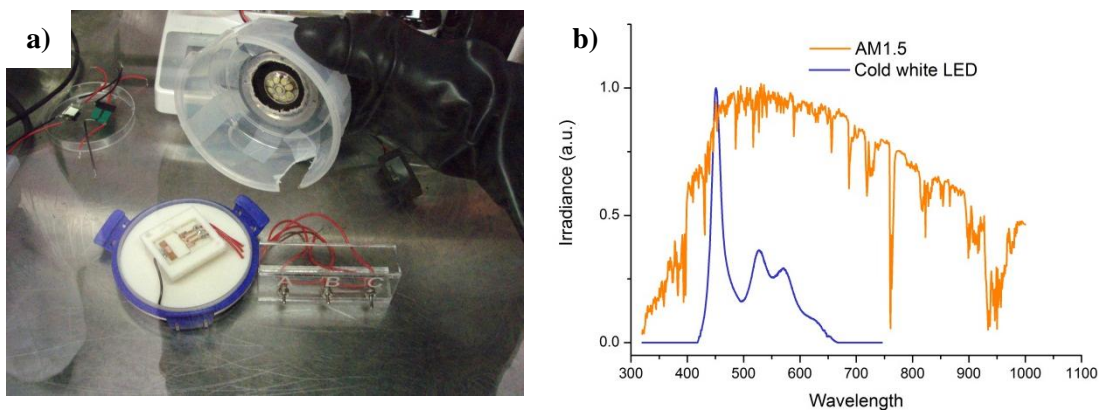


Figure 3.11 – (a) Home-made setup for cell characterization before sealing (in the glove box). (b) Comparison between the spectral irradiance of the LED and AM1.5.

The holder was connected to a eDAQ e-corder 410 to perform linear sweep voltammetry to provide the current response under dark and illumination conditions.

3.3.2 – Incident photon-to-charge carrier efficiency (IPCE)

The IPCE apparatus used in this thesis study measures the short circuit current I_λ from a solar cell illuminated by a monochromatic light. A microscope objective confines the spot onto a small area ($< 1 \text{ mm}^2$) to ensure that the photovoltaic device receives all the photons emitted. If the photon flux, φ_λ , is known for each wavelength (determined during calibration), the IPCE is calculated as:

$$IPCE|_\lambda(\%) = 100 \times \frac{\# \text{ electrons}}{\# \text{ photons}} = 100 \times \frac{I_\lambda / e}{\varphi_\lambda / hc/\lambda} = 100 \times \frac{1240}{\lambda} \times \frac{I_\lambda}{\varphi_\lambda} \quad (3.5)$$

From this equation, one can retrieve the value of the total short circuit current under AM1.5 illumination:

$$I_{sc} = \int^{AM1.5} \varphi_\lambda \times IPCE|_\lambda(\%) d\lambda \quad (3.6)$$

The conversion efficiency of this setup was proven to be altered by the time, however. Measurements at different rates show that the conversion becomes slowly underestimated as the measurement is systematically swept from low to high wavelengths. This result in a lower IPCE at slower rates (see Figure 3.12).

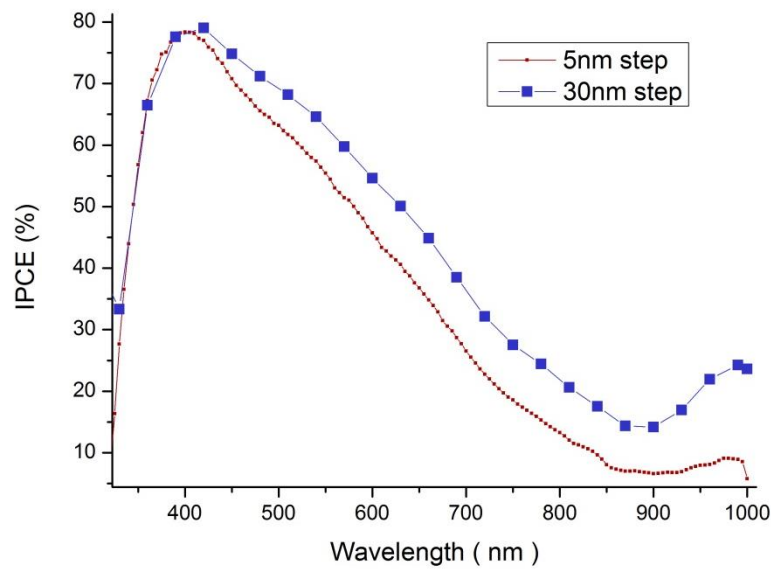


Figure 3.12 – IPCE spectra of a typical device at slow (red) and faster (blue) scan rates. Data reported with permission of Guanran Zhang.

This project used a home-built setup (Figure 3.13) involving a xenon lamp, a power supply and a monochromators supplied from Oriel®-Newport Instruments connected to the sample holder through an optical fibre fitted to a microscope lens to focus the beam. Data were processed using a home-built LabVIEW™ software connected to a Keithley 2400 source meter.

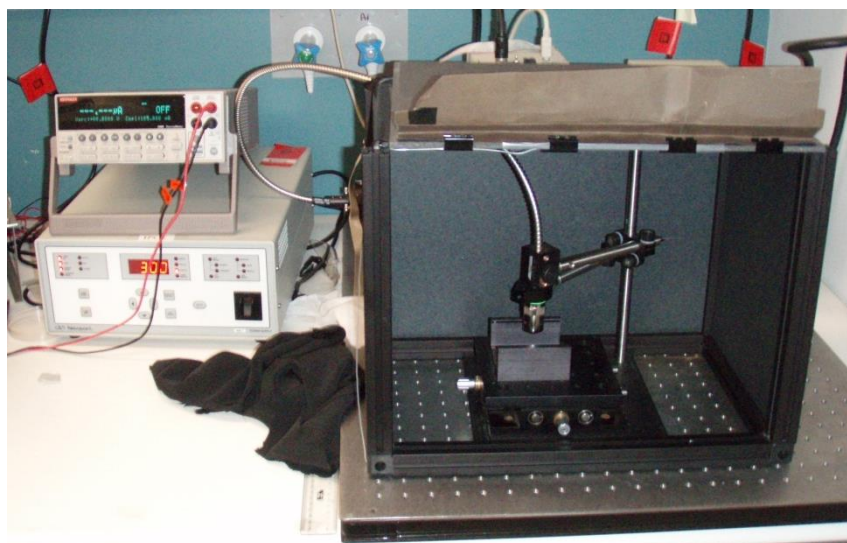


Figure 3.13 – In-house assembled IPCE setup.

3.3.3 – Charge extraction measurements

All these techniques were operated from the same set-up, using a Quanta Ray Lab Nd:YAG pulsed laser (6 ns, 532 nm) using an optical parametric oscillator MOPO-700. The signal output was monitored using a Digital Phosphor Oscilloscope (Tektronix, DPO4045).

3.3.3.1 – Photovoltage (V_{oc}) decay

The device is first held at open circuit voltage (V_{oc}) and is then illuminated by a laser pulse. The decay of photogenerated voltage is monitored.

3.3.3.2 – Transient photovoltage (TPV)

The device is held at open circuit under continuous illumination (adjustable intensity using neutral density filters). The laser pulse acts as a weak optical perturbation, and the photogenerated voltage is monitored in order to evaluate the charge carrier decay lifetime.

3.3.3.3 – Time-resolved charge extraction (TRCE)

In TRCE measurements, the solar cell is initially kept under open-circuit conditions. Charges are then photogenerated following illumination by a laser pulse at t_{pulse} . These charges recombine internally until the device is switched into short-

circuit conditions so the remaining charge carriers can be extracted under the built-in field (see Figure 3.14). The delay t_{del} between the laser pulse and the switch is adjusted with a nanosecond time-resolved switch (Asama Lab Solar Relay). The photocurrent was then integrated to ascertain the charge density at each delay time.

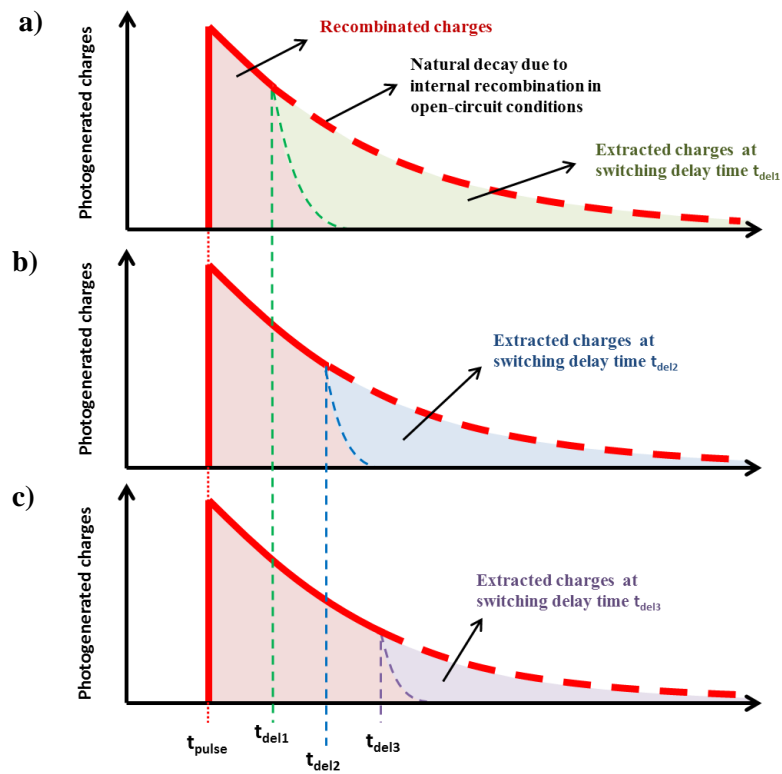


Figure 3.14 – Illustrated procedure to measure time-resolved charge extraction at different switching times.

3.3.3.4 – Time of flight (TOF)

The device is held under constant bias. The laser pulse generates charges, which are immediately extracted under the external field and monitored with an oscilloscope. In the present work, the measurement is performed on thin film ($ad \ll$

1) with a relatively high RC-circuit time constant ($\approx 130 \mu\text{s}$). Such a setup measures the extracted volume photogenerated charges in integral mode (Q-TOF).

3.3.3.5 – Photogenerated charge extraction by linearly increasing voltage (Photo-CELIV)

The device is first illuminated by the laser pulse in reflection mode.² The photogenerated charges are then extracted after an adjusted delay time controlled by a digital delay generator (Stanford Research DG535) by linearly increasing a voltage pulse applied by a Multifunction generator (Wave Factory, WF1974) as illustrated in Figure 3.15. The oscilloscope recording the transient current used a 12Ω input impedance. The resolution of the set-up is around 2 ns, and the calculated RC constant of the sample was ~ 150 ns.

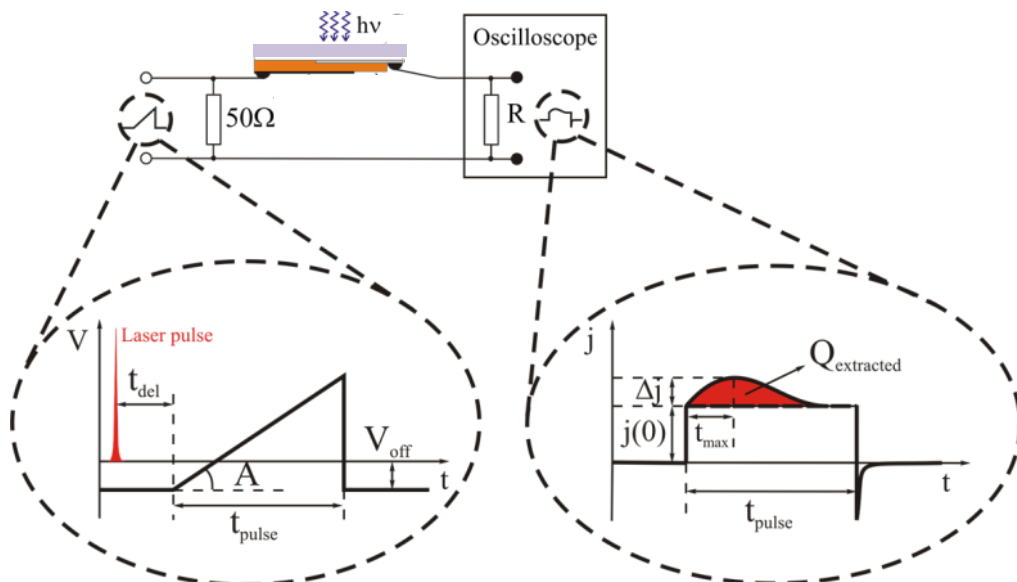


Figure 3.15 – Schematic representation of the photo-CELIV set-up.

3.4 – Quantum dot synthesis

3.4.1 – Synthesis

The quantum dots were synthesized according to a modified version of a previously reported procedure.^{3,4}

3.4.1.1 – Lead oleate precursor

In a 100 ml three-neck flask, 10 ml 1-octadecene (ODE, 90%, Sigma-Aldrich) is dried with bubbling nitrogen and heating at 120°C in an oil bath for 2 hours under continuous magnetic stirring. Once the flask is back to room temperature, 0.45 g lead oxide (PbO, 99.99%, Alfa Aesar) and 1.5 ml oleic acid (OA, 90%, Alfa Aesar, see Figure 3.16) are sequentially injected, leading to a light orange colour (Figure 3.17(a)). The flask is then sealed (with rubber septa) and purged three times by alternating 3 minutes of vacuum pumping (rotary pump) with an argon flush. The solution is stirred for 2 hours under vacuum at room temperature until it acquires a uniform milky white colour (Figure 3.17(b)). The hotplate is then turned on and set to 95°C (flask temperature) for an extra 2 hours until the solution becomes clear and transparent (Figure 3.17(c)).

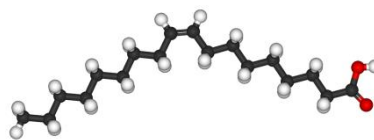


Figure 3.16 – Oleic acid molecule (black: carbon, red: oxygen, white: hydrogen).



Figure 3.17 – Photograph of the flask before degassing (a), before heating (b), and after heating (c).

3.4.1.1 – Sulfur precursor

In a separate 100 ml three-neck flask, 5 ml ODE is dried and degassed with bubbling nitrogen at 100°C for 12 hours under continuous magnetic stirring. Once the flask is back to room temperature, 210 μ l bis(trimethylsilyl) sulfide (TMS, 95%, Sigma-Aldrich, see Figure 3.18) is injected. The

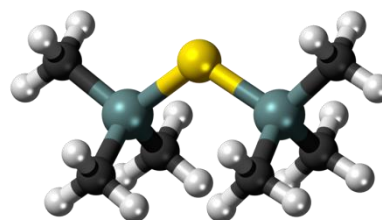


Figure 3.18 – Bis(trimethylsilyl) sulphide molecule (yellow: sulphur, dark cyan: silicon, black: carbon, white: hydrogen).

flask is then sealed and pruged using a freeze-pump-thaw method:

- the sealed flask is lowered and dipped into a liquid nitrogen bath until the whole solution is frozen;
- the valve is opened to vacuum and the atmosphere pumped away for a few minutes;
- the valve is then closed and a heat gun set at 150°C is used to thaw the solvent;
- the flask is refilled with nitrogen;
- these steps are repeated three times.

3.4.1.1 – Injection

The lead oleate flask is first heated to 118°C. A glass syringe with a 100 mm 16G stainless steel needle is used to rapidly inject the sulfur precursor into the lead oleate flask. The solution quickly turns red then dark brown. The hotplate's temperature controller is turned off while stirring continues. Once the flask returns to room temperature, 30 ml acetone (anhydrous $\geq 99.5\%$, Sigma-Aldrich) is injected, and the whole content is transferred into 50 ml centrifuge tubes (Nalgen[®], round bottom).

3.4.2 – Washing

The tube is centrifuged at 7500 rpm for 10 min. The supernatant is discarded, 10 ml toluene (analytical reagent, Ajax Finechem) is added, and the solution is stirred on a vortex mixer until completely dispersed. 10 ml ethanol (absolute, Ajax Finechem) and 25 ml acetone are added before a second vortex mixing and centrifugation process. This entire process is repeated three times, except that at the third repetition, the precipitate is not redispersed in any solvent.

3.4.3 – Weighing and redispersing

The precipitate is dried under a flow of argon, and then the tube is weighed again. Subtracting the weight of the empty tubes gives the total CQD mass (typically between 400 and 450 mg). The appropriate volume of n-octane (99+% extra pure, Sigma-Aldrich) is added to disperse a 45 g/l casting solution, which will be stored in a desiccator until further use.

3.5 – Device assembly

Figure 3.19 shows the final device ready for measurement in air. This section describes the chronological steps to achieve such a device, from the glass cutting and patterning to the TiO₂ electrode deposition, to the coating with PbS CQD layers, to the evaporation and sealing of the contacts. To scale up the assembly procedure, we prepared the first steps on large glass sheets that were cut into individual devices just before the CQD spin-coating step. That allowed us to maintain a certain consistency between the devices.

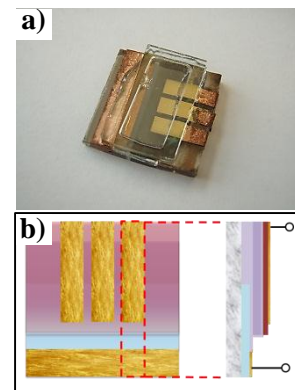


Figure 3.19 – (a) Complete device and (b) scheme displaying the various layers.

3.5.1 – FTO glass cutting and patterning

The device substrates are prepared from 305 mm × 305 mm sheets of glass coated with fluorine doped tin oxide (FTO) acquired from Nippon Sheet Glass (see specifications in Table 3.1).

Table 3.1 – Specifications of the FTO glass from NSG

Product	Thickness (mm)	Light Transmittance (%)	Solar Direct Transmittance (%)	Sheet Resistance (Ω/sq)	Haze (%)
NSG TEC™ A7 3.1mmt	3.1	81	69	7	5

The sheets are first cut into 100 mm × 100 mm squares using a diamond wheel. The slabs are then masked using Kapton® tape (polyimide tape) to protect the FTO (Figure 3.20) during the etching process.

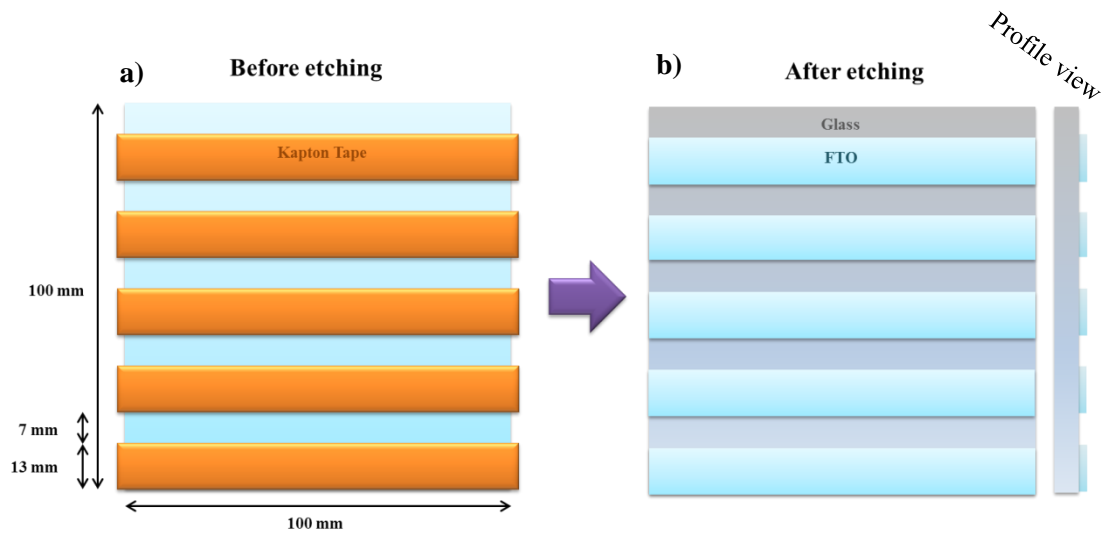
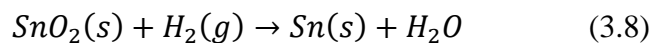
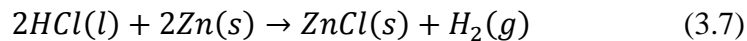


Figure 3.20 – Schematic diagram showing the glass sheet substrate (a) before and (b) after the chemical etching process.

The etching process consists of reducing and removing FTO with hydrogen released from the reaction between hydrochloric acid (HCl) and zinc (Zn):



Zinc powder (Sigma-Aldrich) is ground into a fine powder with a mortar and pestle and sifted through a sieve to spread a thin and uniform layer on the working

surface (large petri dish, glass board). The masked FTO glass is placed on the zinc powder layer, FTO side down. With a pipette, 4M HCl (37%, Ajax Finechem) in deionized water is dropped along the edges and sucked in under the glass by capillarity. As the reaction progresses, one can observe the hydrogen bubbling under the glass. The clear FTO surface in contact with the reactants gradually turns brown as tin oxide is reduced into tin. Finally, the tin is dissolved in the excess HCl, leaving a clear transparent surface. The whole process can take up to 10 minutes. It is important at this stage to not leave any unremoved patch of tin or tin oxide to avoid, any short circuits in the device. The glass is then rinsed with water and ethanol, dried and the Kapton[®] tape removed. The two point resistance measured across the gap is < 5 M Ω .

Then, the glass is subjected to a typical standard washing procedure. Multiple glass sheets can be inserted into a polypropylene container using spacers (see Figure 3.21). The container is filled consecutively with soapy water (concentrated dishwashing liquid), acetone, and ethanol. Each time, the container is sonicated for 20 minutes before having its liquid contents discarded.

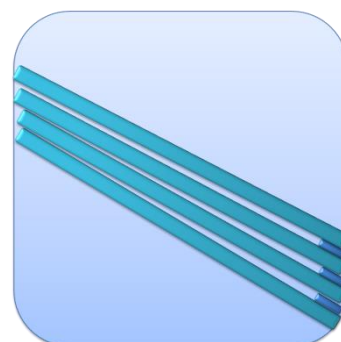


Figure 3.21 – Glass sheet arrangement for sonication.

Finally, the glass sheets can be kept in ethanol until further treatment. They are then dried using flowing nitrogen.

3.5.2 – Titanium dioxide dense layer deposition

The TiO₂ dense layer prevents direct short circuits between the conductive FTO and the quantum dots or the metal contacts. It is deposited on the substrates using manual laboratory spray pyrolysis glassware and a solution of titanium diisopropoxide bis(acetylacetonate) (TAA, 75% in isopropanol, Sigma-Aldrich).

The patterned FTO sheets are masked with 7 mm wide glass strips positioned as described in Figure 3.22, and fastened with Kapton[®] tape at the tips. The sheets are placed on a large and uniformly heated hot plate (Wenesco, HP1212YX) which is covered with aluminium foil. The heat is ramped to 400°C in 20 minutes and left for 5 minutes to let the equilibrium temperature stabilize. In the reservoir tube, TAA in ethanol (1:9 v/v) is stirred to reach homogeneity, and then, the reservoir tube is mounted on the spraying head. The sprayer is oriented along the glass strips to prevent any shadowing effect. Each spray round consists of a spray in each corner, and one at the centre to ensure complete coverage, followed by a waiting period of at least 10 sec to allow organic product to burn off.

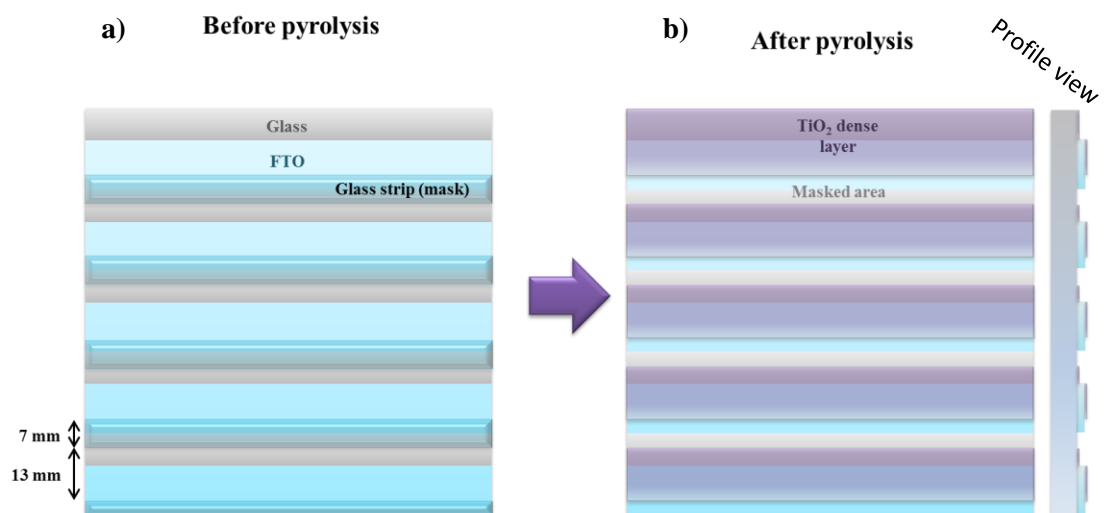


Figure 3.22 –Schematic diagram showing the glass sheet substrate (a) before and (b) after the spray pyrolysis process.

Our standard deposition requires 10 spray rounds, resulting in a 100 nm thickness (see profilometry plot in Figure 3.23).

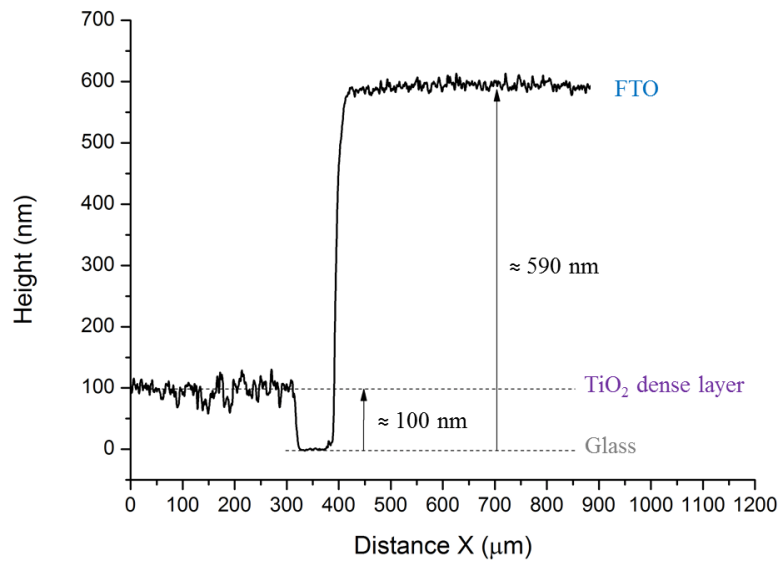


Figure 3.23 – Profilometry data showing FTO and TiO₂ thickness.

3.5.3 – Individual device cutting

Using the diamond wheel, the glass sheets are cut into individual substrates (20 mm x 20 mm) for further depositions (see Figure 3.24).

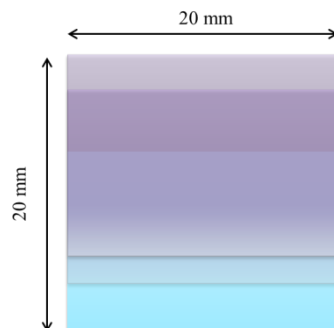


Figure 3.24 – Schematic diagram of a substrate after cutting into individual pieces.

3.5.4 – Colloidal quantum dot layer deposition

Prior to casting CQDs, Kapton[®] tape is used to mask the naked FTO surface. We used a layer-by-layer (LbL) process with a Laurell Ws-400-6npp Lite spincoater (Figure 3.25). The spin-coating technique consists of applying the material to be cast on the substrate and then use centrifugal forces (from high speed rotation) to spread it uniformly. We used this method in the context of PbS CQD deposition, as the ligand exchange process affects the nanocrystal at the surface more than the ones lying beneath.



Figure 3.25 – Laurell Ws-400-6npp Lite spincoater.

A syringe is filled with a 45 g/L PbS CQDs in n-octane and is then capped with a polytetrafluoroethylene (PTFE) syringe filter (1 μm membrane pores) to prevent clusters from reaching the substrate. Organic ligands are dissolved in a 2% v/v ratio in methanol (anhydrous 99.8%, Sigma-Aldrich), and inorganic PCl_5 (95%, Sigma-Aldrich) is dissolved in acetonitrile (anhydrous, Ajax Finechem) in a 0.5 mM concentration.

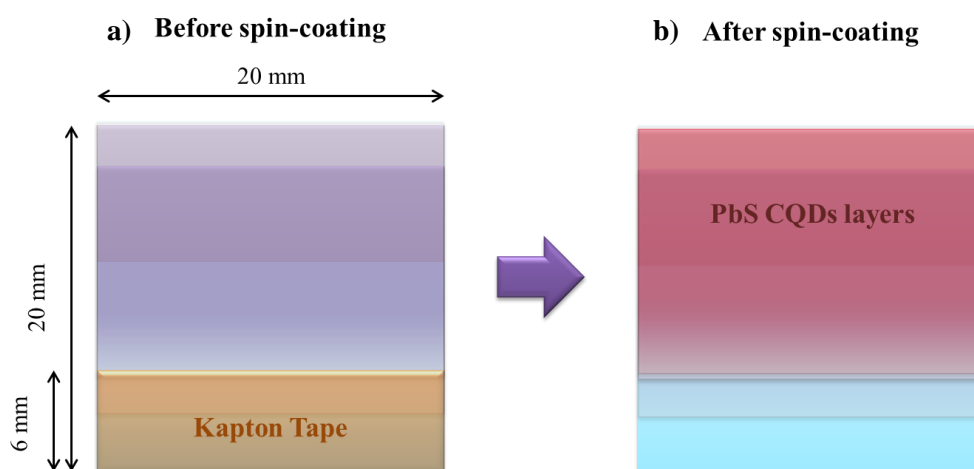


Figure 3.26 – Schematc diagram showing individual substrate (a) before and (b) after PbS CQD spin-coating.

The substrate is positioned on the chuck of the spin-coater sample. Once the lid is closed, an argon supply is inserted into the top hole and kept that way throughout the whole deposition procedure in order to reduce the moisture/oxygen level. All spin-coating steps were set at 2500 rpm.

In a typical single layer deposition, the PbS CQD solution is deposited dropwise from the syringe onto the substrate so it covers the whole surface (more solution required for the first layer due to the poor wettability) and is then immediately spun for 10 sec at 2500 rpm (no ramp rate). The ligand solution is deposited in the same way. Finally, the substrate is thoroughly rinsed using methanol and the heptane (anhydrous 99%, Sigma-Aldrich) while spinning: methanol removes unexchanged ligands, and heptane removes the remaining oleic acid capped CQDs. 11 spin-coating cycles were required for optimal devices, leading to a 150 nm film thickness. The final pattern is illustrated in Figure 3.26.

After PbS CQD deposition, the polyimide tape is removed, and the samples are kept under nitrogen flow until all devices are ready for the next step.

3.5.5 – Contact evaporation

Using polyimide tape, the substrates were positioned on a thin brass mask (Figure 3.27(a)) under an argon blanket (Figure 3.27(b)).

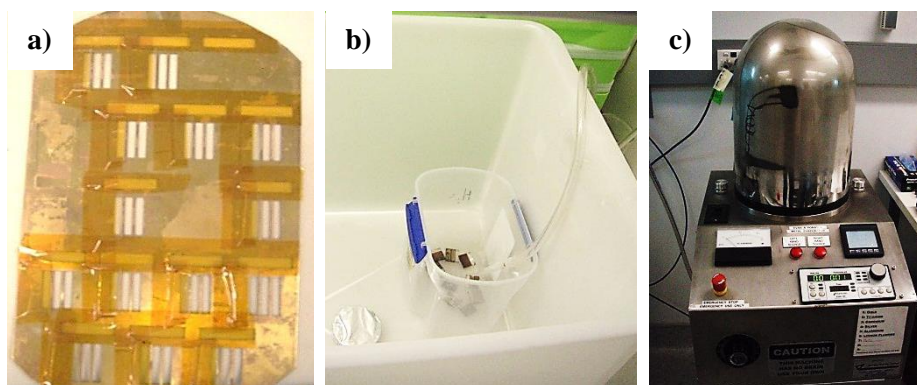


Figure 3.30 – Photograph showing (a) the argon blanket set-up, (b) the thin brass evaporation mask, and (c) the metal evaporator.

The samples are then inserted into a metal evaporator (custom built, AVT Services Pty. Ltd., Figure 3.27(c)). In the case of molybdenum oxide (MoO_3) evaporation, a second mask was used to protect the cathodes. The quartz crystal balance needed to be calibrated for MoO_3 evaporation. 5 nm, 10 nm and 100 nm films (displayed by the sensor) were then measured using a Dektak stylus profilometer (Figure 3.28), and we adjusted the Z-factor from the detector accordingly.

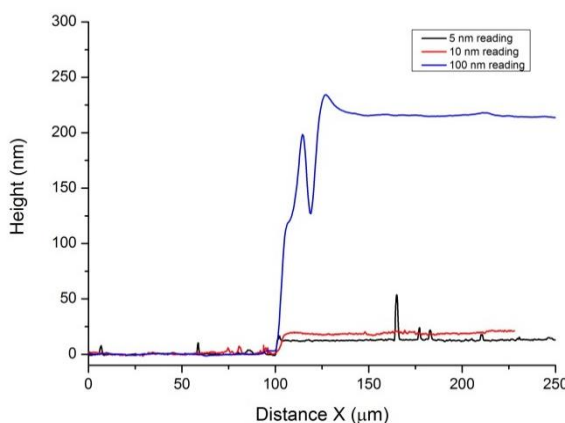


Figure 3.28 – Profilometry data showing MoO_3 film thickness for different evaporation thickness readings (on the quartz crystal balance).

The evaporation was carried out with chamber's pressure at $\sim 10^{-7}$ mbar. At higher pressures, the samples are liable to be thermally damaged as heat transport through convection is more significant. Typical devices are deposited with a 10 nm

MoO₃ layer followed by 70 nm gold (999.9 Swiss Bank Corporation Certified) with the pattern displayed in Figure 3.29. Each device has three pixels with an active area varying between 0.1 and 0.15 cm² (human error while aligning the evaporation mask). The spin-coated layer is expected to undergo strong “edge effects” in the neighbourhood of the tape, resulting in poor uniformity. A safe distance of ~1.5 mm is kept during the final contact evaporation.

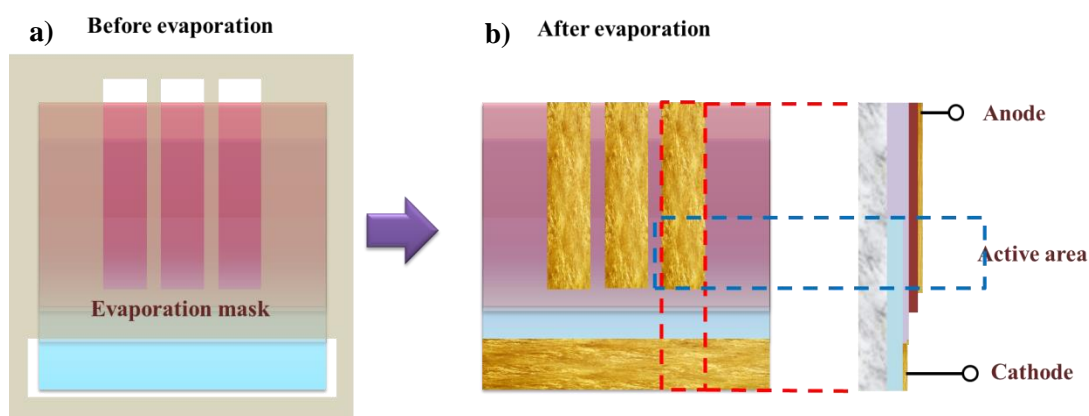


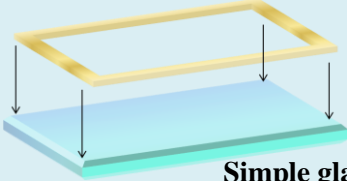
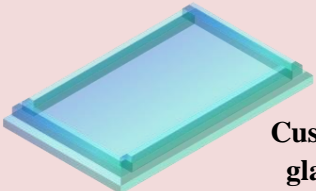
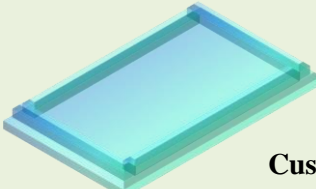
Figure 3.29 – Pattern description showing individual substrate (a) before and (b) after contact evaporation. The drawing on the right gives a cross-sectional view of the device.

After evaporation, the devices are immediately transferred into an argon atmosphere glove box.

3.5.6 – Sealing

In order to protect the devices from air, they are brought into a glove box and sealed with a glass cavity. Different sealing methods were investigated and are listed in Table 3.2.

Table 3.2 – Sealing methods

Cavity	Sealant	Comments
 <p style="text-align: right;">Simple glass slide</p>	<p>Dupont™ Surlyn®; The sealant must be pressed between the glass and the device at 120 °C for few minutes.</p>	<p>Further measurements inside the glove box showed negligible changes while outside testing showed consistent performance degradation. It was assumed that the sealant is not air-proof.</p>
 <p style="text-align: right;">Custom made glass cavity</p>	<p>Ultraviolet cured epoxy; requires a UV gun to be shone on it to harden.</p>	<p>Further testing in the glove box showed a direct decrease of the performance, most likely due to CQD film UV-photodegradation</p>
 <p style="text-align: right;">Custom made glass cavity</p>	<p>Reactive epoxy resins (2-components) requires the resin to be mixed with the hardener before applying on the cavity.</p>	<p>Both testing inside and outside the glove box showed long term stability (over a month) with less than 5% variation.</p>

References

1. Abe, S., K. Mochizuki, and K. Masumoto, *Solubility Range and Lattice-Constant of New Quaternary Solid-Solution Semiconductor PbI-XCAXSI-YSEY for Midinfrared Lasers*. Journal of the Japan Institute of Metals, 1992. **56**(12): p. 1479.
2. Pivrikas, A., et al., *A review of charge transport and recombination in polymer/fullerene organic solar cells*. Progress in photovoltaics: research and applications, 2007. **15**(8): p. 677.
3. Murray, C.B., et al., *Colloidal synthesis of nanocrystals and nanocrystal superlattices*. IBM Journal of Research and Development, 2001. **45**(1): p. 47.
4. Hines, M.A. and G.D. Scholes, *Colloidal PbS nanocrystals with size-tunable near-infrared emission: Observation of post-synthesis self-narrowing of the particle size distribution*. Advanced Materials, 2003. **15**(21): p. 1844.

CHAPTER 4 – CHARACTERIZATION OF CARBOXYLIC LIGAND TREATMENT

4.1 – Introduction

After synthesis, colloidal quantum dots (CQDs) are inherently capped with long molecular chain ligands, which act as bound surfactants controlling the size and shape of the crystals. These molecules are bonded to unstable sites that would otherwise bond with adventitious contamination (hydrocarbons, moisture) and change surface crystallinity. These ligands also act as stabilizers and make the CQDs dispersible in appropriate solvents, facilitating their casting. Once dried on a surface, however, long ligands continue to keep the nanocrystals apart, increasing the overall film resistivity. For this reason, an additional step, consisting of substituting the long alkyl chain molecule (here lead-oleate) for a shorter one (here dissolved in methanol) while keeping a relatively high degree of surface passivation is required. Ligand exchange and passivation mechanisms are widely used in this field, but still not fully understood. Using Fourier transform infrared spectroscopy (FTIR), the correlation of aliphatic vibrational absorption with the presence of oleic acid molecules in the sample was examined. The characterization of colloidal quantum dot (CQD) films with X-ray photoelectron spectroscopy (XPS) can give unique information regarding the presence of specific species of a same element and, by analogy, determine the role of the solvent (methanol) in the ligand exchange process, the capping proportion, and the influence of ambient atmosphere exposure on the surface states' stability. Also, the various electronic transitions were studied through absorption and photoluminescence

spectroscopy. 3-mercaptopropionic acid have been reported as the ligand leading to the best performance in PbS CQDs film based solar cells. It contains mostly a small alkene chain with a carboxylic group at one end and a sulfhydryl group (thiol) at the other end. In this work, we chose to compare this capping agent with two other similar molecules (Figure 4.1) to observe effect of a change in the alkene chain configuration on the overall passivation of the CQDs. The study also aims to uncouple the role of methanol and the ligands in the oleate removal process.

4.2 – Experimental

Five films were prepared as per the procedure described in Section 3.3.6 for comparative study:

- a) Oleic acid (OA) capped quantum dot layer (untreated);
- b) Same as (a), but washed with methanol (MetOH);
- c) Same as (a), but treated with 3-mercaptopropionic acid (MPA) in methanol;
- d) Same as (a), but treated with thioglycolic acid (TGA) in methanol;
- e) Same as (a), but treated with thiolactic acid (TLA) in methanol.

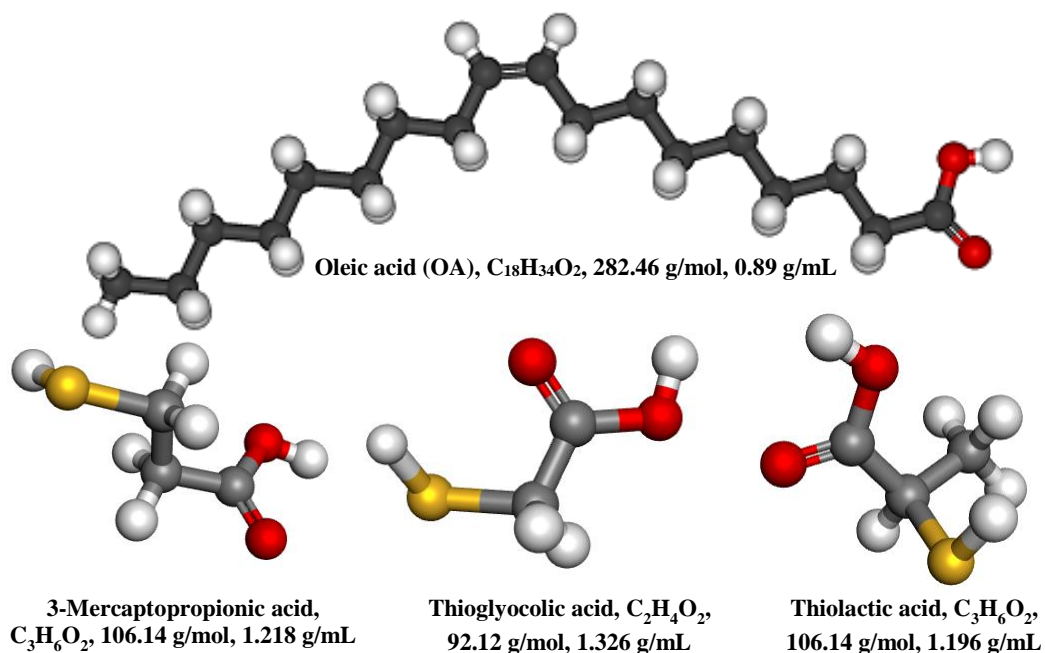


Figure 4.1 – Molecular structure of oleic acid, 3-mercaptopropionic acid, thioglycolic acid and thiolactic acid.

The preparation followed a similar procedure to the one used to deposit the PbS CQD layer on typical devices:

- 1) 100 μ L of a quantum dots solution (45 mg/mL) was drop casted on the substrate (10 mm \times 10 mm) immediately followed by spinning. End of procedure for sample (a);
- 2) For sample (b), the film was then simply rinsed with 500 μ L methanol, spun, then rinsed with heptane while spinning. For samples (c), (d) and (e), 100 μ L of a 2% v/v ligand solution (MPA, TGA and TLA, respectively) was drop casted on the film immediately followed by spinning;
- 3) Samples (c), (d) and (e) are rinsed with 500 μ L methanol, followed immediately by spinning;
- 4) Samples (b), (c), (d) and (e) are rinsed with 500 μ L heptane while spinning.

Each spin-coating step was carried out at 2500 rpm for 10 seconds (no acceleration ramping). The whole procedure was carried out in air, and the samples were not annealed at any time. For XPS measurements, the substrate was a 10 mm × 10 mm (100)-Si wafer and a single PbS CQDs film was cast. The samples were transferred into an argon glove box overnight before being inserted in the vacuum chamber of the XPS system. For ultraviolet (UV)-visible absorption spectroscopy, fluorescence spectroscopy, and infrared (IR) spectroscopy, the substrate was a 10 mm × 10 mm plain glass substrate with a 350 nm screen-printed mesoporous TiO₂ layer on top and four PbS CQDs films were cast.

4.3 – Results and discussion

4.3.1 – FTIR analysis

Figure 4.2 shows the FTIR spectra centred on the 2700-3100 cm⁻¹ range for each sample. The untreated sample displays two peaks around 2850 cm⁻¹ and 2925 cm⁻¹, which are respectively assigned to symmetrical and asymmetrical aliphatic stretching, which are believed to be a characteristic signature of the presence of oleic acid in each sample.

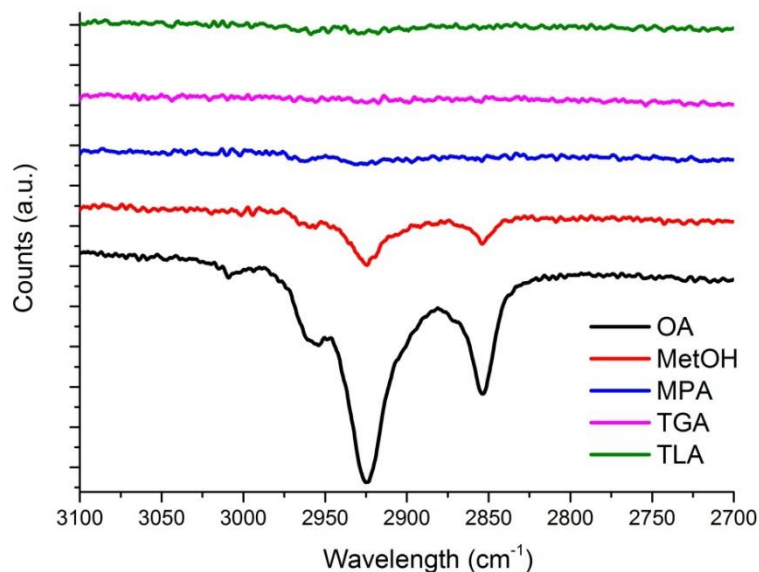


Figure 4.2 – IR spectra of the untreated sample (black) and the methanol (red), MPA (blue), TGA (magenta), and TLA (green) treated samples.

The films treated with the shorter ligands show a near total disappearance of this aliphatic stretching while the ligand-free methanol treatment shows still a small signal. This implies that the removal of oleic acid is partly caused by methanol dissolution of oleic acid combined with the presence of a compatible ligand which will substitute to the remaining molecules.

4.3.2 – XPS analysis

4.3.2.1 – Carbon (C 1s)

Figure 4.3 presents high resolution XPS spectra centred on C 1s, which was fitted with three distinct species for all samples.

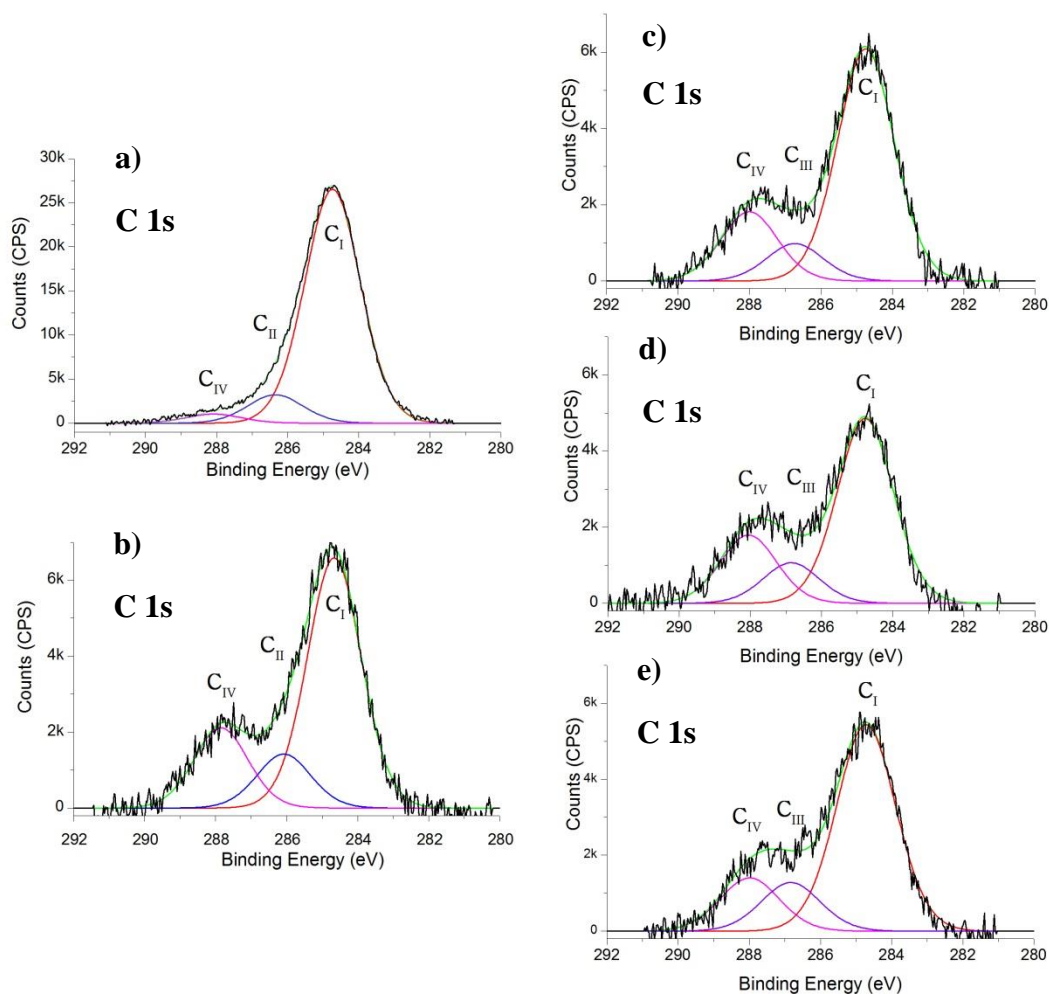


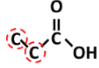
Figure 4.3 – XPS spectra centred on the C 1s peak for untreated (a), and methanol-only (b), MPA (c), TGA (d), and TLA (e) treated samples.

Each sample was referenced to its C 1s aliphatic group at 284.8 eV (C_I) to compensate for the surface charging effect.¹ The untreated sample (Figure 4.3(a)) revealed a high concentration of hydrocarbon species, reflecting the complete quantum dot coverage with oleic acid ligands which contains 17 C-H groups per molecule (see Figure 4.1). Following methanol treatment (Figure 4.3(b-e)), the film lost most of its aliphatic content. This demonstrates that methanol dissolves the initial capping ligands even without further ligand exchange. The intensity of component C_I for all methanol treated samples (with and without ligands) decreased to a minimum

value (~5,000 counts) and most likely comes from the unremoved oleic acid and adventitious contaminants. At these levels, the aliphatic signal is below the sensitivity threshold of the FTIR detector. The sample treated with only methanol displays, however, a certain C-H stretching content (Figure 4.2) which is most likely resulting from the fact that the several films were cast for this measurement. Multilayered systems improve the signal which was initially buried in noise (for single layer). The following layers may also react differently to the methanol treatment by reducing the oleate removal yield. Cass *et al.* claimed that methanol treatment was responsible for removing unbounded OA clusters through FTIR and H-NMR measurements.² This can be partly correlated with the results from Figure 4.3, assuming that these clusters account for most of the OA content.

The component C_{III} was present in all the samples and was reported to reflect the carboxylate group (O=C-O⁻).³ Bonds with a more electronegative element increase the electronic screening and tend to increase the binding energy. Component C_{II} had a binding energy relatively close to the aliphatic contribution, which was previously assigned to carbon atoms neighbouring a carboxylate group.⁴ C_{IV} was present in every ligand-exchanged sample at a similar content (Figure 4.3(c-e)) and can be assigned to the C-S group.^{5, 6} The various components and their assignments are listed in Table 4.1.

Table 4.1 – List of C 1s components observed on CQD film with XPS and their assignment.

Binding Energy (eV)	Species	Assignment
284.73±0.04	C _I	C-H
286.20±0.15	C _{II}	
286.80±0.07	C _{III}	C-S
287.99±0.09	C _{IV}	O=C-OH

4.3.2.2 – Oxygen (O 1s)

Figure 4.4 shows the various contributions to the O 1s peak for each sample. Among all the samples, the untreated one was the only one displaying a component O_{III} at 535.95 eV. This is a satellite peak from the COO group which has the same energy separation from its main peak (O_I) as C_{IV}.⁷ As the oleic acid capped CQD film was the only one displaying this feature, we can conclude that this long molecule tends to be more inclined to trap adventitious water molecules.

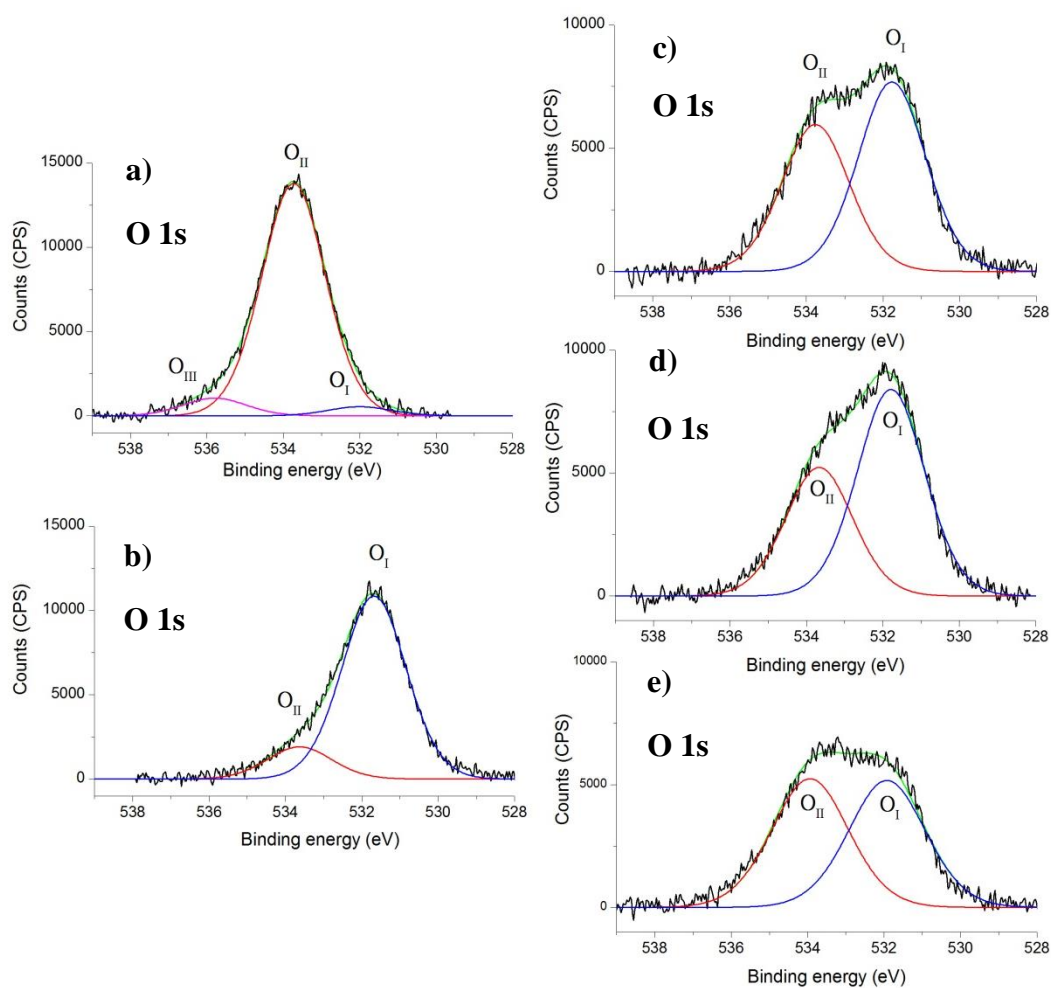
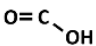


Figure 4.4 – XPS spectra centred on the O 1s peak for untreated (a), and methanol-only (b), MPA (c), TGA (d), and TLA (e) treated samples.

The signal of the untreated sample is mostly dominated by a second component (O_{II}) located at 533.74 ± 0.12 eV. It is believed to be coming from the oxygen atoms from the carboxylate groups as previously reported. This contribution is present in all the other samples, but at much lower content, especially with the methanol-only treatment. The remaining intensity from component O_{II} in this sample, however, reflects the residual “well-anchored” oleic acid molecules that could not be removed (as can be observed in Figure 4.2). By calculating the ratio between the components’ fitted areas for the untreated and methanol-only treated samples, we find that 86% of

the carboxylate groups were removed by this process. The intensity of the component O_{II} increases significantly when new ligands are dissolved in methanol, reflecting the presence of new carboxylate capping ligands at the surface of the CQDs. After treatment with methanol (with or without ligands), a new component (O_I) appears at 531.75 ± 0.05 eV. Various authors reported a sulfoxide contribution with relatively similar binding energies.⁸⁻¹⁰ Our apparatus could not detect any separation between SO₃⁻ and SO₄⁻ components ($\Delta BE \approx 0.7$ eV). Any attempt to fit this data with extra curves resulted in a worse match. Attributing an oxidized state to this component seems valid, however, as the oleic acid capped CQD sample is free from it, reflecting the efficient passivation and protection offered by this ligand. Moreover, the ligand-free methanol treatment, which removes most of the original ligands and thus leaves the surface unprotected, results in a significantly high content of component O_I. The samples which were treated with new ligands display this contribution as well, with intensity 26% lower for MPA, 19% lower for TGA, and 46% lower for TLA.

Table 4.2 – List of O 1s components observed on CQD film with XPS and their assignment.

Binding Energy (eV)	Species	Assignment
531.75±0.05	O _I	OH, SO _x ⁻
533.74±0.12	O _{II}	
535.94	O _{III}	Satellite of COO

In their work, Zhao *et al.*¹⁰ reported measuring the O 1s signal from similar samples (annealed in air). Unlike the current work, they observed a contribution of PbO around 529.4 eV, but no fingerprints from the ligands' carboxylic groups. It is

worth mentioning that the component O₁ has been attributed to the –OH specie in several publications¹¹⁻¹³ and might have a relatively significant contribution.

4.3.2.3 – Lead (Pb 4f)

The Pb 4f signal was fitted with two species with the following restrictions:

- 1) Pb 4f is divided into a doublet 4f_{5/2} and 4f_{7/2};
- 2) the area ratio 4f_{7/2}:4f_{5/2} was 4:3;
- 3) the position of 4f_{5/2} was shifted 4.86 eV towards higher binding energies with respect to the 4f_{7/2}.

In the following figures, the two fitted components follow the same colour code (Pb in blue, Pb in red, and the sum in kaki) and line styles (4f_{7/2} with a solid line and 4f_{5/2} with a dotted line).

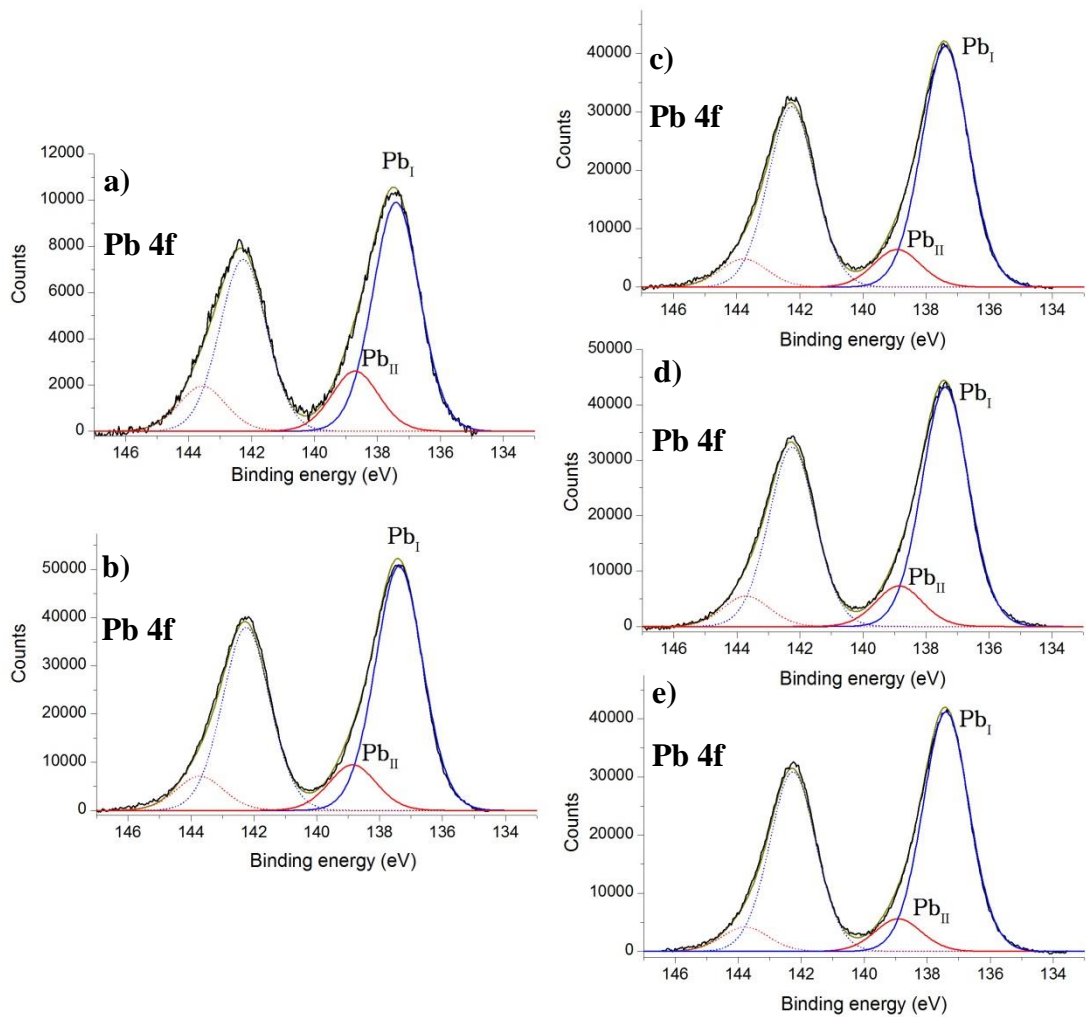


Figure 4.5 – XPS spectra centred on the Pb 4f peak for untreated (a), and methanol-only (b), MPA (c), TGA (d), and TLA (e) treated samples.

Figure 4.5 shows the XPS spectrum of the Pb 4f doublet in every sample. The first component Pb_I around 137.4 eV is undoubtedly assigned to Pb-S bonding, as previously reported.¹⁴⁻¹⁶ The second component Pb_{II} with a binding energy of 138.9 eV is also present in each sample in similar concentration and can be attributed to an oxidized form of lead. Luther *et al.* attributed this peak to the presence of PbO or Pb(OH)₂ while Tang et al. also assigned the presence of PbSO₃. It was observed that the content of Pb_{II} was slightly higher for the untreated sample but similar in the other

samples, suggesting that the nanocrystals are initially oxidized. It can be originating from the synthesis process, lead oleate being extremely sensitive to oxygen. During lead oleate preparation, the solution could turn from transparent to turbid yellow. This is caused by the oxidation of the precursor, and the synthesis process requires to be interrupted. Despite many precautions, the set-up might not have been completely air-proof, and small amount of material could have been oxidized even without any turbidity appearing. The oxidized peak, however, can also be related to the bond between lead atoms and the oleate ligand through a Pb-O-C bond. In this case, the Pb_{II} content in the other samples (without oleic acid) still needs to be addressed.

Table 4.3 – List of Pb 4f components observed on CQD film with XPS and their assignment.

Binding Energy (eV)	Component	Assignment
137.39 ± 0.01	Pb _I	Pb-S
138.85 ± 0.07	Pb _{II}	PbO, Pb(OH) ₂ , PbSO ₃

4.3.2.4 – Sulfur (S 2p)

The S 2p signal was fitted with the minimum number of components that could provide a good fit for all samples (minimum residual signal). Four species were observed and fitted with the following restrictions:

- 4) S 2p is divided into a doublet 2p_{1/2} and 2p_{3/2};
- 5) the area ratio 2p_{3/2}:2p_{1/2} was 2:1;

- 6) the position of $2p_{1/2}$ was shifted 1.18 eV towards higher binding energies with respect to the $2p_{3/2}$.

In the following figures, the four fitted components follow the same colour code (S_I in black, S_{II} in red, S_{III} in blue, S_{IV} in magenta, and the sum in kaki) and line styles ($2p_{3/2}$ with a solid line and $2p_{1/2}$ with a dashed line). The binding energies refer to the $2p_{3/2}$ components.

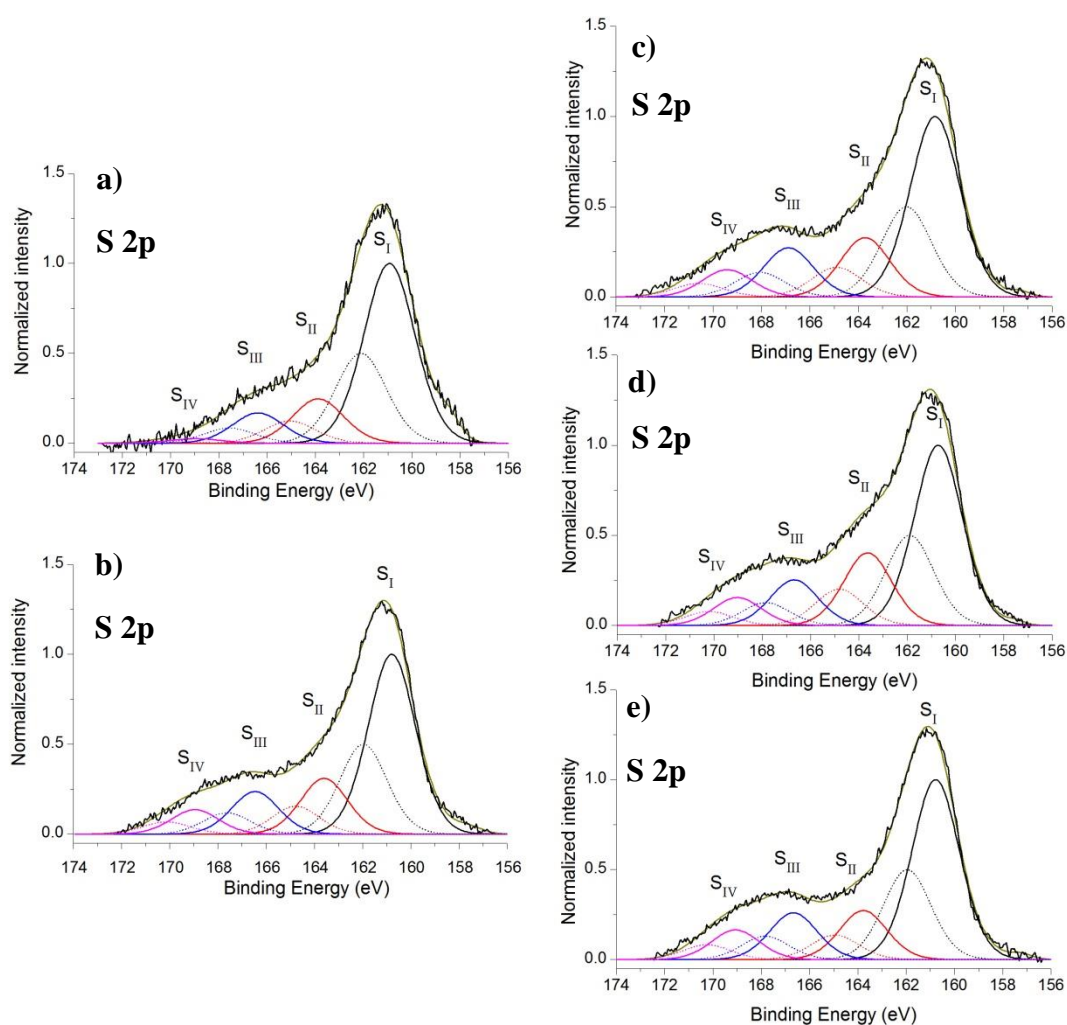


Figure 4.6 – XPS spectra centred on the S 2p peak for untreated (a), and methanol-only (b), MPA (c), TGA (d), and TLA (e) treated samples before ageing.

Figure 4.6 shows the XPS spectrum of the S 2p doublets for all the samples. The component S_I located at 160.8 eV (± 0.2 eV) is associated with the core-level from sulfur bonded with lead (Pb-S)¹⁷⁻¹⁹ originating from the quantum dot volumes more than from their surfaces and thus being less affected by the passivation treatment. The component S_{II} is located at 163.6 eV (± 0.2 eV) and appears to be more significant in the sample treated with TGA (see Table 4.4). The components S_{III} and S_{IV} are in lower content in the untreated sample.

4.3.2.5 – Sulfur (S 2p), after ageing in air

In order compare the impact of the different treatments on the surface reactivity to adventitious contaminants, the samples were kept outside of the analysis chamber in ambient atmospheric conditions for 5 days. Figure 4.7 shows the S 2p spectra for all samples after ageing in air.

Table 4.4 – Content of each S 2p component observed on CQD film with XPS before and after ageing process.

Binding Energy (eV)	Comp	Atomic ratio (%)									
		OA		MetOH		MPA		TGA		TLA	
		Before ageing	After ageing	Before ageing	After ageing	Before ageing	After ageing	Before ageing	After ageing	Before ageing	After ageing
160.8 \pm 0.1	S _I	69.5	58.3	59.5	40.3	57.1	47.7	55.3	46.4	58.9	50.4
163.6 \pm 0.1	S _{II}	17.1	22.2	18.4	33.7	18.7	25.3	22.3	26.7	16.1	25.1
165.6 \pm 0.2	S _{III}	11.7	14.2	14.0	17.1	15.5	18.9	13.9	18.6	15.3	16.1
169.2 \pm 0.2	S _{IV}	1.7	5.3	8.1	9.0	8.6	8.2	8.5	8.3	9.7	8.4

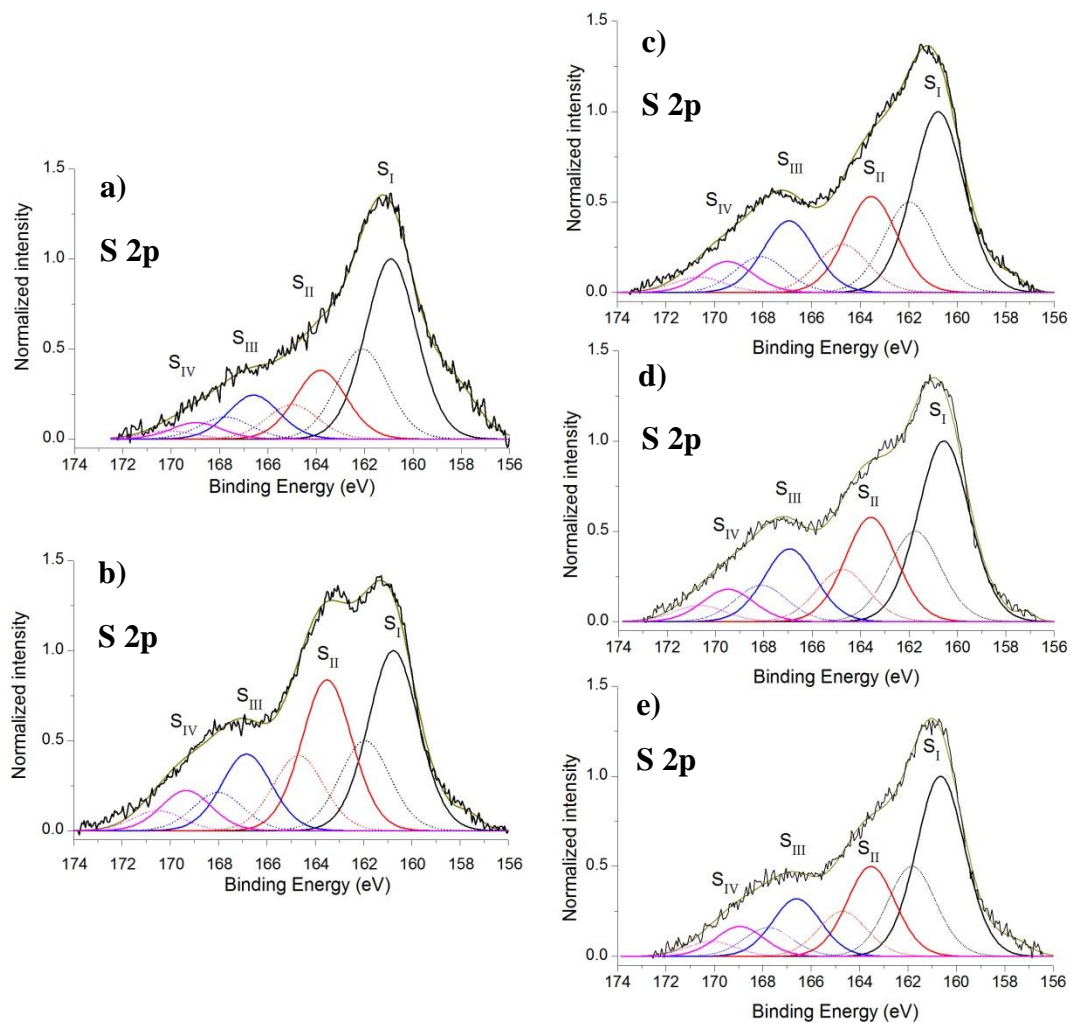


Figure 4.7 – XPS spectra centred on the S 2p peak for untreated (a), methanol-only (b), MPA (c), TGA (d) and TLA (e) treated samples after ageing.

The S 2p spectra gather more species than the other elements observed in the previous section, which are more likely related to uncontrolled passivation through adventitious reactants.

The component S_{II} increases in each sample after being exposed to air, especially after methanol-only treatment (see Figure 4.8).

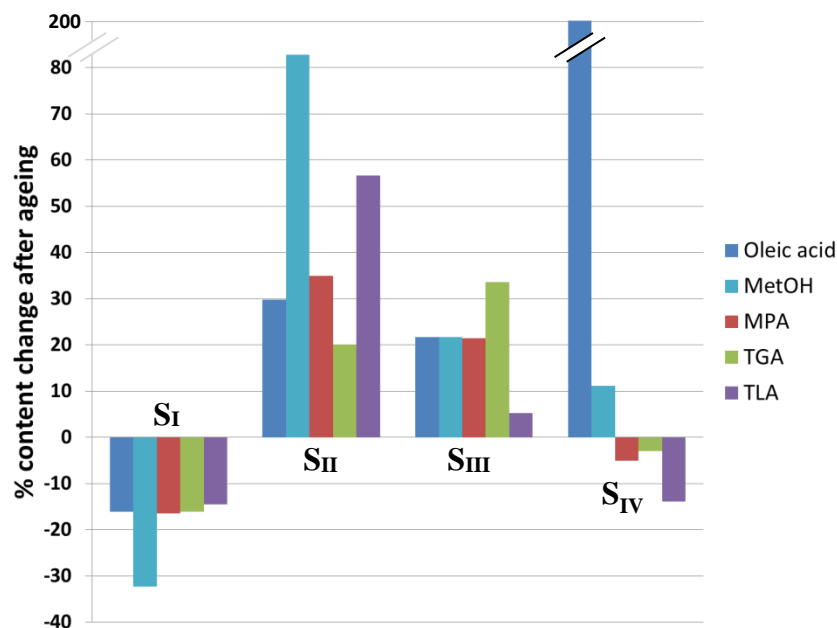


Figure 4.8 – Bar graph showing the content variation after ageing process of component S_I, S_{II}, S_{III} and S_{IV} for each sample.

Oleic acid is initially bound to Pb atoms as part of the lead oleate precursor compound (see Figure 4.9). Its removal is not expected to have such an impact on S atoms' stability except if:

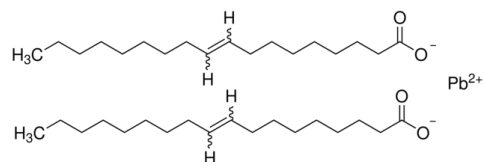


Figure 4.9 – Chemical structure of lead oleate.

- the surface stoichiometry is S-rich,^{14, 15} and oleic acid molecules are sterically protecting reactive sulfur sites (despite the fact that OA binds to on Pb atoms). In this case, component S_{II} could be assigned to a less oxidized specie (e.g. -SO, -SO₂, SOH) or the adsorption of an adventitious oxide weakly adsorbed on the surface;

- methanol treatment removes surface Pb atoms in the process, as previously described by Debnath *et al.*,²⁰ exposing unpassivated sulfur atoms, in which case component S_{II} could be assigned to disulphide bonding (S-S).^{17,20}

The second hypothesis can, however, be ruled out by the fact that S_{II} is clearly affected by atmospheric exposure and that MPA, TGA, and TLA treatments, using methanol as well, do not display such behaviour.

Partial esterification of carboxylic acid by methanol is considered as a possible pathway for the ligand molecules to be altered (Figure 4.10). Considering that these acids are weak and

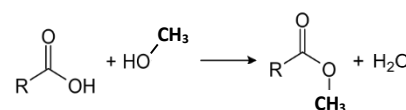


Figure 4.10 – Esterification of carboxylic acid by methanol

in the absence of an additional catalyst, this reaction is expected to be slow and incomplete. Nevertheless, the resulting moisture can hydrolyse the CQDs surface is previously suggested by Luther *et al.* for PbSe nanocrystals forming weak oxides (SO, SO₂) or hydroxides (-OH). Further exposure to air leads each sample to stay in contact with ambient moisture which contributes to this phenomenon. The unprotected methanol-only treated sample suffers the most from it as suggested by the significant increase in S_{II} content.

Component S_{III} (165.6 eV) was assigned to SO₃⁻ and kept increasing after ageing in air for every sample. The one treated with TLA (< 4%), however, showed a considerably smaller variation, suggesting that this ligand offers significant level of protection. S_{IV} (169.2 eV), attributed to SO₄⁻, and relatively small increase in the untreated sample after air exposure it reduces in samples treated with shorter ligands. This is unlikely to represent reality and this flawed observation is attributed to reduced signal due to accumulation of adventitious materials at the surface of the samples.

Thus, species which are in small amount like S_{IV} might undergo a relatively significant offset. However, it can be assumed that the change in S_{IV} content was negligible in the samples treated with shorter ligands.

The assignment for each S 2p component can be referred in Table 4.5.

Table 4.5 – List of S 2p components observed on CQD film from XPS and their assignment

Binding Energy (eV)	Component	Assignment
160.8±0.1	S _I	S-Pb
163.6±0.1	S _{II}	SO, SO ₂ , S-OH
165.6±0.2	S _{III}	SO ₃ ⁻
169.2±0.2	S _{IV}	SO ₄ ⁻

4.3.3 – Optical spectroscopy

4.3.3.1 – Optical absorption spectroscopy

Figure 4.11 shows the UV-visible absorption spectra of the samples cast on mesoporous TiO₂ substrates. The sample suspended in toluene spectrum is shown for comparison. The first excitonic peak <1S_h> - <1S_{1e}> is localized between 1.29 and 1.34 eV. We observe various shifts between the samples. Every peak is fitted with a Gaussian curve with the peak positions, the shift (relative to the untreated sample) FWHM are reported in Table 4.6.

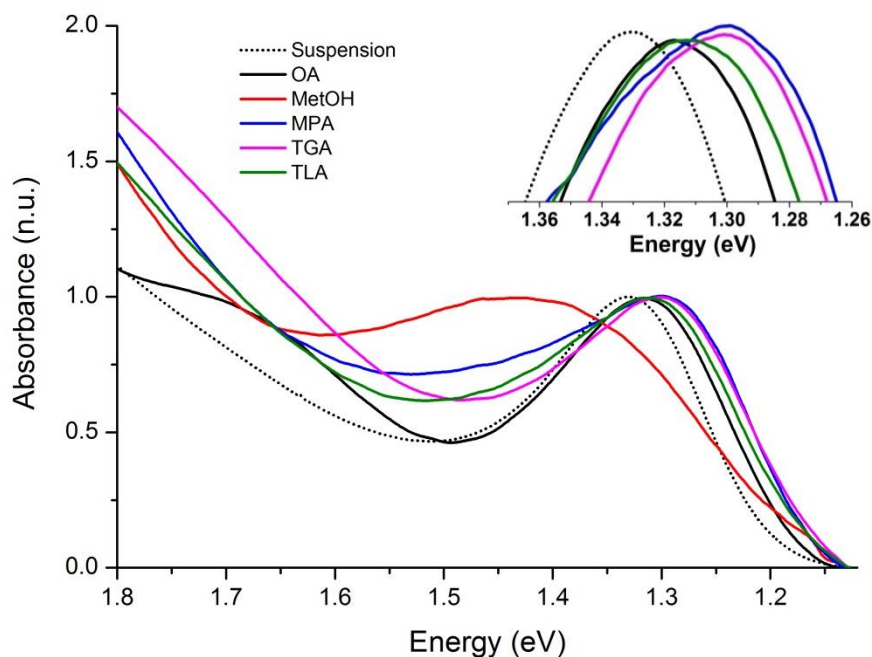


Figure 4.11 – Absorption spectra of suspended CQDs in toluene (dashed curve) and spin-coated films: untreated (black), methanol (red), MPA (blue), TGA (magenta) and TLA (green). The inset shows a higher resolution of the peaks maximum.

A small red shift (~ 14 meV) is observed between the suspended and the spin-cast OA capped CQDs. This phenomenon was previously reported^{21, 22} and is assigned to stronger coupling between CQDs coupling due to proximity. In the suspension at relatively low concentration (~ 1 mg/mL), the particles diffuse from one another to maximize the inter-dot separation distance. During the evaporation of the solvent from the solid surface, the particles are brought together by capillarity, only separated by their capping ligands. The closer the nanocrystals are to one another, the more significant the exciton orbital overlap will be (wavefunction delocalization)²³. As such the dielectric screening will be weaker²⁴ and charges will lose their confinement. In other words, the CQDs partially recover their bulk-like electronic/optical properties: a decrease of the bandgap as well as a broadening of the absorption peak. However, the peak broadening after film casting is negligible compared to what was reported by

Yang *et al.* and might reflect a poor coupling with the TiO₂ layer.²¹ The red shifts associated to the ligand exchanged samples are also expected to originate from CQDs coupling enhancement, although this interpretation was reported to not be accurate by Gao *et al.* as scattering and interference affects the signal. Nevertheless, following the trend of these shifts leads to $d_{\text{MPA}} < d_{\text{TGA}} < d_{\text{TLA}}$, with d_{ligand} being the inter-particle distance after ligand treatment. However, this result is counter intuitive as MPA is the longest molecule of the three. Further TEM or neutron scattering spectroscopy techniques are required to confirm this result.

Table 4.6 – Absorption peak position, shift from OA reference and FWHM.

	$E_{\text{abs}(i)}$ (eV)	$E_{\text{abs(OA)}} - E_{\text{abs}(i)}$ (meV)	FWHM (eV)
Oleic acid capped	1.316	-	0.177
Methanol treatment	1.410	-94	0.334
MPA treatment	1.300	16	0.186
TGA treatment	1.302	14	0.186
TLA treatment	1.310	6	0.178

The absorption peak from the methanol treated sample shows significant change: 94 meV blue shift, peak broadening and intensity drop (not displayed in the normalized spectra). The blue shift typically reflects apparent increase electronic confinement caused by size reduction. Following the four-band envelop formalism to calculate the PbS CQDs size^{25, 26}, we find that the apparent particle radius decreases from 1.83 nm to 1.71 nm, a loss in the order of 1.2 Å (± 0.4 Å). This value is about four times smaller than PbS crystal lattice parameter (5.94 Å) and could be assigned to a single atomic layer. Ihly *et al.* already reported that PbS CQDs oxidation can be characterized by:²⁷

- A blue shift as a fraction of the semiconducting crystal volume is converted into surface oxides which have wider band gaps;
- A peak broadening due to non-uniform oxidation process (the top crystals are more affected than the bottom ones).

This oxidized layer is significant enough to minimize the effect of agglomeration (proximity) which would affect electronic confinement in a similar fashion as for the ligand exchanged samples.

4.3.3.2 – Photoluminescence spectroscopy

Figure 4.12 shows the photoluminescence (PL) spectra of the five samples. Samples with exchanged ligands display a notable red shift (10-20 meV). Previous publications associated the red shift of the emission peak to a signature of Förster resonant energy transfer (FRET) where particle proximity increases the probability of transferring from a high-energy fluorophore to a lower-energy fluorophore through dipole-dipole interactions.^{28,29} In the present work, this shift appears concomitant with the red shift observed in the absorption spectrum. Moreover, FRET red-shift is mediated by a crystal size selected process where only bigger particles (low energy chromophores) emit, narrowing the linewidth of the emission peak. Here, ligand exchanged samples have an increased FWHM (Table 4.7). A significant difference between the intensity of the untreated (OA) sample and the others can be observed. This is associated to a system where radiative decay is faster than other type of charge transition processes and becomes the dominant pathway for electron-hole recombination.

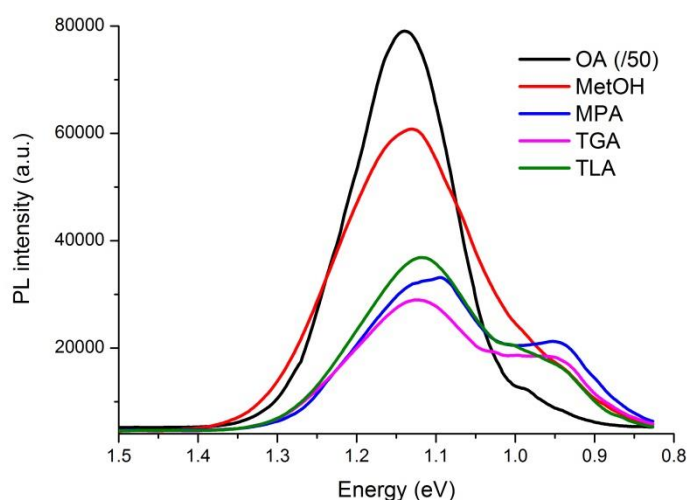


Figure 4.12 – Photoluminescence spectra for OA capped (black), methanol treated (red), MPA (blue), TGA (magenta) and TLA (green) capped samples.

Exciton dissociation via interparticle tunneling increases exponentially with the decrease of the crystal-to-crystal spacing. This decreases the population available for radiative recombination, and thus lowers PL intensity; consistent with the fact that CQDs are more densely packed after ligand exchange. This significant change in PL emission reflects an efficient QD-to-TiO₂ and QD-to-QD charge transfer. The PL intensity from the sample treated with methanol decreased significantly, suggesting an efficient ligand removal and resulting in a shorter interparticle spacing. Previous publications reported an increase in PL after controlled oxidation treatment^{30, 31} as the oxide shell became thicker and more uniform, thus preventing charge dissociation and forcing them to recombine radiatively. The weak PL intensity, however, suggests that charges still hop out of the QDs. An additional feature between 0.95 and 1.02 eV is present in each spectrum and will be discussed later.

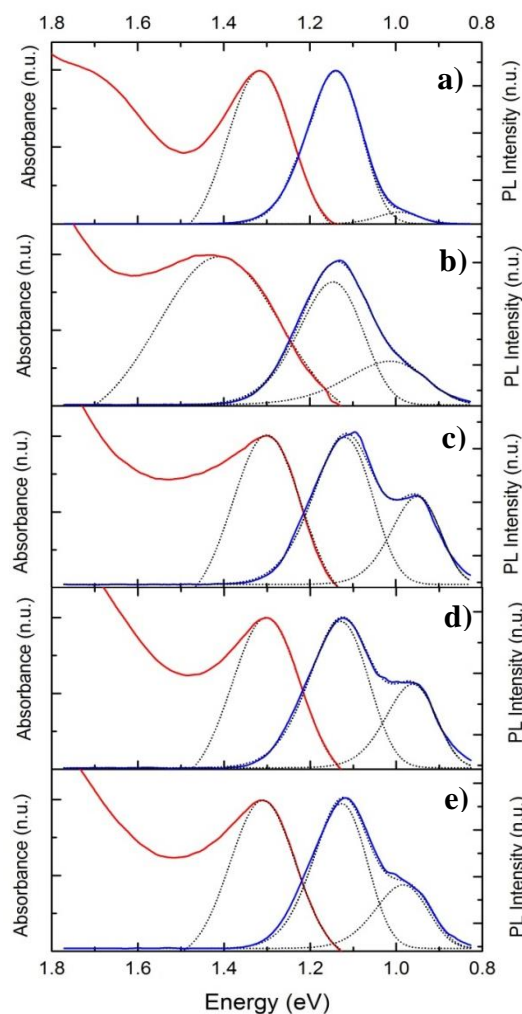


Figure 4.13 – Combined absorption (red) and emission (blue) spectra for OA capped (a), methanol treated (b) and MPA capped (c) samples. Each curve is fitted with a simple or a double Gaussian (black dot).

Figure 4.13 shows the absorption peak next to its analogous emission feature for OA capped, methanol treated, MPA, TGA and TLA capped samples. Absorption peaks were fitted with a simple Gaussian and emission peaks were fitted with a double Gaussian with no specific restriction. For every samples, the emission peak of each components, E_{Em1} and E_{Em2} , and their respective FWHM are reported in Table 4.7. Even if the component (1) is assigned to the same mechanism in each sample, it is clearly red shifted (10-20 meV) after ligand exchange. The energy difference between

the E_{Em1} and E_{Abs} was defined as the Stokes shift $E_{S1} = E_{Em1} - E_{Abs}$ (and analogously for E_{S2}).

Table 4.7 – Absorption and emission peak positions, FWHM and Stokes shifts for components (1) and (2) from the emission spectra for each sample.

Sample	E_{Abs} (eV)	E_{Em1} (eV)	FWHM(1) (eV)	Stokes shift E_{S1} (eV)	E_{Em2} (eV)	FWHM(2) (eV)	Stokes shift E_{S2} (eV)
Oleic acid capped	1.316	1.140	0.149	0.176	0.992	0.112	0.324
Methanol treatment	1.410	1.146	0.176	0.264	1.014	0.217	0.396
MPA treatment	1.300	1.119	0.163	0.181	0.950	0.134	0.350
TGA treatment	1.302	1.129	0.163	0.173	0.962	0.138	0.340
TLA treatment	1.310	1.127	0.148	0.183	0.984	0.144	0.326

Transition energy line broadening is known to originate from various phenomena including phonon scattering and CQDs polydispersity (Figure 4.14).³² Phonon scattering is the process of converting the energy from a relaxing charge carrier (electron) to internal lattice vibrations. This affects both PL emission energy and line width and is strongly temperature dependant. Gao *et al.* reported a FWHM decreased by 15-20 meV once cooled below 100K. Polydispersity originates from the non-uniform reaction during the nanocrystals synthesis. In this size range (3-5 nm diameter), 1 Å size deviation leads to 20-60 meV absorption shift which mostly impacts on the electron affinity (χ). The absorption peak broadening for ligand-free treatment is expected to be affected by this phenomenon as the oxidizing process is

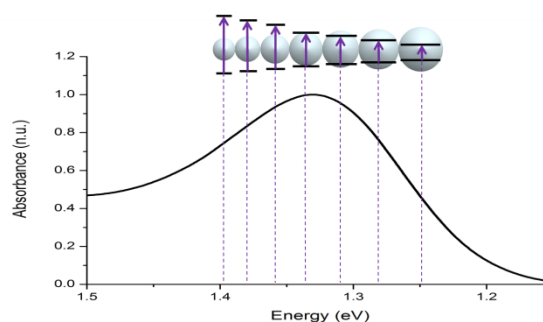


Figure 4.14 – Schematic illustration of polydispersity on line broadening.

non-uniform. All samples showed small but consistently narrowed emission peaks (both E_{Em1} and E_{Em2}) when compared to their respective absorption spectrum. Even the methanol treated sample displays a FWHM in the range of the other samples. These results suggest that the electronic states involved in radiative transitions are not as affected by phonon scattering and/or polydispersity as the ones involved in the absorption transitions.

Stokes shifts are known to represent energy losses between the absorption final state and the emission initial states. Typical molecular Stokes shifts are described by the Franck-Condon principle which attributes the likelihood of a transition to the vibronic overlap between the initial and the final states wavefunctions. These mechanisms, however, are dominant at a molecular scale ($< 2\text{ nm}$) where the impact of structural conformation takes over the periodicity of the lattice.³³ In the past, researches have proposed various explanations for such high Stokes shift including dark exciton intermediate state.^{34, 35} Briefly, excitons are the combination of an electron (spin $\pm 1/2$) and a heavy hole ($\pm 3/2$) generating spin ± 1 (bright exciton) and ± 2 (dark exciton) states. A photon can not carry away more than 1 quantum of angular momentum so an electron can not transit to a spin ± 2 through photoexcitation (optically inactive), but can relax from a bright exciton state to a dark exciton state. The splitting was reported, however, to be rather small^{36, 37} and can not be assigned to the Stokes shift measured in the present work. On the other hand, Allen and Delerue predicted excitonic fine structure splitting of the eightfold degenerate ground state arising from inter-valley scattering.³⁸

The most reported interpretation remains the presence of in-gap energy levels located near the conduction band edge and induced by lattice defects, especially due

to surface passivation issues.³⁹⁻⁴¹ The surface reconstruction plays a dominant role in the CQDs electronic behaviour and is unique to the growth/quenching mechanisms, to the precursors' reactivity and to the type of solvents and passivating agent used in the synthesis process. It was reported that PbS quantum dots fabricated in polymer and glass matrices show significantly different confinement energy dependence on particle size.⁴²⁻⁴⁸ These past reports, added to the present results, suggest that the type of surface passivation, size distribution and matrix characteristics can affect significantly the energy level configuration which can be analysed through small perturbations in the Stokes shift.

Here, the in-gap trap states have been considered playing a dominant role in the Stokes shift. As such, a Jablonski diagram for the current system is illustrated in Figure 4.15, where E_{abs} can be associated to the $\langle 1S_h \rangle - \langle 1S_e \rangle$ exciton level, while E_{em1} and E_{em2} are attributed to radiative transitions emitted from medium and deep in-gap levels, respectively.

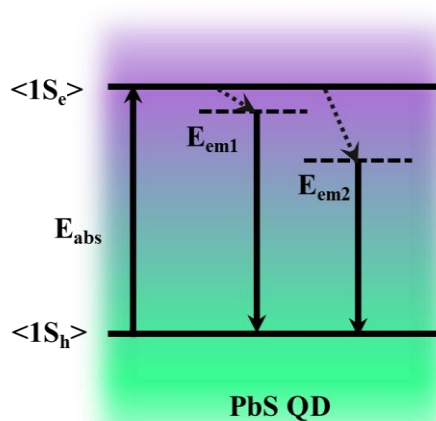


Figure 4.15 – Jablonski diagram associating E_{abs} to the first $\langle 1S_h \rangle - \langle 1S_e \rangle$ exciton level, E_{em1} and E_{em2} to radiative transition emitted from medium and deep in-gap levels, respectively.

The total PL quantum yield could not be measured as the apparatus was not equipped with an integrating sphere, however, it is assumed that the amount of photons reaching the detector reflects the total amount of photons emitted by the sample on a comparative ratio level as all measurement conditions were the same (excitation wavelength, angle, slits) and lie in the same sensitivity region of the detector. $A_{p,i}$ is defined as the area under the component i (1, 2 or 1+2) assigned to a specific passivation p (OA, MetOH, MPA, TGA or TLA). The PL quenching observed in each treated sample is similar: $A_{MetOH,1+2}/A_{OA,1+2} = 3.7\%$ and $A_{MPA,1+2}/A_{OA,1+2} = 2.7\%$ (same results for TGA and TLA $\pm 0.1\%$). Nevertheless, the ratio between each component, $A_{p,1}/A_{p,1+2}$, changes drastically after quenching (Table 4.8).

Table 4.8 – Ratio between the integral under the first component E_{Em1} and the area under the whole curve.

Passivation p	$A_{p,1}/A_{p,1+2}$ (%)
OA	94
MetOH	62
MPA	58
TGA	57
TLA	59

If one is to assume that, in the case of OA capped QDs, no injection in TiO₂ takes place due to the wide interparticle spacing, this ratio corresponds to the proportion of excited electrons from the $\langle 1S_e \rangle$ level favouring E_{Em1} over E_{Em2} (Figure 4.16(a)). Removing or replacing the OA ligand should, however, keep this ratio consistent, assuming that the exciton trapping rate into E_{Em1} and E_{Em2} have the

same dependence on the photogenerated exciton density in $\langle 1S_e \rangle$, and assuming that injection of an electron in the TiO_2 is the only cause for the quenching process. This suggests that the deeper trap level captures electron another source but $\langle 1S_e \rangle$.

Following $\chi_{\text{TiO}_2} \approx 4.2 \text{ eV}$ and $\chi_{\text{CQD}} \approx 3.9 \text{ eV}$,²⁶ the position of the TiO_2 conduction band (E_{CB}) is expected to lie approximately 0.3 eV below the first exciton level $\langle 1S_e \rangle$. The state from which E_{Em2} is emitted, lies 325-400 meV below $\langle 1S_e \rangle$ and can capture charges from E_{CB} before they can diffuse away (Figure 4.16(b)). This mechanism can explain the higher intensity ratio $A_{p,1}/A_{p,1+2}$ after treatment.

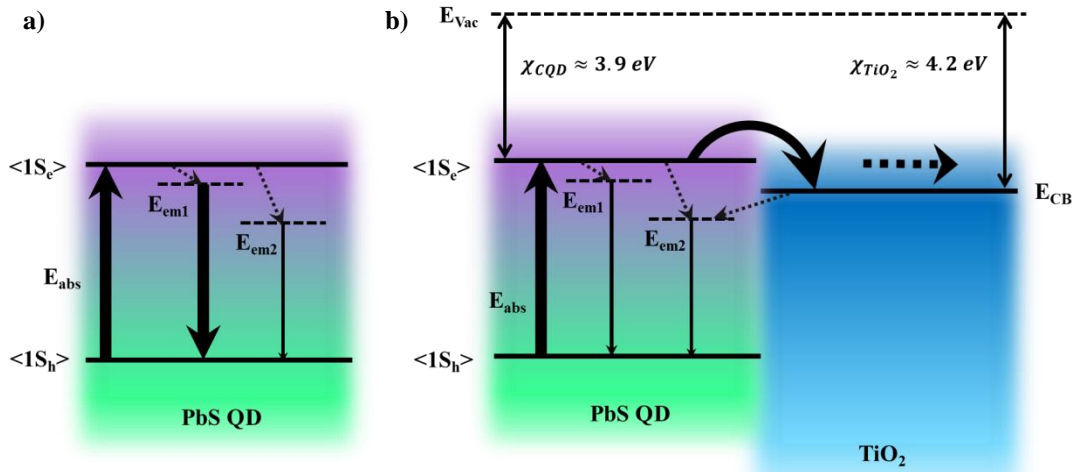


Figure 4.16 – Illustration of possible pathways for isolated CQDs (a) and for CQDs connected to TiO_2 (b). The thickness of the arrows is a qualitative indication of the proportion of electron involved in the pathway.

For a system in steady state condition, one can calculate the ratio of recaptured

electrons over the injected population $\frac{A_{\text{recap}}}{A_{\text{inj}}}$ following:

$$\frac{A_{\text{recap}}}{A_{\text{inj}}} = \frac{A_{p,2} - (A_{\text{OA},2} - A_{\text{inj},2})}{A_{\text{inj},1} + A_{\text{inj},2}}$$

where $A_{inj,1} = A_{OA,1} - A_{sample,1}$ and $A_{inj,2} = \frac{A_{inj,1} \times A_{OA,2}}{A_{OA,1}}$ are the relative proportions of electron injected in TiO_2 instead of transiting in E_{Em1} and E_{Em2} , respectively. This calculation shows that samples treated with the new ligands have 1% of their injected charges recaptured by the deeper trap level while the sample treated with methanol-only shows 1.3%.

Table 4.9 – Proportion of recaptured electrons over injected electrons into TiO_2 .

Passivation p	A_{recap}/A_{inj} (%)
MetOH	1.27
MPA	1.06
TGA	1.02
TLA	1.03

In order to compare the impact of each ligand on the transitional configuration of the CQD films on a Jablonski diagram (Figure 4.17), the positions of the $\langle S1_h \rangle$ levels were aligned. This approximation was made following the assumption that the ionisation energy is the parameter which is the least influenced by variation in the confinement energy according the most models.^{26, 38, 49}

Konstantatos *et al.* previously reported the trapping properties of such films requiring by detecting distinct activation energy between 0.1 and 0.3 eV which could be attributed to the presence of oxidated species at the surface.^{18, 50} The energy shifts below 30 meV, being in the range of room temperature activation energy ($k_B T$), are not considered as accurate, but are relevant for comparative observations.

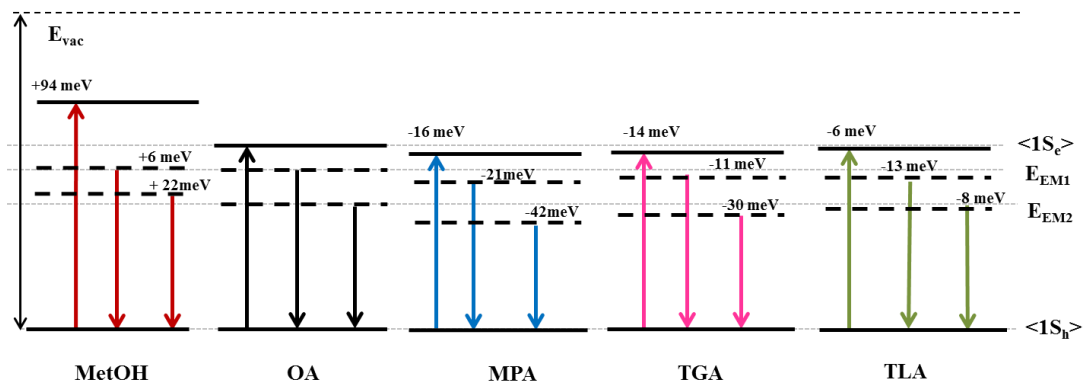


Figure 4.17 – Jablonski diagrams for each sample. The solid lines represent the $\langle 1S_h \rangle$ and $\langle 1S_e \rangle$ exciton energy levels, and the dashed lines represent the in-gap states. The energies displayed represent the shift with the OA sample energy levels (grey dashed line).

As mentioned earlier, the increase in the band gap of the sample treated with only methanol is expected to reflect a size reduction in the order of 3-4 Å (c.a. an atomic monolayer) due to a significant conversion of PbS into oxide. The in-gap levels are not shifted accordingly to the $\langle 1S_e \rangle$ displacement, however, and the trap depths (associated to the Stokes shifts) are considerably increased. For the ligand exchanged samples, on the other hand, the displacement of the exciton level towards lower energy is relatively small but reflects the partial orbital overlap between the QDs as they are closer from one another. It can be observed that the TLA ligand shows the least change in the electronic configuration while still showing similar injection efficiency in TiO_2 , suggesting that the QDs are brought closer but still retain comparable confinement to the untreated sample. MPA and TGA treated samples showed deeper traps (30-40 meV shift).

4.4 – Conclusion

Using FTIR and XPS, the influence of ligand and ligand-free treatments on the oleic acid coverage was determined. Methanol alone appears to remove more than 86 % of OA capping. We observed that despite the fact that OA is specifically bonded to Pb-sites, it protects exposed S-sites from atmospheric exposure. Ligand-free samples aged in air for 5 days show a significantly higher content of a component that we assigned to less oxidized sulfur compounds (-SO, -SO₂, -SOH) or to weakly adsorbed adventitious oxides. Using UV-Vis-NIR absorption, a strong blue shift was observed in the spectrum of the methanol-only treated sample. The calculated radius reduction (1-2 Å) could possibly be attributed to oxidation of a single atomic monolayer. Two distinct features were observed in the photoluminescence spectrum of each sample, attributed to a shallow and a deep in-gap energy level. The luminescence quenching effect on ligand exchanged samples was attributed to enhanced electron injection into TiO₂ particles. The proportion of recaptured electron was calculated to be around 1-1.3 %. The sample treated with TLA showed less oxidation (including SO₃⁻ and SO₄⁻) and good injection efficiency in TiO₂ while displaying the least electronic configuration change.

References

1. Crist, B.V., *Handbook of Monochromatic XPS Spectra: The elements and native oxides*. 2000: Wiley.
2. Cass, L.C., M. Malicki, and E.A. Weiss, *The Chemical Environments of Oleate Species within Samples of Oleate-Coated PbS Quantum Dots*. *Analytical Chemistry*, 2013. **85**(14): p. 6974.
3. Fang, Y., et al., *Enzymatic transglycosylation of PEG brushes by beta-galactosidase*. *Chemical Communications*, 2012. **48**(91): p. 11208.
4. Giesbers, M., A.T.M. Marcelis, and H. Zuilhof, *Simulation of XPS C1s Spectra of Organic Monolayers by Quantum Chemical Methods*. *Langmuir*, 2013. **29**(15): p. 4782.
5. Campos, M.A.C., J.M.J. Paulusse, and H. Zuilhof, *Functional monolayers on oxide-free silicon surfaces via thiol-ene click chemistry*. *Chemical Communications*, 2010. **46**(30): p. 5512.
6. Techane, S.D., L.J. Gamble, and D.G. Castner, *X-ray photoelectron spectroscopy characterization of gold nanoparticles functionalized with amine-terminated alkanethiols*. *Biointerphases*, 2011. **6**(3): p. 98.
7. Jones, G., et al., *The local adsorption geometry and electronic structure of alanine on Cu {110}*. *Surface science*, 2006. **600**(9): p. 1924.
8. Nasef, M.M., et al., *XPS studies of radiation grafted PTFE-g-polystyrene sulfonic acid membranes*. *Journal of Applied Polymer Science*, 2000. **76**(3): p. 336.
9. Zingg, D.S. and D.M. Hercules, *Electron-Spectroscopy for Chemical Analysis Studies of Lead Sulfide Oxidation*. *Journal of Physical Chemistry*, 1978. **82**(18): p. 1992.
10. Zhao, N., et al., *Colloidal PbS Quantum Dot Solar Cells with High Fill Factor*. *ACS Nano*, 2010. **4**(7): p. 3743.
11. Li, Z.W. and Y.F. Zhu, *Surface-modification of SiO₂ nanoparticles with oleic acid*. *Applied Surface Science*, 2003. **211**(1-4): p. 315.

12. Shirazi, S.N., *Wet Chemical Surface Modifications of Titanium and Ti6Al4V Alloy and Their Effect on the Hydrothermal Aging Mechanisms and Adhesion Properties*. 2010.
13. Clark, D.T., B.J. Cromarty, and A. Dilks, *Theoretical Investigation of Molecular Core Binding and Relaxation Energies in a Series of Oxygen-Containing Organic-Molecules of Interest in the Study of Surface Oxidation of Polymers*. *Journal of Polymer Science Part A-Polymer Chemistry*, 1978. **16**(12): p. 3173.
14. Choi, H., et al., *Steric-Hindrance-Driven Shape Transition in PbS Quantum Dots: Understanding Size-Dependent Stability*. *Journal of the American Chemical Society*, 2013. **135**(14): p. 5278.
15. Tang, J., et al., *Quantum Dot Photovoltaics in the Extreme Quantum Confinement Regime: The Surface-Chemical Origins of Exceptional Air- and Light-Stability*. *ACS Nano*, 2010. **4**(2): p. 869.
16. Luther, J.M., et al., *Structural, optical and electrical properties of self-assembled films of PbSe nanocrystals treated with 1,2-ethanedithiol*. *ACS Nano*, 2008. **2**(2): p. 271.
17. Lobo, A., et al., *Photoelectron spectroscopic investigations of chemical bonding in organically stabilized PbS nanocrystals*. *Journal of Physical Chemistry B*, 2005. **109**(37): p. 17422.
18. Konstantatos, G., et al., *Engineering the temporal response of photoconductive photodetectors via selective introduction of surface trap states*. *Nano Letters*, 2008. **8**(5): p. 1446.
19. Peterson, P.J., *Corrosion of Electronic and Magnetic Materials*. 1992: ASTM.
20. Debnath, R., et al., *Ambient-Processed Colloidal Quantum Dot Solar Cells via Individual Pre-Encapsulation of Nanoparticles*. *Journal of the American Chemical Society*, 2010. **132**(17): p. 5952.
21. Yang, Y., et al., *Strong Electronic Coupling and Ultrafast Electron Transfer between PbS Quantum Dots and TiO₂ Nanocrystalline Films*. *Nano Letters*, 2012. **12**(1): p. 303.
22. Mora-Sero, I., et al., *Selective contacts drive charge extraction in quantum dot solids via asymmetry in carrier transfer kinetics*. *Nature Communications*, 2013. **4**.

23. Schedelbeck, G., et al., *Coupled quantum dots fabricated by cleaved edge overgrowth: From artificial atoms to molecules*. *Science*, 1997. **278**(5344): p. 1792.
24. Rogach, A., *Semiconductor Nanocrystal Quantum Dots: Synthesis, Assembly, Spectroscopy and Applications*. 2008: Springer London, Limited.
25. Elfurawi, U., *Optical and Electronic Properties of PbS Colloidal Nanocrystals*, in *School of Physics and Astronomy*. 2012, University of Nottingham: Nottingham.
26. Hyun, B.R., et al., *Electron Injection from Colloidal PbS Quantum Dots into Titanium Dioxide Nanoparticles*. *ACS Nano*, 2008. **2**(11): p. 2206.
27. Ihly, R., et al., *The Photothermal Stability of PbS Quantum Dot Solids*. *ACS Nano*, 2011. **5**(10): p. 8175.
28. Clark, S.W., J.M. Harbold, and F.W. Wise, *Resonant energy transfer in PbS quantum dots*. *The Journal of Physical Chemistry C*, 2007. **111**(20): p. 7302.
29. Xu, F., et al., *Efficient exciton funneling in cascaded PbS quantum dot superstructures*. *ACS Nano*, 2011. **5**(12): p. 9950.
30. Liu, L.P., Q. Peng, and Y.D. Li, *An effective oxidation route to blue emission CdSe quantum dots*. *Inorganic Chemistry*, 2008. **47**(8): p. 3182.
31. Wang, X.Y., et al., *Photo-oxidation-enhanced coupling in densely packed CdSe quantum-dot films*. *Applied Physics Letters*, 2003. **83**(1): p. 162.
32. Zhitomirsky, D., et al., *Colloidal Quantum Dot Photovoltaics: The Effect of Polydispersity*. *Nano Letters*, 2012. **12**(2): p. 1007.
33. Franceschetti, A. and S.T. Pantelides, *Excited-state relaxations and Franck-Condon shift in Si quantum dots*. *Physical Review B*, 2003. **68**(3).
34. Sallen, G., et al., *Dark exciton optical spectroscopy of a semiconducting quantum dot embedded in a nanowire*. arXiv preprint arXiv:0903.0497, 2009.

35. Bagga, A., P. Chattopadhyay, and S. Ghosh. *Stokes shift in quantum dots: Origin of dark exciton*. in *Physics of Semiconductor Devices, 2007. IWPSD 2007. International Workshop on*. 2007. IEEE.
36. Espiau de Lamaestre, R., et al., *Evidence for a “dark exciton” state of PbS nanocrystals in a silicate glass*. Applied Physics Letters, 2006. **88**(18): p. 181115.
37. Gaponenko, M.S., et al., *Temperature-dependent photoluminescence of PbS quantum dots in glass: Evidence of exciton state splitting and carrier trapping*. Physical Review B, 2010. **82**(12): p. 125320.
38. Allan, G. and C. Delerue, *Confinement effects in PbSe quantum wells and nanocrystals*. Physical Review B, 2004. **70**(24): p. 245321.
39. Lewis, J., S. Wu, and X. Jiang, *Unconventional gap state of trapped exciton in lead sulfide quantum dots*. Nanotechnology, 2010. **21**(45): p. 455402.
40. Bakulin, A.A., et al., *Charge Trapping Dynamics in PbS Colloidal Quantum Dot Photovoltaic Devices*. ACS Nano, 2013. **7**(10): p. 8771.
41. Gao, J. and J.C. Johnson, *Charge Trapping in Bright and Dark States of Coupled PbS Quantum Dot Films*. ACS Nano, 2012. **6**(4): p. 3292.
42. Okuno, T., et al., *Strong confinement of PbSe and PbS quantum dots*. Journal of Luminescence, 2000. **87**: p. 491.
43. Kuljanin, J., et al., *Synthesis and characterization of nanocomposite of polyvinyl alcohol and lead sulfide nanoparticles*. Materials chemistry and physics, 2006. **95**(1): p. 67.
44. Kostić, R., et al., *Photoluminescence and far-infrared spectroscopy of PbS quantum dots–Polyvinyl alcohol nanocomposite*. Optical Materials, 2008. **30**(7): p. 1177.
45. Lu, S., et al., *Synthesis and characterization of PbS nanoparticles in ethanolic solution stabilized by hydroxypropyl cellulose*. Journal of Materials Science Letters, 1998. **17**(24): p. 2071.
46. Gallardo, S., et al., *Photochemistry and Radiation-Chemistry of Colloidal Semiconductors 34 Properties of Q-PbS*. Berichte Der Bunsen-Gesellschaft-Physical Chemistry Chemical Physics, 1989. **93**(10): p. 1080.

47. Nozik, A.J., et al., *Size Quantization in Small Semiconductor Particles*. Journal of Physical Chemistry, 1985. **89**(3): p. 397.
48. Nenadovic, M.T., et al., *Transient Bleaching of Small PbS Colloids - Influence of Surface Properties*. Journal of Physical Chemistry, 1990. **94**(16): p. 6390.
49. Kang, I. and F.W. Wise, *Electronic structure and optical properties of PbS and PbSe quantum dots*. Journal of the Optical Society of America B-Optical Physics, 1997. **14**(7): p. 1632.
50. Konstantatos, G. and E.H. Sargent, *PbS colloidal quantum dot photoconductive photodetectors: Transport, traps, and gain*. Applied Physics Letters, 2007. **91**(17).

CHAPTER 5 – IMPACT OF SELECTIVE CONTACTS ON TRANSPORT AND STABILITY

5.1 – Introduction

The nature of transport and recombination mechanisms in heterojunction colloidal quantum dot (CQD) solar cells is not fully understood and has led to varying theories.¹⁻⁴ Many researchers have proposed the notion of “selective contact” to explain the role of oxide layers between the active material and the electrodes.⁵⁻⁹ In the absence of an efficiently depleted region, charge carriers with a long lifetime tend to diffuse in the device with a certain probability of reaching either the anode or the cathode, generating an opposite current (electron/hole annihilation) and lowering the device performances. This chapter studies the impact of TiO₂ and MoO_x as respective electrons and holes selective contacts on device properties. Typical steady-state measurements (such as incident photon-to-charge carrier efficiency and current-voltage response under illumination) have suggested the presence of a space-charge-limited current regime due to the presence of mid-gap traps. This justifies the use of 5 nm pulsed-laser assisted optoelectronic measurement techniques, which provide more information on the recombination mechanisms in these types of photovoltaic devices.

5.2 – Experimental

Various devices were assembled in a manner similar to that described in Section 3.5. A thicker TiO₂ layer was achieved by increasing the number of cycles during the spray pyrolysis deposition while MoO_x thickness was determined by

controlling the evaporation time. All the devices have a set standard 10 nm thickness of MoO_x, except if stated otherwise. Profilometry of the CQD film (Figure 5.1) shows that the surface is covered with asperities that have a high aspect ratio (~5 μm width for ~300 nm height). This type of surface roughness was reported to result from excessive ligand concentration.¹⁰ The thickness of the PbS CQD film was estimated by excluding the influence of this roughness, as the smallest distance between the electrodes will dominate the behaviour of the device. All devices had similar thicknesses.

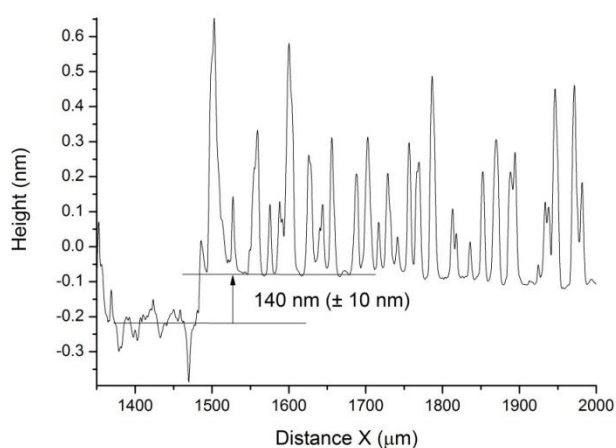


Figure 5.1 – Profilometry of the PbS CQD film on a typical device with 11 spin-coated layers.

The devices were sealed following the method describe in Section 3.5.5 in an argon filled glove box. Thus the following characterizations are considered to be as if performed in an argon environment.

5.3 – Results and discussion

5.3.1 – Steady state measurements

Figure 5.2(a) shows the incident photon-to-charge carrier efficiency (IPCE) spectrum of a device with a 135 nm TiO₂ layer. The signal is only reported to 1000 nm, as this is the limitation of the IPCE system used. The presence of a feature above 900 nm, however, clearly indicates that light is still being converted above that limit, as it is most likely related to the first exciton state.¹¹ In order to extrapolate the missing part, a Gaussian (solid green line) was fitted with the same position and full width at half maximum (FWHM) as the first exciton (1S_h-1S_e) peak from the absorption. The IPCE is then convoluted with the spectrum of the solar simulator (xenon lamp + AM1.5 filter) to obtain the spectral current density profile (Figure 5.2(b)). The area under this curve is calculated to be 11.56 mA/cm², corresponding to the short-circuit current density, J_{sc} , of the device (see equation 3.6).

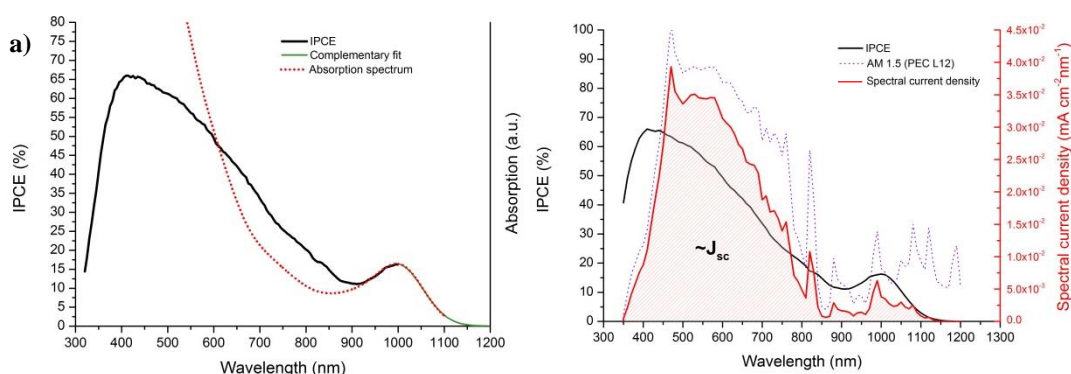


Figure 5.2 – (a) Partial IPCE spectrum (black solid curve) and complementary Gaussian fit (green solid curve) matching the first exciton peak from the absorption spectrum (dashed red curve). (b) Spectral current density (red solid curve) obtained from the convolution between the IPCE spectrum (black solid curve) and the lamp spectrum (purple dotted curve).

Figure 5.3 shows the $J - V$ curves for two samples with different TiO_2 thicknesses (performance parameters in Table 5.1). The device with the thicker TiO_2 layer shows lower current, but a higher open circuit voltage and fill factor, resulting in similar power conversion efficiencies (PCE). There is a substantial difference between the J_{SC} from Figure 5.3(a) and the one calculated from the IPCE measurements (Figure 5.2). This is believed to originate from an underestimation due to a decrease in the current during the IPCE sweep, as reported for Figure 3.12 (Section 3.3.2).

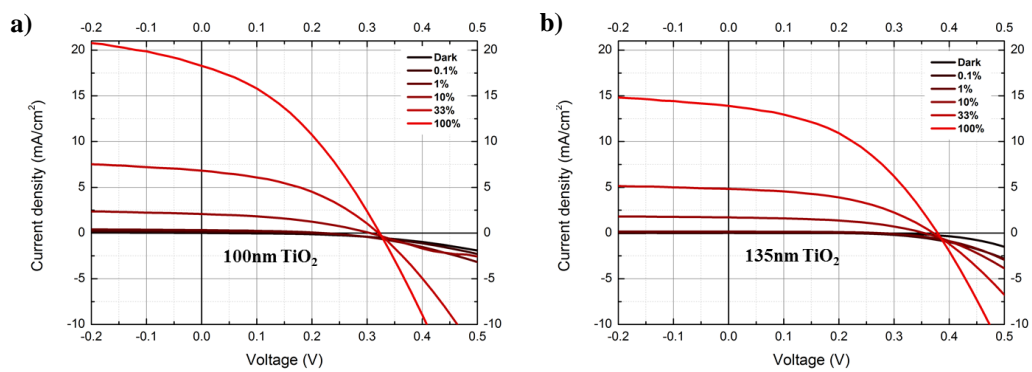


Figure 5.3 – Current density – voltage ($J - V$) curves measured at different light intensities for devices with (a) 100 nm TiO_2 and (b) 135 nm TiO_2 layer.

The dependences of J_{SC} and the open-circuit voltage V_{OC} (at 0.1 V/s) on the light intensity are plotted in Figure 5.4. The short-circuit current density experimental data were fitted with a power law $J_{SC} \propto L^a$, where L is the light intensity and the parameter a is found to be 0.92 and 0.96 for the devices with 100 nm and 135 nm TiO_2 layers, respectively (Figure 5.4(a)). Values of a below unity in polymer/fullerene based solar cells have been reported to reflect various phenomena responsible for the

recombination of charge carriers before they can be collected. They include space charge limiting effects and variation between electron and hole mobility due to unbalanced trap states, which are more likely to be correlated with a change in the thickness of the selective contact.^{12, 13}

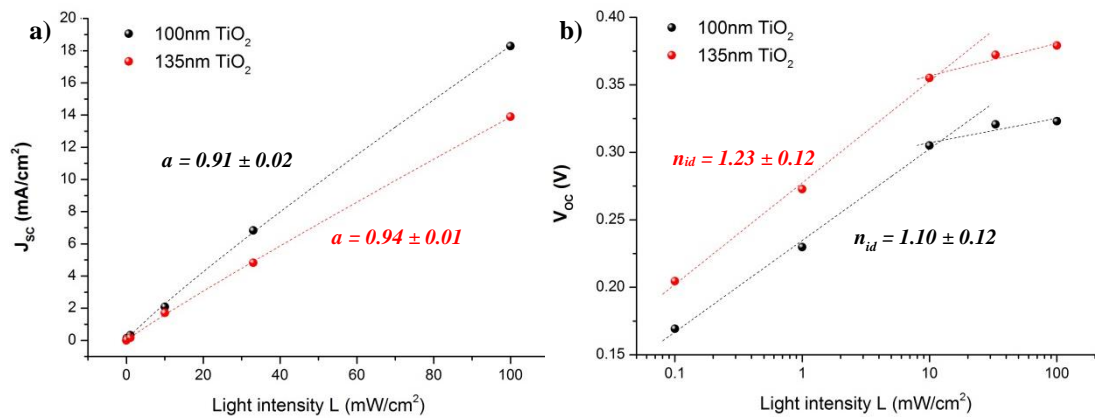


Figure 5.4 – (a) J_{sc} and (b) V_{oc} dependence on the light intensity for devices with a TiO₂ layer thickness of 100 nm and 135 nm.

Assuming that the photogenerated current is directly proportional to the light intensity, the ideality factor n_{id} can be derived from equation (2.15):

$$n_{id} = \frac{q}{k_B T} \frac{dV_{oc}}{d(\ln(L))} \quad (5.1)$$

where q is the elementary charge, k_B is the Boltzmann constant, V_{oc} is the open-circuit voltage, and L is the light intensity. In Figure 5.4(b), the dependence of V_{oc} on L reported on a log scale appears linear at low illumination ($< 10\%$), then the slope changes above 10 mW/cm^2 , reflecting a beginning of charge saturation. In this region, equation 5.1 does not hold anymore. This is why the ideality factor is calculated in the low light intensity region of the curve, resulting in n_{id} of 1.10 and 1.23 for the 100 nm

and 135 nm TiO₂ layer, respectively. This parameter gives information on the recombination regimes in the device. An ideality factor above unity indicates the presence of traps, the depth and abundance of which increase for values of n_{id} approaching 2. At first glance, a thicker TiO₂ layer increases the influence of the traps on the overall current flow, but only a marginal difference can be claimed. It can be deduced that the thickness of the TiO₂ layer in this range has a minor effect on the device performance.

Figure 5.5(a) shows the $J - V$ curves of a device without a the MoO_x selective contact when swept forward and backward. The inverted curvature (“roll over”) was previously assigned to ineffective current flow at the hole collector by Gao *et al.*²

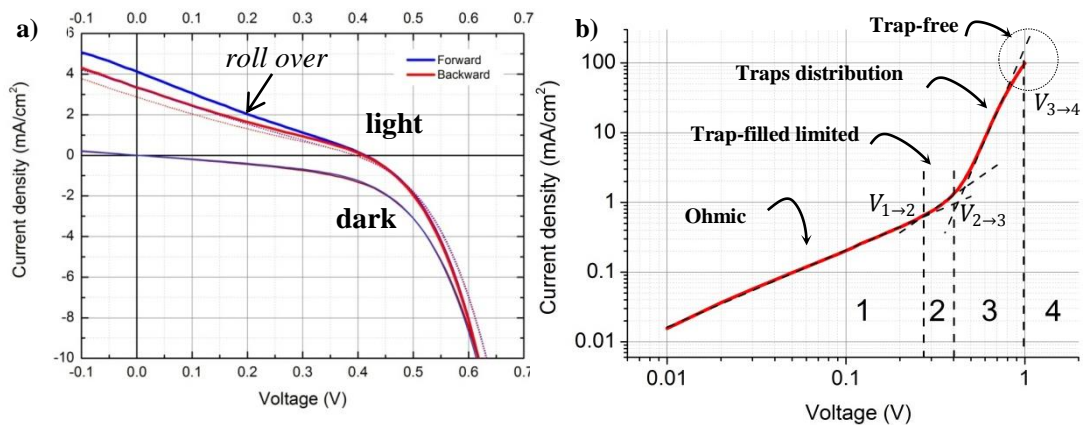


Figure 5.5 – (a) $J - V$ curves in forward (blue) and backward (red) bias voltage sweeps for a device without a MoO_x selective contact. Dotted lines correspond to a subsequent sweep. (b) log-log representation of the dark current.

In the absence of a selective barrier such as MoO_x, electrons can also be injected into the cathode creating an opposite current. The roll-over feature can be represented by fitting a two-diode equivalent circuit, with the diodes facing each other.

This sample also shows a significantly linear character, which could be due to a low shunt resistance, reflecting the presence of an alternate path for electrons. This can be caused by undesirable overlapping layers (TiO_2/Au) or pinholes occurring during the assembly process and short-circuiting one or more junctions. The ohmic behaviour of the dark current, however, followed by various conduction regimes (Figure 5.5(b)) can also be associated with the space-charge limited current (SCLC). In the context of transistors, this phenomenon arises when the depletion width is of the same order of magnitude as the physical length of the channel (Figure 5.6).^{9, 14}

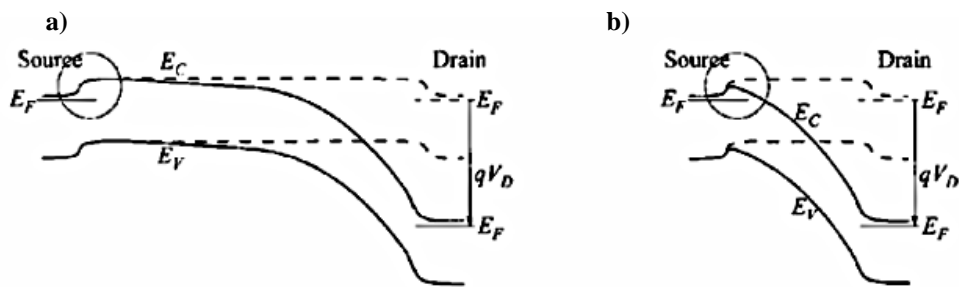


Figure 5.6 – Energy-band diagram showing a long (a) and short (b) channel, and their impact on the potential barrier (S.M. Sze, 2006).

This dark current behaviour was later proposed, however, to also arise from other atypical transport mechanisms due to asymmetrical trapping.¹⁵ Thus, local variations in the electric field at a contact also alter the local barrier height on the other side. It can be caused by:

- 1) an underestimation of the minimum *thickness* requirements of the device;
- 2) an over estimation of the *doping level*, which is inversely proportional to the depletion width (see equation (2.3));

- 3) a band-gap structure populated with discrete traps or a spectrum of trapping energy levels for one type of charge carrier.

The first issue is expected in thin film technologies. The thickness of the PbS CQD layer ($L \approx 140 \pm 10 \text{ nm}$) is thinner than what was reported in previous work ($\sim 200 \text{ nm}$),¹⁶ and additional variations in the doping level could provoke widening of the depletion region.

The first issue also can be related to the high aspect ratio of the surface roughness, where pinholes with sizes below the profilometer detection limit could create small localized shorter channels ($< 140 \text{ nm}$), short-circuiting the rest of the junction. Nevertheless, trap-assisted transport in such devices has previously been addressed,^{3, 17-19} and the SCLC model provides relevant information on the trap distribution.

Figure 5.5(b) identifies four distinct regions on the dark current $J - V$ curve. Assuming that hole quasi-Fermi level, E_{FP} , initially lies above the energy level of the traps (negligible doping), the current-voltage response is ohmic (region 1) up to $V_{1 \rightarrow 2}$ ($\sim 0.27 \text{ V}$). Below $V_{1 \rightarrow 2}$, thermally generated carriers dominate the injected carrier density ($J \propto V$).

At higher bias, E_{FP} is close to the trap levels (region 2) and the $J - V$ characteristic switches from ohmic to SCL mediated by single trapping following:

$$J_{SCL} \approx \frac{9\varepsilon_0\varepsilon_r\mu V^2}{8\theta L^3} \quad (5.2)$$

where ε_0 , ε_r , θ , μ and V are the absolute and relative dielectric constants, the fraction of free versus trapped carriers, the carrier mobility, and the bias voltage, respectively. If transport was dominated by single shallow traps, these trapping states would fill up

to $V_{2 \rightarrow 3}$ (~ 0.4 V), above which, the current should undergo a steep jump into a trap-free conduction regime (region 4). An additional regime (region 3) is observed, however, following a $J \propto V^6$ dependence, which extends over a significant bias voltage range ($V_{3 \rightarrow 4} - V_{2 \rightarrow 3} \approx 0.6$ V), suggesting the presence of exponentially distributed trap states close to the valence band edge.²⁰ Using $\theta \approx 0.08$ from Kim et al.²¹ as an approximation, a mobility μ of $(1.3 \pm 0.2) \times 10^{-5} \text{ cm}^2 \cdot \text{V}^{-1} \cdot \text{s}^{-1}$ is obtained from equation (5.2).

Subsequent voltage sweeps (dotted lines in Figure 5.5) show a significant decrease in J_{SC} (-14%) which is attributed to a certain form of degradation, despite effective sealing from atmosphere.

Figure 5.7 shows the $J - V$ curves of devices with evaporated MoO_x contacts in forward (blue) and backward (red) bias sweeps (performances reported in Table 5.1).

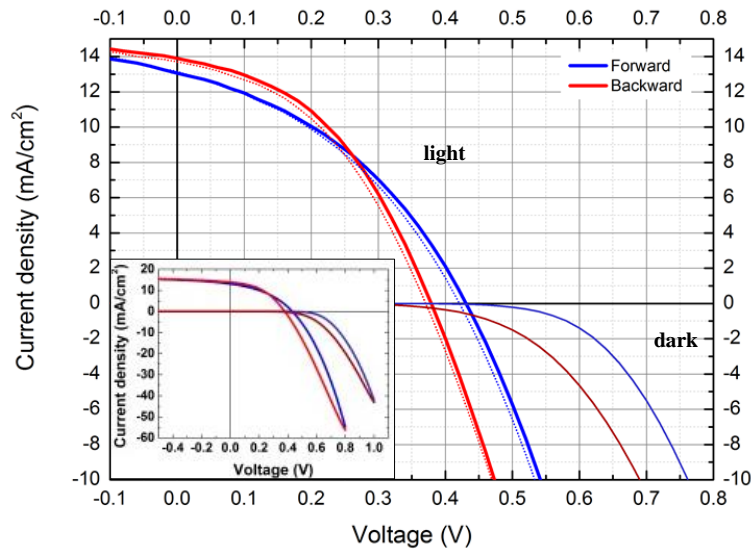


Figure 5.7 – Current-voltage curves measured with MoO_x (10 nm) selective contact. The dotted lines represent the scans in forward (blue) and backward (red) bias sweeps, and the solid lines are the computed averages. Thinner lines are the sweeps immediately following the scan.

The two devices show significantly different features. The current and fill factor are significantly higher when MoO_x is present (Table 5.2). These higher performances were previously reported to be assigned to efficient electron screening at the selective contact.^{22,23} Despite a significant mismatch between their valence band edges, holes from the PbS CQDs can be injected into MoO_x gap states caused by oxygen vacancies. Moreover, the MoO_x interface tends to be easily reduced, inducing a considerable band bending at the interface (Figure 5.8). The dipole moment induced by this electron transfer from the CQDs layer into the oxide which can be approximated by:

$$\delta_{PbS-MoO_x} \sim \Phi_{MoO_x} - IE_{PbS} = 6.9 \text{ eV} - 5.12 \text{ eV} = 1.78 \text{ eV} \quad (5.1)$$

with Φ_{MoO_x} and IE_{PbS} the work function of MoO_x²⁴ and the ionisation energy of the PbS CQDs layer²³, respectively. By modifying the surface potential of the substrate, such an oxide forms a junction that efficiently converts a hole current into an electron current.

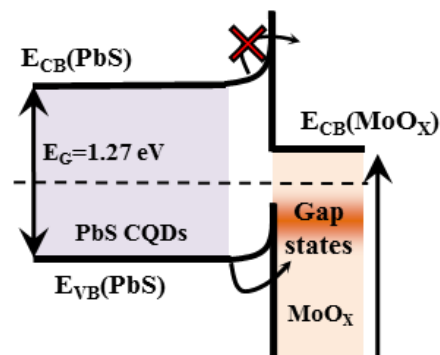


Figure 5.8 – Energy band alignment between PbS CQDs and MoO_x

The device with the MoO_x selective contact displays a strong hysteretic character both in the dark and under illumination. The sweep rate was optimized²⁵ in order to reduce this effect. Shang *et al.* reported that this phenomenon can also be associated with the retention properties of trapped carriers.²⁰ To investigate this effect, further measurements using broader and slower voltage sweeps at various temperatures are required in order to identify potential switching behaviour (low resistive state vs. high resistive state).

Table 5.1 – Performance table for devices with different selective TiO₂ contact thicknesses.

TiO ₂ thickness	MoO _x thickness	J _{sc} (mA/cm ²)	V _{oc} (V)	FF	PCE%
100nm	10nm	18.1	0.34	0.36	2.2
135nm	10nm	13.5	0.40	0.41	2.2
135nm	0nm	3.7	0.41	0.24	0.37

Further measurements showed repeatable results (dotted curves on Figure 5.7) with less than 1% variation. This suggests that the MoO_x layer also protects the device from degradation.

In order to identify how degradation affects the CQDs, films with and without MoO_x (without gold or sealing) were studied through photospectroscopy (Figure 5.9).

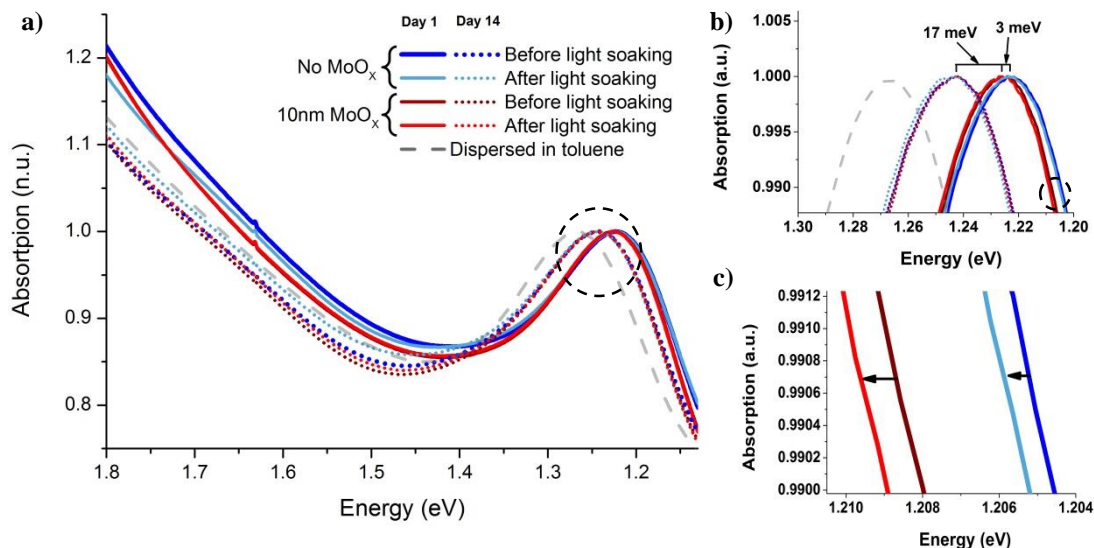


Figure 5.9 – (a) Absorption spectroscopy of PbS CQD films with (red) and without (blue) MoO_x layer. (b) and (c) Higher resolution spectra.

As previously mentioned in Chapter 4, the red shift compared to that of the CQDs suspended in toluene originates from the interparticle spacing which significantly decreases after drying on a surface and having the ligands exchanged. The sample without the MoO_x is red shifted (~3 meV) when compared to the other sample (Figure 5.9(b)). Illuminating the samples under full sun (AM1.5) provoked in both samples a small but consistent blue shift (< 1 meV), which could be due to minor surface oxidation (Figure 5.9(c)). Nevertheless, both samples behaved similarly. After repeating this set of measurements after storing the samples in ambient atmosphere for 14 days, a ~15-20 meV blue shift is observed (Figure 5.9(a)), and the curves are superimposed. Because no significant differences were observed between both samples, thus the three following options are proposed:

- the degradation does not affect the CQD crystal, suggesting that the ligands might be ones undergoing a structural change;

- the degradation appears during gold evaporation and MoO_x protects the top layer from thermally activated phenomena;
- the degradation requires electrical current to be triggered.

5.3.2 – Time-resolved optoelectronic measurements

To further investigate the charge recombination behaviour of these devices, time resolved optoelectronic techniques were used. The laser wavelength (532 nm) falls into a region where the optical density of the device is nearly unity (Figure 5.10).

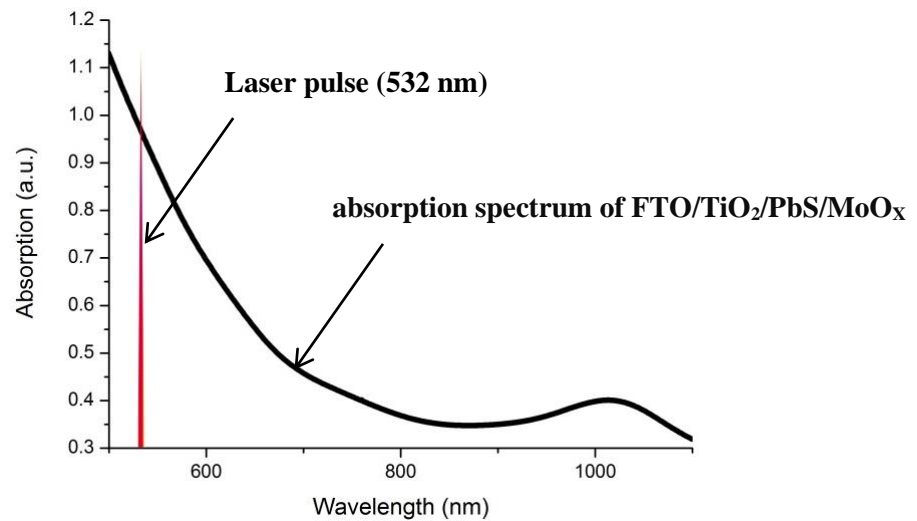


Figure 5.10 – Optical absorbance of the control PbS CQD device. A red vertical line representing the laser pulse is also shown.

Figure 5.11(a) shows the charge extraction by linearly increasing the voltage (CELIV) measurements on the control device (135 nm TiO₂ and 10 nm MoO_x). The capacitance (13.3 nF) is calculated as:

$$C = \frac{U_0}{RA} = S \frac{j_0}{A} \quad (5.3)$$

Where R is the oscilloscope impedance, S is the device area, U_0 and j_0 are differentiated RC-circuit voltage and current density step, respectively and A is the ramp rate (see Section 3.3.3.4). Calculating the relative dielectric constant from this result gives $\epsilon_r = 17.6 \pm 0.2$ (using the thickness measured from the stylus profilometer), which is in agreement with a previous report.²⁶

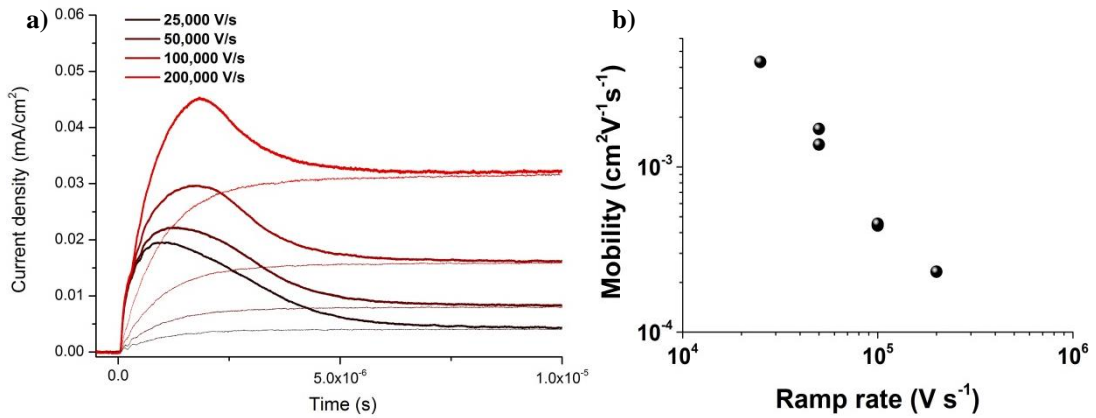


Figure 5.11 – (a) CELIV and photo-CELIV measurements for a standard device with 135 nm TiO₂ and 10 nm MoO_x. (b) Mobility dependence on the ramp rate.

There is no evidence of extracted charges in the dark from the CELIV measurements, which indicates a negligible doping level inside the active area. This result is in contradiction with previous published materials stating that there is a distinctly *p*-type doped CQD films following ligand exchange.^{16, 27} Nevertheless, this result can result from an ineffective passivation treatment, explain the lower values of V_{OC} and reinforce the hypothesis of space-charge limiting conditions (Section 5.3.1.). Further capacitance-voltage response measurements are necessary to ascertain the doping level in detail.

Charge mobility, μ , was calculated for each ramp rate (Figure 5.11(b)) following:²⁸

$$\text{(intermediate conductivity)} \quad \mu = \frac{2d^2}{3At_{max}^2 \left[1 + 0.36 \frac{\Delta j}{j_0} \right]} \quad (5.4)$$

where d is the thickness of the active layer, and t_{max} and Δj are the characteristic extraction time and the conductivity current density, respectively. This gives a lower limit estimation of the carrier mobility of $4.3 \cdot 10^{-3} \text{ cm}^2 \text{V}^{-1} \text{s}^{-1}$. The strong dependence of the apparent mobility on the ramp rate, however, suggests that the mobility range of this device is actually beyond the range of this technique in its present setup conditions.

Figure 5.12(a) shows the time-resolved charge extraction (TRCE) data for the 135 nm TiO_2 and 10 nm MoO_x device plotted on a log-linear scale. If the recombination of the charge carriers were described by a pure monomolecular model, it would follow a first order reaction rate law²⁹:

$$n(t) = n_0 e^{-kt}, \quad t_{1/2} = \ln(2)/k \quad (5.5)$$

where, $n(t)$ and n_0 are the time-dependent and initial photogenerated charge density, respectively, k is the recombination rate constant, and $t_{1/2}$ is the half-life ($n(t_{1/2}) = n_0/2$). First order recombination models describe mechanisms such as:

- Geminate recombination, where excited electrons are back transferred before proper charge separation has occurred;
- Shockley-Read-Hall recombination, in which an electron and a hole recombine following mutual capture in a trap state or a recombination centre;
- Significant charge carrier concentration gradient, enabling mobile holes to recombine in the presence of excess electrons.

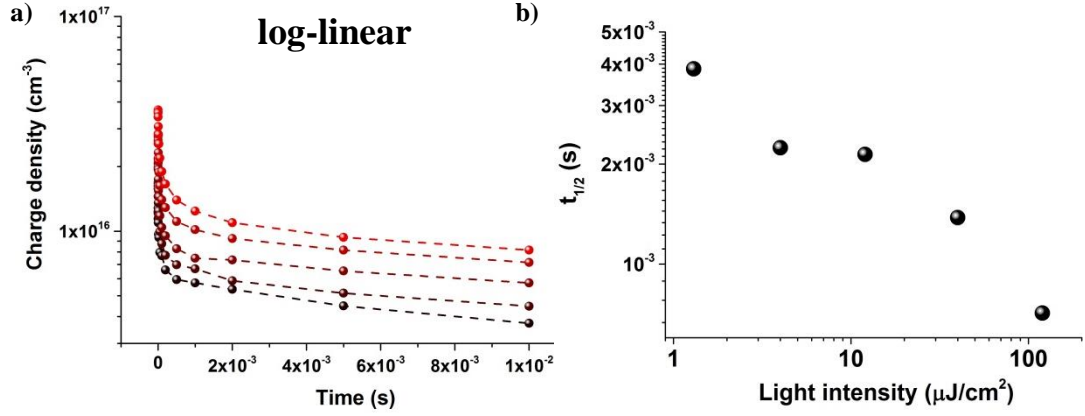


Figure 5.12 – (a) Time-resolved charge extraction (TRCE) plot of device on a log-linear scale. (b) Half-life dependence on the light intensity.

The absence of linearity in Figure 5.12(a) suggests that the decay is not monoexponential. Moreover, the half-life dependence on the light intensity (Figure 5.12(b)) shows a consistent decrease, while first-order reaction $t_{1/2}$ would be expected to be constant as suggested by equation (5.5). Therefore, the monomolecular recombination model can be discounted as a dominant mechanism for such a system.

Figure 5.13 shows the same data plotted on a log-log scale. The decaying pattern appears to be divided into two regions, where the fastest phase ($< 3 \times 10^{-6}$ s) shows a slower decay. The second phase matches with a power law:

$$n \propto t^{-\alpha} \quad (5.6)$$

with $\alpha = 0.15 \pm 0.02$. α was reported to describe the energetic distribution of polaron (quasi-particle representing a charge moving in a highly polarizable lattice) localised states in polymer based photovoltaic devices.³⁰ Polarons can form in weakly confined quantum dots, arising from the strong coupling between the electrons and the longitudinal-optical (LO)-phonons, leading to entangled wavefunctions between

discrete electronic states and different phonon occupancies.³¹⁻³³ A power approaching unity reflects a dominant second-order reaction describing bimolecular recombination mechanisms. Smaller values are attributed to the presence of traps requiring thermal activation for recombination to occur (smaller α , deeper traps). Because first and second order decays do not optimally match the experimental data, the reaction might be better described by a higher order. This was previously reported as possibly originating from highly dispersive bimolecular decay dynamics, attributed to an exponential tail of sub-band-gap localized trap states.^{34, 35}

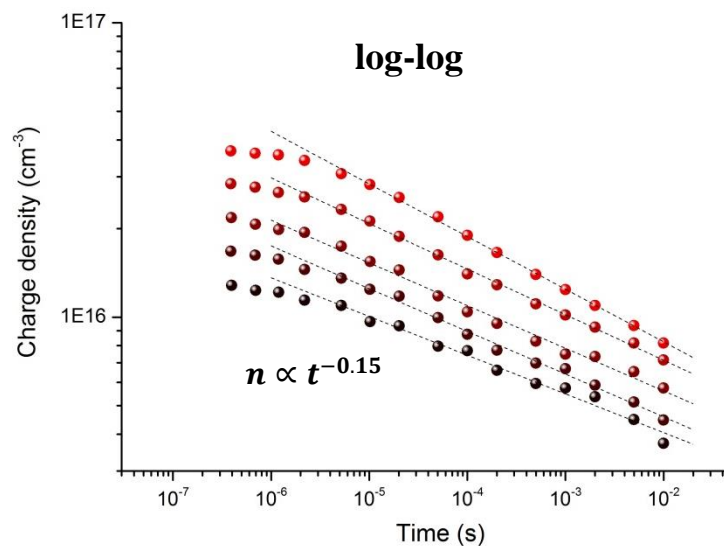


Figure 5.13 – TRCE plot of 135 nm TiO₂/10 nm MoO_x device on a log-log scale.

Figure 5.14 shows the TRCE data for devices with 10 nm, 5 nm, and 0 nm MoO_x layers. The curves can be fitted with a power law in the first phase which is followed by a significant accelerated decay for the samples with 5 nm and no MoO_x. The trend suggests that the carrier lifetime increases with increasing the thickness of

the selective contact, possibly by shielding recombination with charges from the external circuit.

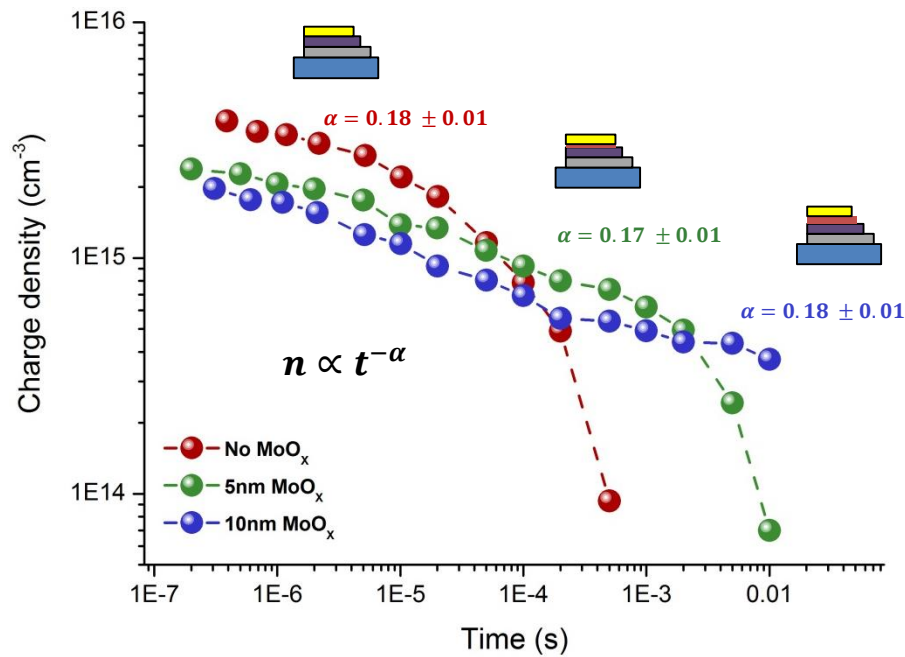


Figure 5.14 – TRCE plot for devices without MoO_x (red), and with 10 nm (green) and 20 nm (blue) MoO_x layers at 16 μJ/cm².

α is similar for each curve, but a consistent shift towards lower charge densities with increasing thickness the MoO_x layer can also be observed. Nothing is assumed to change the initial photogenerated carrier density in the CQD film. The differences between each samples at $t < 10^{-5}$ s are presumed to originate from small variations in the film thickness and roughness. The causes responsible for this accelerated decay are most likely related to the degradation mentioned in Section 5.3.1.

Figure 5.15(a) shows the open-circuit voltage decay (OCVD) for the devices with 5 nm and 10 nm MoO_x layers. A V_{OC} rise in both curves can be observed in the 10^{-7} - 10^{-6} s region and is believed to indicate that the charge distribution responsible

for splitting the quasi-Fermi levels at the contacts is dominated by a slow diffusion process in the sub-microsecond regime.

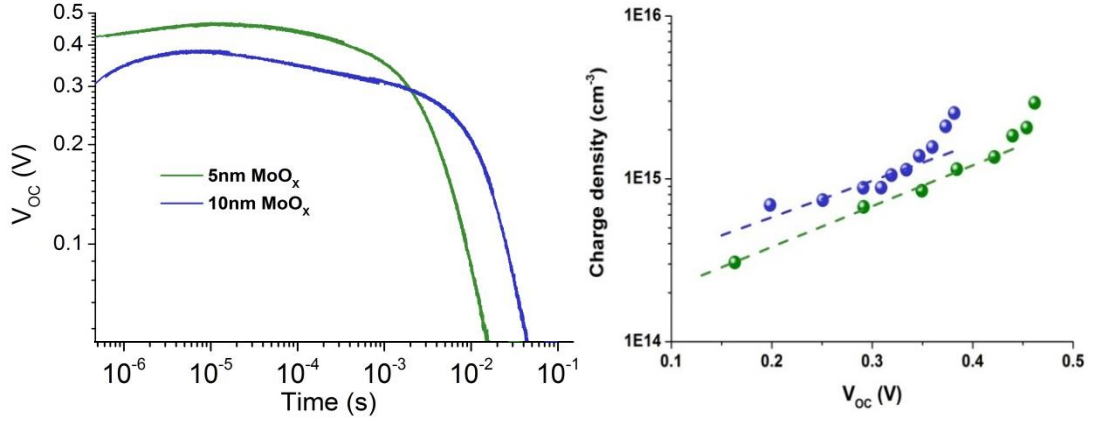


Figure 5.15 – (a) OCVD curves for devices with 5 nm and 10 nm MoO_x layers at 160 μJ/cm². (b) Photovoltage dependence on the charge density from Figure 5.12. The dashed curves represent the exponential fit.

As determined previously, the doping of the CQD layer is negligible. As such, setting the hole initial quasi-Fermi level (E_{FP}) close to the intrinsic state (see Figure 5.16), while the electron quasi-Fermi level (E_{FN}) lies close to the conduction band (pinned by the TiO₂ electrode). After the laser pulse hits the sample at t_1 , the photogenerated charge density distribution in the device follows the Beer-Lambert exponential law, setting E_{FP} closer to the valence band at the front electrode than at the back electrode (red dashed line). The first phase of the transient ($< 10^{-5}$ s) is dominated by the diffusion of the carriers which gradually adjust E_{FP} at the back electrode to be closer to the valence band (orange and yellow dashed lines) up to t_{dr} (green dashed line). The rise of V_{OC} is observable on the microsecond time scale because both diffusion and recombination processes are relatively slow in this system.

At t_{dr} , the recombination mechanisms become more significant and overtake diffusion. The loss of carriers causes V_{OC} to decay, as observed in Figure 5.15(a).

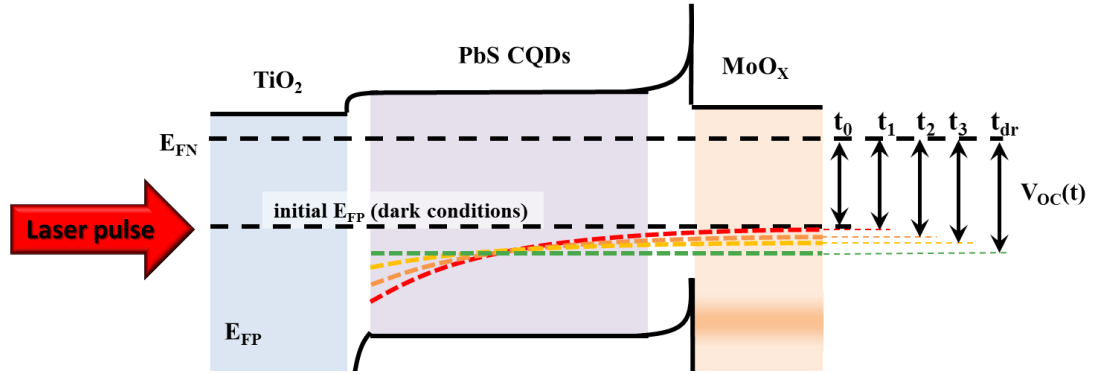


Figure 5.16 – Schematic diagram describing the slow growth of V_{OC} after illumination with a laser pulse. t_0 describes the dark equilibrium before illumination. t_1 describes the system immediately after illumination. t_2 and t_3 describes the system with gradual charge diffusion. At t_{dr} , the maximum number of charges at the rear edge of the CQD film is reached. After t_{dr} , recombination becomes significant and EFP returns gradually to its initial position (at t_0).

The sample with a thicker MoO_x layer displays a lower V_{OC} and an extended decay. These are in agreement with the results from Figure 5.14 that show a lower charge density and no notable accelerated decay. The charge density dependence on V_{OC} is plotted for both devices (Figure 5.15(b)). Because only the decaying region has a physical correspondence to the recombination mechanism, the exponential was only fitted to the lower voltages:

$$n = n_0 e^{\gamma V_{OC}} \quad (5.7)$$

with $\gamma = 5.5 \pm 0.3$. This value is relatively small compared to a typical 2nd order recombination reaction ($\gamma_{PCBM} \approx 13$),³⁰ suggesting a complex trapping/detrapping

regime. Ideally, a completely trap-free environment would lead to a pure bimolecular recombination with $\gamma_{bimol} = q/2k_B T \approx 19$.

Figure 5.17 shows the time-of-flight (TOF) measurements under a 1 V bias for the 135 nm TiO₂ and 10 nm MoO_x device (RC circuit time constant, $\tau_{RC} \approx 130 \mu s$). A 10 k Ω impedance was used to investigate if the saturation regime could be reached in order to obtain the extraction time. No saturation was observed, however, even when using the highest available light intensity. This is due to the strongly dispersive transport character of the material.³⁶

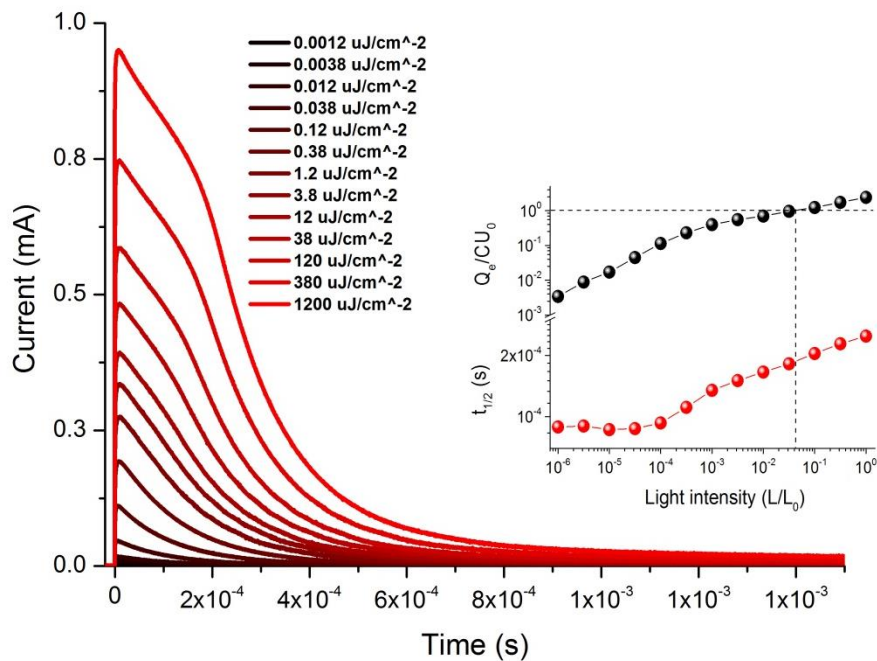


Figure 5.17 – Time-of-flight measurements. The inset shows the extracted charge (black) and half-life (red) dependence on the light intensity. The dashed lines indicate the limit after which the amount of extracted charges exceeds the capacitive charges stored at the contacts.

The inset in Figure 5.17 shows the evolution of the half decay time and the normalized extracted charges with the capacitive charges. A first recombination

regime is observed where $t_{1/2}$ is independent of the light intensity, indicating that the photogenerated charge carriers recombine within the transit time. This is followed by a monotonic increase, thus excluding the possibility of a Langevin-type bimolecular recombination.

In non-Langevin bimolecular recombination, typically, the half-life is constant until the extracted charge equals the capacitive charge. It then increases up to a saturation regime where charge extraction becomes limited by the circuit resistance,³⁷ after which, both parameters are completely independent of the light intensity. The inset shows no signs of a plateau either in the half decay time or in the extracted charge dependence on the light intensity, suggesting that the conditions were not appropriate to push the system up to its saturation regime. It should be noted that $t_{1/2}$ is of the same order of magnitude as the RC time constant ($\sim 10^{-4}$ s) and relatively longer than typical values from other organic solar cells, which might explain why the saturation regime could not be observed. Increasing the circuit impedance R (e.g. 1 M Ω) would typically reduce the extraction time and should reveal the saturation regime.

Figure 5.18 shows the normalized transient photovoltage measurement (TPV) for the 135 nm TiO₂ and 10 nm MoO_x device at various light intensities, each associated with an open-circuit voltage (see legend). The irregularities in the curves at longer time are due to fast decay in the background voltage.

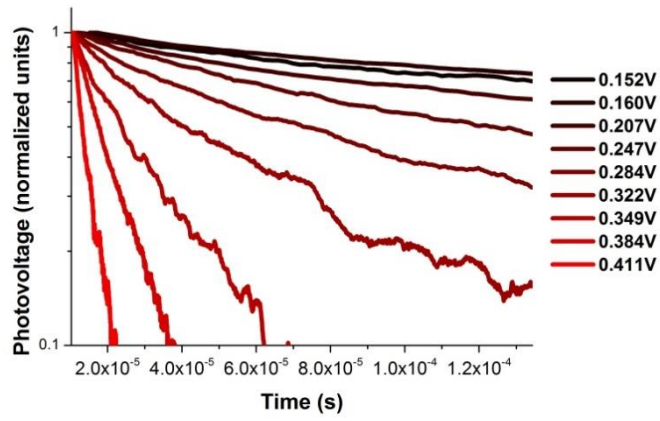


Figure 5.18 – Transient photovoltage measurement under various V_{OC} conditions.

The decays could not be fitted with a monoexponential for the 0.152-0.349 V range. The main “slow” decay component appears to be preceded by a faster one which is dominant at low V_{OC} (see Figure 5.19).

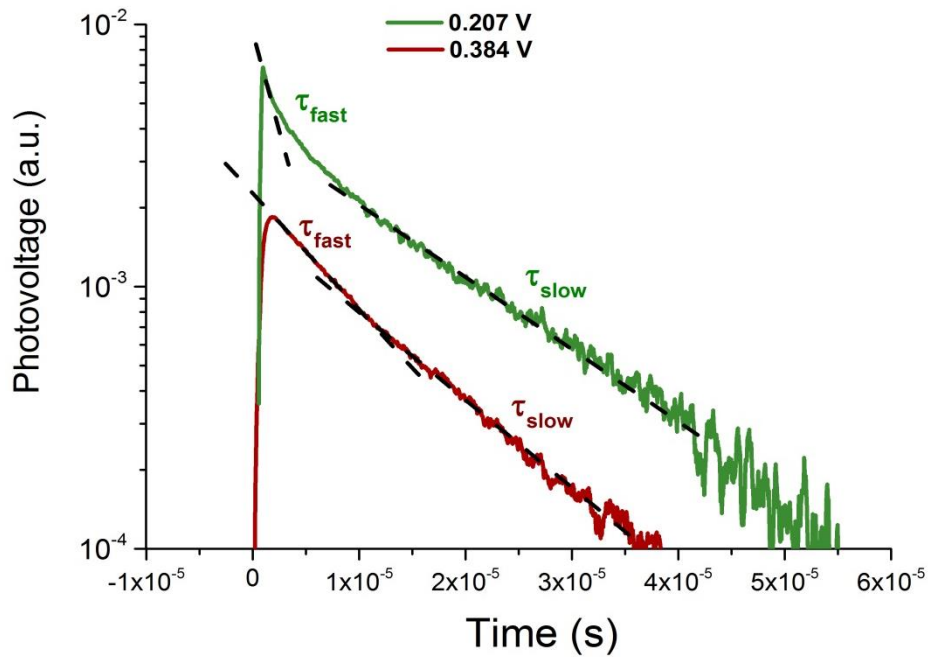


Figure 5.19 – Transient photovoltage measurement ($< 100 \mu\text{s}$) for $V_{OC} = 0.207$ and 0.384 V.

In TPV, the steady state condition is under full light with the traps limiting the diffusion already filled. It is then believed that Equation (5.7) used at lower voltage can be used to replace the photovoltage by the carrier density. The curves can be then fitted with a stretched exponential with the following form:

$$\Delta n = \Delta n_0 e^{-(t/\tau_0)^\delta} \quad (5.8)$$

where Δn and Δn_0 are the time dependent and initial excess carriers densities generated following the weak optical perturbation, respectively. τ_0 and δ are the stretched exponential lifetime and power fitting parameters, respectively. The quality of fit was assessed by considering the reduced chi-square value (χ^2) and the randomness of the weighted residuals. The observed lifetime, τ_{obs} , can be obtained by calculating the mean value through its Gamma distribution, $\Gamma(x)$, following:

$$\tau_{obs} = \frac{\tau_0}{\delta} \Gamma\left(\frac{1}{\delta}\right) \quad (5.9)$$

Stretched exponentials typically reflect dispersive relaxation mechanisms in disordered systems³⁸ where δ is related to the distribution order. Indeed, at $\delta = 1$, the function returns to a monoexponential form, and $\tau_{obs} = \tau_0$. In the present system, it can be observed that δ rises from 0.33 to 0.78 as the open-circuit voltage is increased (Figure 5.20(a)), suggesting the gradual disappearance of the dispersive character to leave a quasi-monoexponential decay. This can be interpreted as a recombination regime where deep traps are gradually filled as the V_{OC} increases,

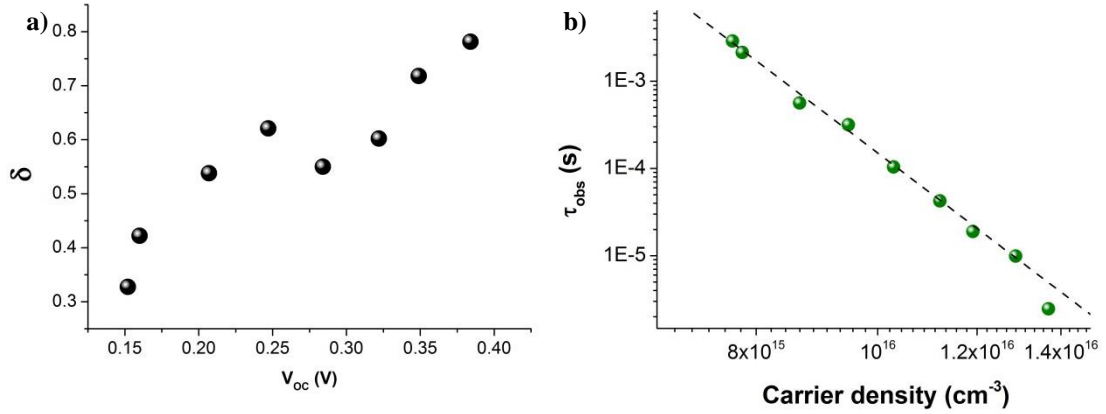


Figure 5.20 – (a) Dependence of stretched exponential power fitting parameter δ on V_{OC} . (b) Observed lifetime, τ_{obs} , dependence on the carrier density.

This phenomenon appears to be related to the deep traps distribution mentioned earlier. At low photogenerated charge carrier density ($V_{OC} \approx 0.15$ V), several mid-gap traps are still vacant, leaving a wide range of recombination pathways that are well represented by a stretched exponential. As the traps are gradually filled up, the remaining charges see their mobility increased, and diffusion limited recombination mechanisms become dominant, which are better represented by a single exponential decay. This strengthens the hypothesis of a SCLC regime as mentioned earlier.

In Figure 5.20(b), the observed transient lifetime is plotted against the carrier density on a log-log scale. Experimental data were fitted with a power law:

$$\tau_{obs} = \tau_{obs,0}(n_0/n)^\lambda$$

where the power λ was calculated to be 10.9. This value is extremely high when compared to what is reported for fullerene^{4,34,39} and polymer solar cells.⁴⁰ This can be

expected as the stretched exponential fittings exclude the typical bimolecular recombination process from being dominant.

5.4 – Conclusion

This chapter gathers introductory measurements describing transport mechanisms in PbS QCD solar cells. Thicker TiO₂ selective contact showed a higher open-circuit voltage and fill-factor, at the expense of a lower short-circuit current and resulting in very similar power conversion efficiencies. The dependence of J_{sc} and V_{oc} on light intensity suggest that thinner TiO₂ result in stronger space-charge limiting effects and less recombination through interfacial trapping levels. A qualitative study of the space-charge-limited current raised the hypothesis of an exponential distribution of shallow to medium trap energy levels in the vicinity of the valence band edge. The sample with the MoO_x selective contact layer showed improved performance. The higher fill factor is expected to originate from the sealing of potential pinholes that cause local short circuits, and from the electron barrier arising from the strong dipole that forms at the interface between the PbS CQD layer and the MoO_x, while allowing holes through the mid-gap states. The appearance of a hysteresis in the $J - V$ curve suggests an increase in the retention properties of the interfacial traps. The high short-circuit current is attributed to improved device stability. Because absorption spectroscopy could not pinpoint any differences between films with and without a MoO_x layer, before and after light illumination, the hypothesis of degradation through air exposure or through photoactivated mechanisms can be rejected.

Transient techniques were used to probe time-dependant recombination mechanisms. Using CELIV without illumination, no charges were extracted, suggesting a negligible doping level in the PbS layer. This measurement is in strong agreement with the SCLC model used previously, as it is responsible for broadening the depletion region and pinning the hole quasi-Fermi level above the trap states. The relatively slow decay curve obtained from time-resolved charge extraction could be fitted with neither a typical first- nor second-order process (monomolecular), suggesting complex sub-band-gap trapping. Accelerated decays were observed as the thickness of the MoO_x layer was reduced and a higher probability was assigned for recombination with charges originating from the external circuit. The presence of a delayed maximum on the V_{OC} decay measurement was attributed to the slow charge carrier diffusion mechanism dominating recombination before $t_{max} \approx 10^{-5}$ s. Time-of-flight measurements confirm the absence of Langevin-type recombination, but could not identify any other mechanisms, as saturation was not observed. Transient photovoltage measurements could be fitted with a stretched exponential with a V_{OC} dependent stretch factor, suggesting that the recombination mechanisms are sensitive to the trap vacancy level.

References

1. Lee, J.-S., et al., *Band-like transport, high electron mobility and high photoconductivity in all-inorganic nanocrystal arrays*. Nature Nanotechnology, 2011. **6**(6): p. 348.
2. Gao, J.B., et al., *Quantum Dot Size Dependent J-V Characteristics in Heterojunction ZnO/PbS Quantum Dot Solar Cells*. Nano Letters, 2011. **11**(3): p. 1002.
3. Nagpal, P. and V.I. Klimov, *Role of mid-gap states in charge transport and photoconductivity in semiconductor nanocrystal films*. Nature Communications, 2011. **2**: p. 486.
4. Ryan, J.W., et al., *Nongeminate Recombination Dynamics–Device Voltage Relationship in Hybrid PbS Quantum Dot/C60 Solar Cells*. The Journal of Physical Chemistry C, 2013. **117**(34): p. 17470.
5. Mora-Sero, I., et al., *Selective contacts drive charge extraction in quantum dot solids via asymmetry in carrier transfer kinetics*. Nature Communications, 2013. **4**.
6. Ehrler, B., et al., *Preventing interfacial recombination in colloidal quantum dot solar cells by doping the metal oxide*. ACS Nano, 2013. **7**(5): p. 4210.
7. Willis, S.M., et al., *The transitional heterojunction behavior of PbS/ZnO colloidal quantum dot solar cells*. Nano Letters, 2012. **12**(3): p. 1522.
8. Adinolfi, V., et al., *Electric field engineering using quantum-size-effect-tuned heterojunctions*. Applied Physics Letters, 2013. **103**(1): p. 011106.
9. Maraghechi, P., et al., *The donor–supply electrode enhances performance in colloidal quantum dot solar cells*. ACS Nano, 2013. **7**(7): p. 6111.
10. Barkhouse, D.A.R., et al., *Thiols passivate recombination centers in colloidal quantum dots leading to enhanced photovoltaic device efficiency*. ACS Nano, 2008. **2**(11): p. 2356.
11. Tang, J., et al., *Colloidal-quantum-dot photovoltaics using atomic-ligand passivation*. Nature Materials, 2011. **10**(10): p. 765.

12. Cowan, S.R., A. Roy, and A.J. Heeger, *Recombination in polymer-fullerene bulk heterojunction solar cells*. Physical Review B, 2010. **82**(24): p. 245207.
13. Koster, L., et al., *Origin of the light intensity dependence of the short-circuit current of polymer/fullerene solar cells*. Applied Physics Letters, 2005. **87**(20): p. 203502.
14. Sze, S.M. and K.K. Ng, *Physics of Semiconductor Devices*. 2006: Wiley.
15. Kao, K.C. and C.S. Hwang, *Electrical Transport in Solids*. International series in the science of the solid state, 1981. **14**: p. 569.
16. Pattantyus-Abraham, A.G., et al., *Depleted-heterojunction colloidal quantum dot solar cells*. ACS Nano, 2010. **4**(6): p. 3374.
17. Stadler, P., et al., *Joint Mapping of Mobility and Trap Density in Colloidal Quantum Dot Solids*. ACS Nano, 2013. **7**(7): p. 5757.
18. Zhitomirsky, D., et al., *Measuring charge carrier diffusion in coupled colloidal quantum dot solids*. ACS Nano, 2013. **7**(6): p. 5282.
19. Bakulin, A.A., et al., *Charge Trapping Dynamics in PbS Colloidal Quantum Dot Photovoltaic Devices*. ACS Nano, 2013. **7**(10): p. 8771.
20. Shang, D., et al., *Effect of carrier trapping on the hysteretic current-voltage characteristics in Ag/ La 0.7 Ca 0.3 MnO 3/ Pt heterostructures*. Physical Review B, 2006. **73**(24): p. 245427.
21. Kim, J.K., et al., *Space charge limited conduction in ultrathin PbS quantum dot solid diodes*. Journal of Applied Physics, 2014. **115**(5): p. 054302.
22. Kanai, K., et al., *Electronic structure of anode interface with molybdenum oxide buffer layer*. Organic Electronics, 2010. **11**(2): p. 188.
23. Gao, J., et al., *n-type transition metal oxide as a hole extraction layer in PbS quantum dot solar cells*. Nano Letters, 2011. **11**(8): p. 3263.
24. Meyer, J., et al., *Transition Metal Oxides for Organic Electronics: Energetics, Device Physics and Applications*. Advanced Materials, 2012. **24**(40): p. 5408.

25. Herman, M., M. Jankovec, and M. Topič, *Optimal IV curve scan time of solar cells and modules in light of irradiance level*. International Journal of Photoenergy, 2012. **2012**.
26. Tang, J., et al., *Quantum Dot Photovoltaics in the Extreme Quantum Confinement Regime: The Surface-Chemical Origins of Exceptional Air- and Light-Stability*. ACS Nano, 2010. **4**(2): p. 869.
27. Johnston, K.W., et al., *Efficient Schottky-quantum-dot photovoltaics: The roles of depletion, drift, and diffusion*. Applied Physics Letters, 2008. **92**(12): p. 122111.
28. Juska, G., et al., *Hole drift mobility in $\mu\text{c-Si}$: H*. Journal of Applied Physics, 2001. **89**(9): p. 4971.
29. Shoaee, S., et al., *Influence of nanoscale phase separation on geminate versus bimolecular recombination in P3HT: fullerene blend films*. Energy & Environmental Science, 2010. **3**(7): p. 971.
30. Clarke, T.M., et al., *Photodegradation in Encapsulated Silole- Based Polymer: PCBM Solar Cells Investigated using Transient Absorption Spectroscopy and Charge Extraction Measurements*. Advanced Energy Materials, 2013. **3**(11): p. 1473.
31. Inoshita, T. and H. Sakaki, *Density of states and phonon-induced relaxation of electrons in semiconductor quantum dots*. Physical Review B, 1997. **56**(8): p. R4355.
32. Ferreira, R. and G. Bastard, *Electron-Phonon Interaction in Semiconductor Quantum Dots*, in *Semiconductor Macroatoms: Basic Physics and Quantum-device Applications*, F. Rossi, Editor. 2005, Imperial College Press: London. p. 183.
33. Verzelen, O., G. Bastard, and R. Ferreira, *Energy relaxation in quantum dots*. Physical Review B, 2002. **66**(8): p. 081308.
34. Shuttle, C., et al., *Experimental determination of the rate law for charge carrier decay in a polythiophene: Fullerene solar cell*. Applied Physics Letters, 2008. **92**(9): p. 3311.
35. Deibel, C., A. Baumann, and V. Dyakonov, *Polaron recombination in pristine and annealed bulk heterojunction solar cells*. Applied Physics Letters, 2008. **93**(16): p. 163303.

36. Kokil, A., K. Yang, and J. Kumar, *Techniques for characterization of charge carrier mobility in organic semiconductors*. Journal of Polymer Science Part B: Polymer Physics, 2012. **50**(15): p. 1130.
37. Pivrikas, A., et al., *Bimolecular recombination coefficient as a sensitive testing parameter for low-mobility solar-cell materials*. Physical Review Letters, 2005. **94**(17): p. 176806.
38. Albero, J., et al., *Photo-induced charge recombination kinetics in low bandgap PCPDTBT polymer: CdSe quantum dot bulk heterojunction solar cells*. Chemical Science, 2011. **2**(12): p. 2396.
39. Boix, P.P., et al., *Carrier recombination losses in inverted polymer: Fullerene solar cells with ZnO hole-blocking layer from transient photovoltage and impedance spectroscopy techniques*. Journal of Applied Physics, 2011. **109**(7): p. 074514.
40. Li, Z., et al., *Comparison of the operation of polymer/fullerene, polymer/polymer, and polymer/nanocrystal solar cells: a transient photocurrent and photovoltage study*. Advanced Functional Materials, 2011. **21**(8): p. 1419.

CHAPTER 6 – CONCLUSION AND FUTURE WORK

In this work, various aspects of novel PbS CQD based solar cells were investigated. The study of the particle surface state allowed the identification of different passivation pathways characteristic to specific ligand treatments leading to different optical responses. FTIR and XPS analysis were used to investigate the various elemental species composition on films treated with different passivating agents. A strong decrease in aliphatic carbon groups was observed after simply treating the films with methanol, suggesting that this solvent by itself dissolve a significant portion of the inherent oleic acid ligand. The presence of lead oxide/hydroxide was detected on the untreated sample suggesting that the nanoparticle might oxidize during the synthesis process. Even if oleate groups are bound to lead atoms, higher contents of oxidized sulfur compounds were observed on samples where oleic acid was removed/replaced. A weakly oxidized specie (-SO, -SO₂ or -SOH) was detected on both S 2p and O 1s spectra and was found to be significantly sensitive to air exposure, especially on the sample rinsed with methanol only.

The removal of oleic acid ligand following methanol rinsing leaves the CQD film relatively vulnerable to ambient adventitious oxidation. This was confirmed by a significant blue shift of the first $\langle 1S_h \rangle \rightarrow \langle 1S_e \rangle$ exciton absorption peak. From this energy difference, the particle radius reduction was calculated to be in the order of 1-2 Å and was attributed to the oxidation of a single atomic monolayer. The absorption peak broadening also suggests that the oxidation is non-uniform through the thickness of the film. On the other hand, all ligand exchange treatments led to a notable red shift

that was assumed to be directly related to electron wavefunction delocalization due to a smaller interparticle spacing. A significant Stokes shift was observed between the first exciton peak and the two photoluminescence peaks which were attributed to a shallow and deep in-gap energy levels, respectively. The strong photoluminescent quenching indicates an efficient electron injection from the CQD film to TiO₂ particles. Nevertheless, the non-uniform quenching among the two emission peaks was attributed to the recapture of approximately 1% of the injected charges into the deeper in-gap state of the QDs. Compared to the samples treated with MPA and TGA, the TLA treatment showed the best protection against adventitious surface oxidation) and the least electronic reconfiguration while maintaining similar electron injection in TiO₂.

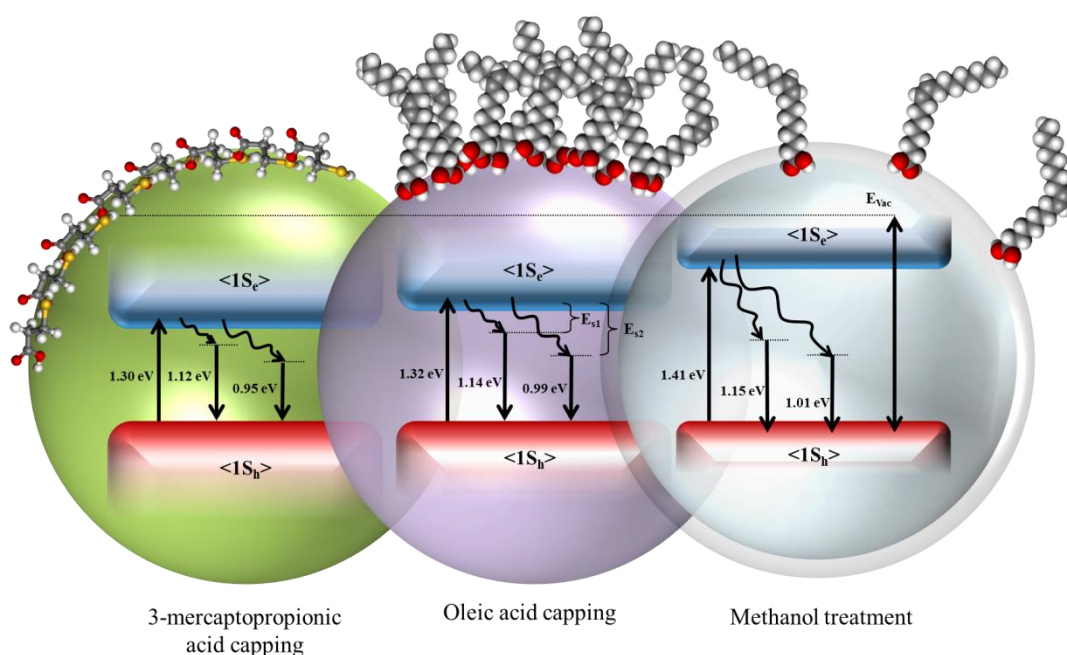


Figure 6.1 – Illustration of three QDs differently passivated, the short and long molecules representing 3-mercaptopropionic acid and oleic acid, respectively. The QD treated with methanol shows a significant proportion of ligands removed, as well as thin oxidized shell.

Various factors appear to influence the response of PbS CQD film photovoltaic devices. Increasing the thickness of the TiO₂ selective contact led to an increase of the

open-circuit voltage and the fill factor at the expense of a lower short-circuit current density. A space-charge limited current model appears to match with the current-voltage response and suggest a whole distribution of in-gap energy levels which must be overcome before reaching a trap-free regime. Both TiO₂ and MoO_x selective contacts have a significant impact on the space-charge limiting effect. Moreover, significant increase in J_{SC} and fill factor confirmed that the MoO_x acts as a barrier to electrons, thus preventing back current while allowing hole to travel through in-gap states. It is also expected to seal potential pin-holes connecting TiO₂ to gold, which creates local short circuits. On the other, MoO_x selective contact increased the hysteretic character of the current voltage response, indicating the presence of strong retention of trapped carriers.

The enhanced stability of samples coated with MoO_x could not be addressed through absorption spectroscopy. The absence of extracted free charge carrier through linearly increased voltage indicates that the doping level in the active layer is negligible. This results might be responsible for widening the depleted region at the PbS/TiO₂ interface and participate to the space-charge limited current. Both time-resolved charge extraction and photovoltage decay measurements suggest that the recombination mechanism is first dominated by a very slow process until t_{dr} . During that time, carriers diffuse slowly in the device. Past that time, the recombination rate undergoes a significant acceleration and both charge density and photovoltage drop. t_{dr} appears to have a notable dependence on the MoO_x thickness, suggesting that charges recombining with the external circuit could be at least one of the cause for this precipitated decay. Despite the fact that this type of device has a lot of similarities with organic solar cells because of the trap assisted charge transport, neither first-order (monomolecular) nor Langevin-second-order reaction could be used to describe the

recombination behaviour. Other types of second-order reaction rate could not be completely rejected, however, such long characteristic times might be the signature of complex pathways involving multiple steps, as suggested by the good fit provided by the stretched exponential function of the transient photovoltage decay.

This work elucidated certain mechanisms and proposed different interpretations regarding various processes. XPS analysis of the surface composition on various levels, in particular oxygen and carbon reveal a lot of information regarding the presence of organic ligands such as the coverage proportion and the type of passivation bond. Deeper analysis would involve a better protection of the sample from adventitious contamination and angle (or beam energy) resolved analysis in order to distinguish the surface contributions from the ones originating inside the QDs. This technique would also provide information on the role of intermediate ligand such as oleylamine or octylamine. Optical spectroscopy such as UV-Vis-NIR absorption and photoluminescence gave rather accurate indication on how the CQD film responds under optical excitation. To the best of our knowledge, such distinct in-gap trap states were not reported before. Further measurements using an integrating sphere to quantify the fluorescence yield and time resolved detectors sensitive to NIR photons to ascertain the differences of each states decay would provide the necessary information to provide details on the excited quasi-particle identity (dark/bright exciton or polaron).

PbS CQD stability is a matter requiring dedicated study. The current work proposed that photodegradation of the ligands, thermal evaporation and electric activation are possible pathways responsible for lowering the performance of the device. A full space-charge limited model needs to be fitted on a various range of devices with different CQD and selective contact thicknesses over broader voltage

bias range in order to identify the different regime. Moreover, trapped charge retention can definitely be addressed and explained using these models. Finally, transient optoelectronic measurement showed atypical and promising results. In order to extract crucial information, the conditions of the set-up will require to be adjusted in order to reach the carrier density saturation. In this regime, parameters such as the transit time can be measured and the mobility calculated. Further devices with various interparticle spacing must be analysed to attribute the contribution of such parameters on the charge transport properties. The TLA ligand, which showed better stability and appeared to be less affected by the exciton wavefunction overlap, needs to be further investigated and implemented in a proper device. Finally, further optimization on the CQDs synthesis is required in order to produce defect-free material.

PUBLICATIONS DURING PHD

- 1) '*The Effect of Surface Passivation on the Structure of Sulphur-Rich PbS Colloidal Quantum Dots for Photovoltaic Application*', **Victor Malgras**, Andrew Nattestad, Jung Ho Kim, Shi Xue Dou, [*under preparation*];

- 2) '*Recombination Mechanisms in PbS Colloidal Quantum Dots Heterojunction Solar Cells*', **Victor Malgras**, Guanran Zhang, Attila Mozer, Jung Ho Kim, Shi Xue Dou, [*under preparation*];

- 3) '*Mesoporous Pt Hollow Cubes with Controlled Shell Thicknesses and Investigation of Their Electrocatalytic Performance*', Cuiling Li, Bo Jiang, Masataka Imura, **Victor Malgras**, and Yusuke Yamauchi, **Chemical Communication** [submitted on 08/09/2014];

- 4) '*Large-Scale Synthesis of Coaxial Carbon Nanotube/Ni(OH)₂ Composites for Asymmetric Supercapacitor Application*', Rahul R. Salunkhe, Jianjian Lin, **Victor Malgras**, Shi Xue Dou, Jung Ho Kim, Yusuke Yamauchi, **Nano Energy** [submitted on 28/07/2014];

- 5) '*Channelled Porous TiO₂ Synthesized with a Water-in-Oil Microemulsion*', **Victor Malgras**, Priyanka Jood, Ziqi Sun, Jung Ho Kim, Shi Xue Dou, **Chemistry: A European Journal** 20 (33), 10451-10455 (2014);

- 6) '*Structurally Stabilized Mesoporous TiO₂ Nanofibres for Efficient Dye-Sensitized Solar Cells*', Fargol Bijarbooneh, Yue Zhao, Ziqi Sun, Yoon-Uk Heo, **Victor Malgras**, Jung Ho Kim, Shi Xue Dou, **APL Materials** 1 (3), 032106 (2013);
- 7) '*Aqueous Colloidal Stability Evaluated by Zeta Potential Measurement and Resultant TiO₂ for Superior Photovoltaic Performance*', Fargol Bijarbooneh, Yue Zhao, Jung Ho Kim, Ziqi Sun, **Victor Malgras**, Seyed Hamed Aboutalebi, Yoon-Uk Heo, Masashi Ikegami, Shi Xue Dou, **Journal of the American Ceramic Society** 96 (8), 2636 (2013);
- 8) '*Rational Design of 3D Dendritic TiO₂ Nanostructures with Favorable Architectures*', Ziqi Sun, Jung Ho Kim, Yue Zhao, Fargol Bijarbooneh, **Victor Malgras**, Youngmin Lee, Yong-Mook Kang, Shi Xue Dou, **Journal of the American Chemical Society** 133 (48), 19314 (2011);
- 9) '*Improved photovoltaic performance of dye-sensitized solar cells with modified self-assembling highly ordered mesoporous TiO₂ photoanodes*', Ziqi Sun, Jung Ho Kim, Yue Zhao, Fargol Bijarbooneh, **Victor Malgras**, Shi Xue Dou, **Journal of Materials Chemistry** 22 (23), 11711 (2012);
- 10) '*Continually adjustable oriented 1D TiO₂ nanostructure arrays with controlled growth of morphology and their application in dye-sensitized solar cells*', Ziqi Sun, Jung Ho Kim, Ting Liao, Yue Zhao, Fargol Bijarbooneh, **Victor Malgras**, Shi Xue Dou, **CrystEngComm** 14 (17), 5472 (2012);

CONFERENCES ATTENDED DURING PHD

- *Oral Presentation*, 23rd Annual Meetings of MRS-J 2013, Yokohama, Japan;
- *Poster Presentation*, **Australian Nanotechnology Network ECR 2012**, Melbourne Australia;
- *Oral Presentation*, **Uniquist Research Commercialization Workshop 2012**, Gold Coast, Australia.